THE UNIVERSITY OF CHICAGO

COMPUTER VISION AND STATISTICAL METHODS FOR THE STUDY OF RENAL AUTOIMMUNITY: THE IMMUNE ARCHITECTURE OF LUPUS NEPHRITIS AND RENAL ALLOGRAFT REJECTION

A DISSERTATION SUBMITTED TO
THE FACULTY OF THE DIVISION OF THE BIOLOGICAL SCIENCES
AND THE PRITZKER SCHOOL OF MEDICINE
IN CANDIDACY FOR THE DEGREE OF
DOCTOR OF PHILOSOPHY

INTERDISCIPLINARY SCIENTIST TRAINING PROGRAM:
GENETICS, GENOMICS, AND SYSTEMS BIOLOGY

BY
GABRIEL BONAMICHI CASELLA

CHICAGO, ILLINOIS
JUNE 2024

Eu dedico essa tese à minha familia, meus amigos, meus Ancestrais, e sobretudo ao meu amado Povo.

Dedico questa tesi alla mia famiglia, ai miei amici, ai miei Antenati, e soprattutto al mio amato Popolo.

I dedicate this thesis to my family, my friends, my Ancestors, and above all to my beloved People.

-Non Ducor Duco-

Canção do exílio

Minha terra tem palmeiras
Onde canta o Sabiá,
As aves, que aqui gorjeiam,
Não gorjeiam como lá.

Nosso céu tem mais estrelas,
Nossas várzeas têm mais flores,
Nossos bosques têm mais vida,
Nossa vida mais amores.

Em cismar, sozinho, à noite,
Mais prazer encontro eu lá;
Minha terra tem palmeiras,
Onde canta o Sabiá.

Minha terra tem primores,
Que tais não encontro eu cá;
Em cismar – sozinho, à noite –
Mais prazer encontro eu lá;
Minha terra tem palmeiras,
Onde canta o Sabiá.

Não permita Deus que eu morra,
Sem que eu volte para lá;
Sem que desfrute os primores
Que não encontro por cá;
Sem qu'inda aviste as palmeiras,
Onde canta o Sabiá.

—Gonçalves Dias (1823-1864)

TABLE OF CONTENTS

LIST OF FIGURES

ACKNOWLEDGMENTS

I wish to express my upmost gratitude to my family, who were central to my path to becoming a physician-scientist. My parents, Jose Casella and Gizelda Casella, my sister Isabella Casella, my grandmother Vó Têtê, all my cousins, and aunts and uncles. I would like to thank my co-PIs Dr. Marcus Clark and Dr. Maryellen Giger for their guidance and mentorship throughout these years. I am grateful for the help and supervision of my thesis committee in revising this manuscript and project. My chair Dr. John Novembre, and fellow committee members Dr. Matthew Stephens and Dr. Jun Huang. I would further like to thank Dr. Madeleine Torcasso (Durkee) who has also been a major source of support and mentorship in my graduate studies. Additionally, I wish to acknowledge the scientific contributions of our clinical collaborators Dr. Anita Chong, Dr. Kichul Ko, and Dr. Anthony Chang. I further would like to specifically acknowledge the contributions of Junting Ai (Lily), who has been critical for the tissue processing and imaging of our biopsies. I want to recognize my lab mates Thao Cao, Michael Andrade and Deep Ghosh who helped in the development of the computational pipeline. Finally, I wish to extend my thanks to the members of the Clark Lab and the Giger Lab for their collegiality and intellectual stimulus. I feel as if I have truly grown as both a person and as a scientist these years in the MSTP program.

ABSTRACT

While single-cell "omics" have been critical for the study of human disease, most of these approaches require tissue dissociation, losing important spatial information. Conversely, traditional immunohistochemical methods are only able to capture the spatial expression of only a limited set of markers. Thus, multiplexed microscopy has reshaped the study of tissue biology by measuring cell expression from +40 proteins while maintaining the spatial context. This study aims to understand the cellular and immune landscapes that underpin highly heterogeneous renal autoimmunity. As such, we collected and analyzed using our advanced computational pipeline for image analysis: 25 Lupus Nephritis (LN), 23 Renal Allograft Rejection (RAR), and six "normal" kidney (NK) control samples. Biopsies were iteratively stained using the PhenoCycler protocol, and imaged with a spinning disk confocal microscope to acquire high-resolution, full-section images with a 42-marker panel covering a wide array of immune and non-immune markers.

In this work, we applied novel algorithms for cell detection, segmentation, classification, and spatial feature extraction, to examine the interaction of immune cells within the renal microenvironment. Nuclear detection and segmentation was performed using Cellpose2.0, and the cell body was approximated by dilating the nuclear masks. We have further developed a decision-tree classifier for the multiclass annotation of renal cells that is analogous to well-established flow-cytometry-based cell analyses and immunophenotyping. In our decision tree, cells are sequentially sorted into marker-negative and marker-positive populations using their mean fluorescence intensity (MFI). Marker order is based upon well-established, hierarchical expression of immunological cell markers. Moreover, we have further created a computational tool to capture Microtubule Organizing Center (mTOC) polarization between pairs of cells, which we leverage to better direct cell-cell contacts and cognate immunity.

Ultimately, we identify key immune populations involved in renal autoimmunity, in particular, CD14+MerTk+ M1 MΦ, CD14+CD163+ M2 (MΦ), and CD8+ T-cells. We detect

a cohort-specific polarization of immune lineages, with LN showing a predominant myeloid-driven pathology, while RAR was characterized by a T-cell autoimmune response. The presence of these immune players in tissue was significantly associated with various features of tissue inflammation, elucidating their potential as biomarkers for disease activity and progression. We find that CD14+MerTk+ macrophages, in concert with CD8+ T-cells, appear to drive an inflammatory response in RAR. In contrast, inflammation in our LN samples is overwhelmingly driven by CD14+MerTk+ macrophages mostly independent from T-cells. This would suggest a more nuanced cellular interplay, where T-cell modulation of macrophage activity influences the inflammatory microenvironment.

In summary, our comprehensive spatial analysis offers new insights into the cellular players underpinning renal autoimmunity; highlighting the potential of immune spatial features to be leveraged as a predictive and diagnostic tool. This dissertation paves the way for future research into targeted therapies that address the unique immunological profiles of autoimmune patients; with a greater emphasis on targeting the myeloid cell compartment in LN and the myeloid:T-cell interactions in RAR. The development of computational tools for spatial analysis presents a technical advancement that allows for a novel approach to understanding the complex and heterogeneous immune responses in renal autoimmunity.

CHAPTER 1

LUPUS NEPHRITIS

1.0.1 Systemic lupus erythematosus and lupus nephritis

Systemic lupus erythematosus (SLE) is a highly heterogeneous autoimmune disease that impacts around 200,000 people in the U.S. alone [1, 2, 3]. Around 40% of these patients have renal disease, denoted lupus nephritis (LN) [4], which is the organ-specific manifestation of SLE. Ultimately, many LN patients do not achieve complete clinical remission and eventually progress to end-stage renal disease (ESRD). Unfortunately, the prognoses for therapy-resistant LN patients have not improved significantly in recent years despite ongoing advances in patient therapy [4]. Preventing ESRD in LN is imperative due to 1) the high economic burden of treatment, 2) the significant loss of quality of life, and 3) the high mortality rate for these patients [5, 6]. Furthermore, it is essential to note that extreme demographic disparities exist in LN patients. SLE and LN disproportionately impact women, comprising 90% of the patient population [7], as well as communities of color (38.5% of patients with SLE are African American (AA) while 36.2% identify as white [8]). In addition to increased prevalence in minority communities, SLE is reported to be phenotypically more severe in communities of color, especially in regards to African Americans [9]. As a result, LN disease overburdens communities that historically have suffered from decades of under-investment and unequal or suboptimal access to healthcare.

It is generally thought that SLE arises due to the loss of immunologic self-tolerance to endogenous nuclear antigens, leading to a systemic autoimmune disorder. These endogenous nuclear antigens elicit an innate and adaptive immune reaction and lead to the proliferation of characteristic chromatin-reactive B cells and a type I interferon response [10]. The innate immune system and T-cells from the adaptive immune system have long been reported to play a role in SLE disease progression. T-cells have been reported to help amplify B cell

autoantibody production and produce cytokines and chemokines that contribute to systemic inflammation [11]. Although the exact etiology of SLE remains unclear, genetic factors play a significant role, contributing to as much as 43.9% of the heritable component of heritable risk and a relative risk of 5.9% in first-degree relatives [12]. Furthermore, genome-wide association studies have identified ∼80 genes that are significantly associated with SLE; many of these single-nucleotide polymorphisms occur in genes involved in type I interferon response, nucleic acid sensing, B cell and T-cell signaling/function; and general inflammation. Other non-genetic factors associated with this loss of self-tolerance include infections, ultraviolet light, hormonal drugs, agricultural pesticides, noxious industrial agents, and a history of smoking [10].

In their groundbreaking 1957 study, Holborow et al. identified the presence of circulating anti-nuclear antibodies in the serum of SLE patients, for the first time linking B cells to the pathogenesis of SLE [13]. B cells generate the BCR receptors through random recombination of germline-encoded gene segments to create a diverse BCR repertoire, essential for recognizing a wide range of pathogens [14]. However, this process inherently risks producing self-reactive B cells, potentially leading to autoimmunity. Despite multiple tolerance mechanisms such as clonal deletion, receptor editing, and the induction of anergy, many naive B cells in healthy individuals still show varying degrees of autoreactivity. From an evolutionary perspective, however, a broad humoral response to diverse pathogens necessitates the maintenance of this breadth of repertoire. Completely removing all self-reactive B cells could create vulnerabilities in the naive repertoire that pathogens might exploit. It is thought that in SLE, self-reactive cells persist within the naive repertoire. SLE, whose exact origins remain unclear, can potentially impact any organ in the body [15]. The presentation of SLE in patients is notably diverse, with symptoms ranging from mild skin and joint issues to severe complications involving the kidneys, blood, or central nervous system. This clinical variability and the absence of definitive diagnostic markers or tests present substantial

diagnostic challenges for healthcare providers. Furthermore, the presentation of SLE can be limited to a few non-specific clinical signs that may mimic other autoimmune, infectious, or hematological conditions.

Lupus research and therapy have traditionally focused on B cells given that 1) autoreactive antibodies characterize LN, 2) B cells are capable of antigen presentation as professional antigen-presenting cells (APCs), 3) B cells are numerous in LN biopsies, 4) B cell activating factor (BAFF) is increased in LN kidneys, and 5) LN kidneys have de novo tertiary lymphoid like structures [16, 17, 18, 19]. However, focusing solely on B cell therapies is insufficient as a treatment for many LN cases. The landmark single-cell AMP study [16] has further highlighted the significant heterogeneity of LN and previously unappreciated T-cell and myeloid immune compartments in these patients. More research is clearly needed to understand how overlooked immune cell types, such as cytotoxic T-cells and myeloid cells, contribute to LN disease activity.

1.0.2 Lupus nephritis: glomerulonephritis

Two types of immune inflammation are commonly identified on LN kidney biopsies: glomerulonephritis (GN) and tubulointerstitial inflammation (TII). Glomerulonephritis has long been described in LN and is considered by many to be a traditional hallmark of LN disease. GN in LN is thought to be primarily caused by immune complex deposition within the glomeruli, as these patients often present with "full house" immunofluorescence staining for immunoglobulins IgA, IgM, IgG, and complement factors C3 and C1q [20]. The latter complement proteins are among SLE's most researched molecular mediators [10]. Furthermore, recent studies have shown an association between anti-dsDNA antibodies and GN pathogenesis [21]. Constitutively active B-cells and B cell activating factor (BAFF) have long been known to drive autoantibody production in SLE patients. Lowering autoantibody levels can be achieved therapeutically through BAFF blockade (for instance, using belimumab) or by B-cell deple-

tion (anti-CD20 rituximab), commonly employed to treat SLE patients [10]. Interestingly, a long-lived bone marrow resident population of plasma cells has been associated with LN patients, further highlighting the role of autoantibodies in GN [10, 22].

A specific neutrophil subset, known as low-density granulocytes, has been implicated in exacerbating glomerular inflammation. This is done through the neutrophil's release of DNA-protein nets, believed to induce widespread inflammation and lead to the loss of T-cells and B-cells' self-tolerance [23]. Accordingly, peripheral blood levels of neutrophils correlate with LN disease activity in SLE patients [24]. Given the correlation between lupus disease activity, anti-dsDNA antibodies, and circulating T follicular cells, the absence of T follicular helper (TfH) cells in glomerular histology suggests a systemic, rather than localized, role in the development of glomerulonephritis (GN) through the breakdown of immune tolerance [25, 21].

1.0.3 Lupus nephritis: tubulointerstitial inflammation

Tubulointerstitial inflammation (TII) is an extremely heterogeneous immune phenotype characterized by significant T-cell and B-cell aggregates and the formation of large immune-rich structures akin to tertiary lymphoid structures (TLS), which typically develop in areas of chronic inflammation. Single-cell RNAseq has been pivotal in capturing how the TII environment is incredibly complex. Dendritic cells, B-cells, T-cells, natural killer cells, T follicular helper cells and plasma cells are some of the immune cells that are known to contribute to the observed heterogeneous autoimmune response [16, 17, 25, 26, 27]. CD4+ T-cells are one of the most abundant lymphocytes in the kidney, however IgD-CD27- B-cells were also common [16]. pDCs have been identified as an important in situ antigen-presenting cell (APC) within the TII [26]. Additionally, CD3+CD8+ T-cells are known to accumulate in periglomerular [28] and peritubular [29, 30] regions and have been associated with poor renal health [28, 29, 30, 31].

Laser capture microscopy has confirmed that these TLS-like sites actively engage in immune cell clonal expansion and somatic hypermutation, key characteristics of tertiary lymphoid structures [27, 21]. Additionally, T-follicular cells have been implicated in providing costimulatory signal to B-cells in the TII, and many of the reported T-cell:B-cell aggregate are in fact Tfh:B-cell interactions [25]. When the antibodies from clonally expanded intrarenal B cells were analyzed, it was found that most antibodies bound cytoplasmic antigens, most notably vimentin. While vimentin has been traditionally thought as merely an intermediate structural filament, recent data has highlighted a potential pro-inflammatory role. Vimentin secretion by activated macrophages, purported interaction with Dectin-1, and expression in inflamed LN biopsies within the tubulointerstitium all implicate vimentin in promoting in situ inflammation [21]. Interestingly, serum anti-vimentin antibodies correlated with TII disease severity [32]. While tubulointerstitial inflammation is more predictive than GN for progression to ESRD, around half of LN patients with moderate to severe TII will not develop ESRD, showing the need to understand patient heterogeneity. Several groups have demonstrated that immune cell spatial context in situ is indispensable for understanding disease progression and trends in patient survivability [33, 34].

1.0.4 Clinical features and common treatments

The majority of SLE patients develop LN within the first 5 years of their diagnosis; this time is even shorter in minority patient populations such as African-American patients and Hispanic-American patients [35, 21, 10]. SLE has a total prevalence of 8-180 cases per 100,000 individuals, with a notably higher prevalence in females (f/m ratio of 6.1 to 13.3:1) [36]. One of the hypotheses behind why females are more prone to SLE is that it is due to the cumulative dosage effects of genes such as *TLR7* [10]. Paradoxically, the prevalence of LN is higher in males than in females, with ratios ranging from 1.1:1 to 1.7:1.

LN is still a major cause of morbidity and mortality in SLE. While the five-year mortal-

ity rate decreased steadily from 1975 to 1995, it has persisted at a constant despite novel interventions [37]. During initial diagnosis, patients are most regularly observed having mild proteinuria, and/or hematuria, and more rarely leukocyturia. Even more infrequent are 'silent' LN cases that insidiously present normal laboratory results. On the other extreme, are patients who initially present with severe proteinuria (greater than 3.5 g per day), advanced CKD, or acute nephritic syndrome as the initial clinical manifestation of LN [10, 38]. Due to the high variance of laboratory blood and urinalysis results, kidney biopsies remain the gold standard for confirming LN diagnosis and the corresponding histopathological subtype; this is particularly important for detecting those 'silent' LN cases [10, 39]. Kidney biopsies are usually advised in cases of persistent proteinuria of greater than 0.5 g daily when accompanied by hematuria and/or cellular casts, but also in cases of persistent hematuria after dismissing other more probable causes [38]. The histological presentation on biopsy is also vital for excluding clinical mimics such as thin basement membrane disease, hypertensive nephrosclerosis, IgA nephropathy, and diabetic nephropathy [10, 40]. Kidney biopsies will often have signs of arteriosclerosis, tubular atrophy, glomerular sclerosis,vascular lesions, and interstitial fibrosis and inflammation. Interestingly, many patients who respond well to induction therapy will still have signs of active kidney disease upon repeat biopsies, up to 29% of patients with a complete response [41].

The immunosuppressive therapy regimen is separated into an initial induction therapy with strong immunosuppressants (3-6 months) to attain swift remission, and a maintenance therapy with a milder low-dosage of immunosuppressants and steroids to prevent disease activity flares. Induction therapy usually involves glucocorticoids paired with either cyclophosphamide or mycophenolate mofetil (MMF). Interestingly, African-American (40% vs 53.9%; P = 0.39) and Hispanic patients (38.8% vs 60.9%; P = 0.011) showed greater improvement with MMF rather than cyclophosphamide, Asian (53.2% vs 63.9%; P = 0.24) and white patients (56.0% vs 54.2%; P = 0.83) on the other hand, had similar improvements with

either drug [42]. In one specific study, 68% of patients who had a renal flare while taking cyclophosphamide developed chronic kidney disease over the median follow-up of 6 years [43]. B-cell depletion through biologics like rituximab (anti-CD20) is not effective compared to MMF alone. Another biologic, Belimumab (anti B-cell activating factor BAFF) is still undergoing clinical trials but has successfully met some initial key trial endpoints [10]. Anti-malarial (AMAs) drugs such as hydroxychloroquine are recommended to almost all patients with LN. AMAs reduce the chance of developing LN in SLE patients, and in LN patients it increases the chances of remission, decreases the frequency of flares, and reduces the risk of progression to ESRD [10, 44]. However, patient response to these therapies is extremely varied with relapse flare rates as high as 35%, and anywhere from 5% to 20% of LN cases will go on to ESRD within 10 years of the initial flare, requiring either ongoing dialysis or organ transplantation [10].

1.0.5 Spatial immunity

Spatial immunology is an emerging field integrating spatial analytics with immune system research to explore immune cells' spatial distribution and interaction within different tissues and organs [45, 46, 47, 48]. Spatial "omics" methods have revolutionized our understanding of the complex landscape of our immune system's response to pathogens, tumors, and autoimmune disorders. Spatial immunology utilizes advanced imaging techniques such as multiplex immunohistochemistry (mIHC), mass cytometry (CyTOF), and single-cell RNA sequencing (scRNA-seq) combined with spatial transcriptomics. These methods enable researchers to map immune cells' localization and functional state within tissues. One major application of spatial immunology is in cancer research, where understanding the tumor microenvironment (TIME) is crucial for developing effective immunotherapies [47, 45]. Studies have shown how the spatial arrangement of immune cells within tumors can predict treatment response and patient prognosis.

Current imaging and analytical techniques can be limited in their resolution and the number of markers they can simultaneously detect. This can restrict the accuracy and depth of immune cell profiling within tissues [46, 48]. The vast amount of data generated by spatial immune studies is challenging to process and interpret. Advanced computational tools and algorithms are required to analyze and visualize this data effectively. Furthermore, there is a lack of standardized protocols for tissue preparation, image acquisition, and data analysis in spatial immunology. This variability can lead to inconsistencies across studies and hinder the comparability of results. Advancements in imaging technologies and computational analysis are likely to drive the evolution of spatial immunology. Developing standardized methods and addressing ethical concerns are crucial for the progression of this field. Furthermore, integrating spatial immunological data with other "omics" data could lead to a more comprehensive understanding of immune responses in various health and disease contexts. Omics technologies offer vast potential in immunology, producing high-dimensional data that typically necessitates unbiased, exploratory data analysis. Yet, to truly harness these technologies effectively, it is crucial to adhere to the principles of hypothesis-driven science. While some may view a hypothesis as a limitation that could narrow the scope of inquiry, it serves as a crucial guide that focuses research efforts while still allowing for the emergence of new hypotheses and discoveries through data analysis. This disciplined approach helps maintain clarity and direction in research, ensuring meaningful and impactful outcomes [46, 48].

1.1 Pior work of the lab

1.1.1 High-resolution (HR) dataset

To better understand how TII is associated with clinical outcomes, in our paper [49], the Clark-Giger lab collected 55 LN FFPE archival biopsies with known outcomes after at least

2 years of longitudinal follow-up. 14 patients progressed to renal failure (ESRD+) within 2 years of diagnosis, 5 patients underwent recent renal failure (ESRD current), and 35 patients did not progress to renal failure (ESRD-) within 2 years of diagnosis. We hypothesized that differences in renal outcomes would correlate with differences in in situ adaptive immunity, specifically in the frequency and arrangement of immune effector cells in tissue. At the time, our group had already identified some shared immune features amongst inflamed LN biopsies such as T:B aggregates and TLS [27, 25]. To this end, each biopsy was stained for six markers for prominent immune cell populations: CD3, CD4, CD20, CD11c, BDCA2, and DAPI. This allowed for the characterization of five immune cell categories: CD3+CD4+ T cells, CD3+CD4– T cells, CD20+ B cells, BDCA2+ pDCs, and CD11c+ mDCs. Among the 55 biopsies, all regions of interest (ROIs) with observable CD3+ T cells were captured, leading to a total of 865 ROIs denoted as the high-resolution (HR) dataset. Each image ROI measured 1024 $\times$ 1024 pixels, with an individual pixel dimension of 0.1058 μm (Figure 1.1A).

When evaluating the overall cell density (total cells per ROI) in the HR dataset, no marked differences emerged between ESRD– and ESRD+ (including ESRD current) patients. However, due to the known associations between immune cell aggregates and TLS with disease activity and inflammation in LN, we sought to further capture and phenotype immune cells aggregates. As a result, I used the Density-Based Spatial Clustering of Applications with Noise (DBSCAN) algorithm [50] at a centroid-centroid distance of 100px to spatially segment aggregates of immune cells within the 1024x1024 images, putative for inflammatory cell networks. (Figure 1.1B) 100 pixels was initially chosen due to it being an approximation for the average cell body size. However, further analyses using 50 pixels, 75 pixels, 125 pixels, and 150 pixels revealed that distances under 100 pixels was too stringent and tended to sub-compartmentalize large immune aggregates. On the other hand, distances greater than 100 pixels captured most of the cells in an ROI, losing DBSCAN's utility since it mirrors global

ROI-based analyses.

After performing DBSCAN, I employed unsupervised clustering using K-means clustering to determine the subphenotypes of these immune aggregates. Metrics such as cell frequencies, cell proportion, and cell morphology were used for feature extraction due to the intuitiveness and interpretability of using these features to quantify aggregates. Following feature extraction, I employed a bootstrap subsampling experiment at N = 250 repetitions, and K = 6 clusters was determined to be the optimal number of clusters using the empirical elbow method on the within-cluster sum of distances squared (WCSS) and delta WCSS plots. (Figure 1.1C) I used a leave-one-out T-test [49, 51] to find the unique defining features between these 6 cell aggregates. I assigned the following cluster classes: CD4+ T-cell dominant, CD4- T-cell dominant, pDC dominant, B-cell dominant, mDC dominant, and large immune mixed. (figure 1.1D-E) The latter large immune mixed cell aggregate was hypothesized to be putative for a TLS; however, at the time we lacked the appropriate cell markers (PD1, ICOS, FOxP3) to verify this.

To understand the cohort differences in these captured immune cell aggregates, I performed a non-parametric Mann-Whitney U test with a Bonferroni correction comparing the total neighborhood count per ROI between ESRD- and ESRD+ cohorts and found that the aggregate cell count for each sample was more pronounced in the ESRD+ group (with ESRD current), indicating more extensive inflammation zones in ESRD. When comparing the aggregate subtypes, I found that CD4-T-cell dominant aggregates had a statistically significant association with ESRD status (p=0.04). If the ESRD cohort is further broken down into ESRD+ and ESRD current, we find statistically significant associations between CD4- T-cell dominant aggregates and ESRD+ (p=0.03) and ESRD current (p=0.009). The specific increase in ESRD current patients led us to believe that CD4- T-cells were involved in areas of active inflammation (Figure 1.1 F). These CD4-CD3+ T-cells in theory, can correspond to CD8+ T-cells, $\gamma\delta$ T-cells, and natural killer T-cells since these immune cell populations

are all CD3+ and CD4- T-cells by definition.

1.1.2 Highly-multiplexed (HMP) dataset

We employed highly multiplexed (HMP) confocal microscopy on a distinct dataset of 18 LN biopsies as a follow-up dataset to our HR analyses. To enhance the diversity of the immune lymphocyte population captured in situ in this HMP dataset, an ensemble of 9 markers was probed, namely CD3, CD4, CD8, ICOS, PD1, FoxP3, CD20, CD138, and DAPI. Notably, this dataset did not cover myeloid cell lineage markers due to the focus on T-cells/B-cells (adaptive immunity). Furthermore, instead of capturing singular ROIs of inflamed regions as in the HR dataset, entire biopsy sections were imaged, allowing for comprehensive spatial analysis as global tissue coordinates are preserved.

Within the HMP dataset, T cells were the predominant lymphocytes at 65% cells and Plasma cells emerged as the second most populous class, accounting for an estimated 28% of lymphocytes. B cells, in contrast, demonstrated a markedly smaller prevalence, constituting a mere 6%. Again, CD4+ T cells underscored their dominance in our data by emerging as the most abundant cell population, constituting 35% of the recognized lymphocytes and above 50% of T cells, CD8+ T-cells represented around 17% of the identified lymphocytes and a proximate 26% of all T-cells. A significant population of T cells CD4-CD8- were also found in the biopsies. Approximately one-third (30%) of the CD8+ T cells within the HMP dataset exhibited PD1+ expression, implying a potential exhausted phenotype. Around a quarter (25%) of the CD8+ T cells were categorized as demonstrating an "exhausted" state (PD1+ICOS–FoxP3–). Approximately 5.41%, of the CD4+ T cells expressed FoxP3, and an even smaller subset was also PD1–ICOS–, implying that T regulatory cells (Tregs) constitute roughly 2.5% of CD4+ T cells. T follicular helper (Tfh) cells were identified through the co-expression of PD1 and ICOS by CD4+ T cells. Within the CD4+ T cell category, 5.05% displayed the PD1+ICOS+FoxP3– profile. Using the criterion of PD1+ICOS+/–/FoxP3–

Figure 1.1: Early work: lupus nephritis and DBSCAN neighborhood analysis

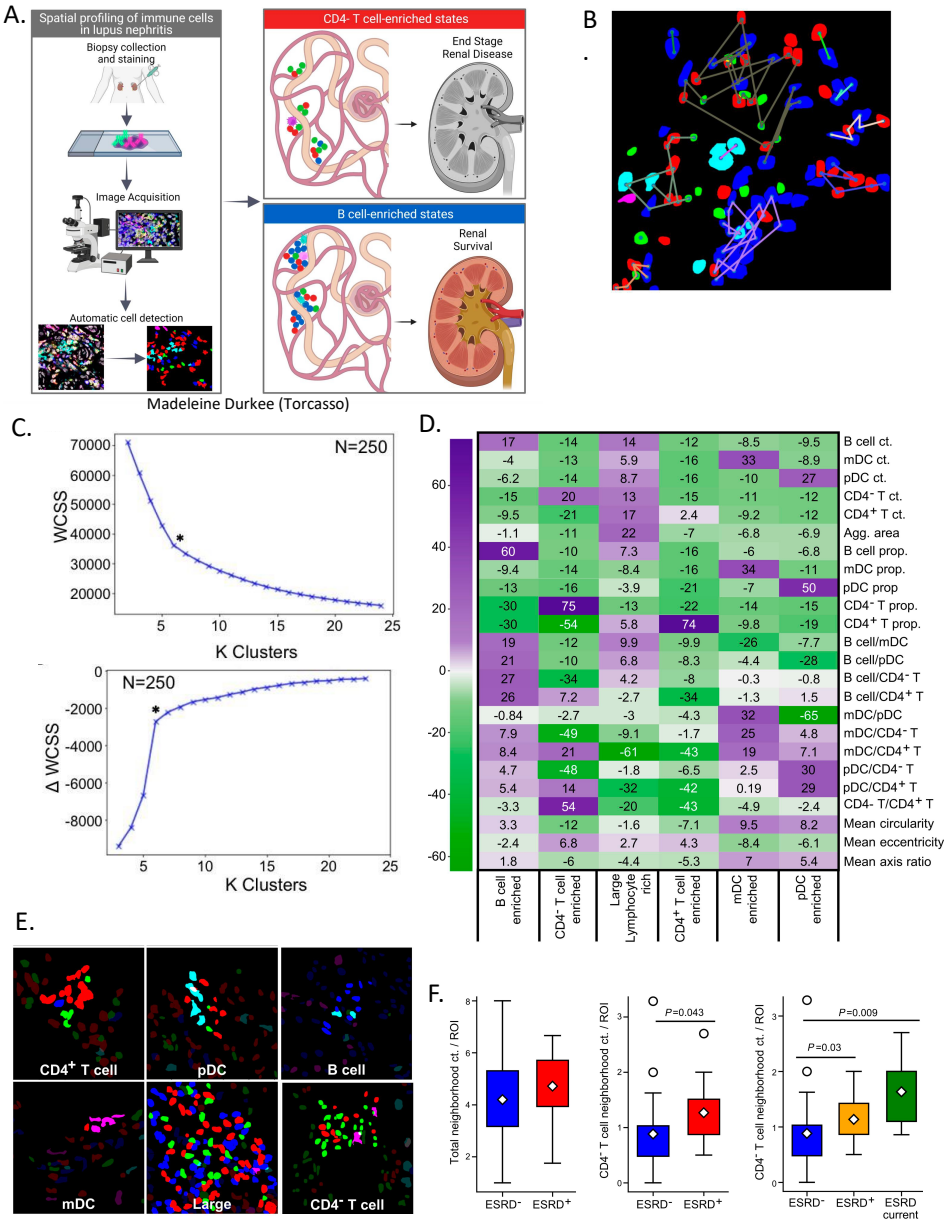

A) Graphical abstract of the Abraham et al paper [49]. B) Neighborhoods of automatically detected cells were spatially segmented by DBSCAN. Automatic cell segmentations and representative neighborhoods (highlighted in E) are shown for images taken at 63x magnification. C) within cluster sum of distances squared (top) and delta WCSS (bottom). D) Heatmap showing test statistics for each feature from leave-one-out t tests used to define 6 types of cell neighborhoods, colored by the magnitude of the test statistic. E) Representative neighborhoods from each defined class. F) The abundance of neighborhoods between the patient cohorts, normalized by the number of ROIs per patient, was compared by Mann-Whitney U test with a Bonferroni's correction for (left) all cell neighborhoods and (middle, right) CD4– T cell neighborhoods. Significant P values after correcting for multiple comparisons are noted.

to definite the Tfh cellular subset, approximately 30% of the CD4+ T cells were recognized as Tfh cells. To further explore the characteristics of these T-cells in lupus nephritis (LN), we utilized public single-cell RNA sequencing (scRNA-Seq) data from immune cells in the kidneys of LN patients [16]. Using unsupervised clustering and canonical marker expression, our analysis identified naïve T and CTL clusters among these intrarenal immune cells. We noted a subpopulation expressing TRAC and TRDC, indicating these DN T cells might be $\gamma\delta$ T cells. Further validation was done through staining eight LN biopsy samples with antibodies for CD3, CD4, CD8, and TCRγ, revealing that on average, 51.4% $\pm$ 21.3% of DN T cells were TCRγ positive. Spatial analysis of the tissue showed that CD4– T cell populations, including CD8+, $\gamma\delta$, and double-negative (DN) T cells, often formed distinct clusters. These clusters were found to be linked to severe/treatment-resistant disease, and predicted progression to renal failure. Conversely, areas with significant B cell aggregates were found in patients with better prognoses, suggesting diverse autoimmune processes in LN that might require tailored therapeutic strategies. These findings highlight the potential heterogeneity in pathogenic mechanisms and the importance of targeted treatments in LN.

To further characterize DN T cells, we interrogated public scRNA-Seq data of immune cells infiltrating the kidneys of patients with LN [16]. We identified naive T and cytotoxic clusters in intrarenal immune cells by unsupervised clustering and canonical marker expression. Yuta Asano pioneered this work. When looking at the expression levels of TCRα and δ chains, we observed a subpopulation of cells that were positive for both TRAC and TRDC; suggesting that DN T cells in LN could indeed be $\gamma\delta$ T cells. We subjected eight LN biopsy samples to staining using antibodies specific to CD3, CD4, CD8, and TCRγ. On average, 51.4% $\pm$ 21.3% of DN T cells were TCRγ positive. When looking at how cells and inflammation is organized in tissue, the data demonstrated that CD4– T cell populations, encompassing CD8+, $\gamma\delta$, and double-negative (CD4–CD8–δ–; DN) T cells, frequently assemble into discrete cellular clusters. Such clusters are both associated with acute refractory disease

and serve as predictors for progression to renal failure. Conversely, areas with large B cell aggregates correlated with patients who did not advance to renal failure. These observations and additional findings suggest that systemic and in situ autoimmune pathogenic processes in LN phenotypically differ, and each may necessitate distinct therapeutic approaches.

The association between favorable renal outcomes and dense B cell aggregates was unexpected as LN is traditionally considered a B-cell disease. We developed multiple possible biological explanations for this experimental result. For example, B cells may play an overlooked protective function amidst renal inflammation [52]. Another possibility is that the presence of B cells and the consequent local antibody production might be either innocuous or neutral compared to other in situ pathological events. A third possibility is that while dense B-cell areas may instigate tissue damage, traditional B-cell-focused therapeutic interventions effectively counteract this phenomenon. A significant proportion of these patients underwent treatments involving high-dose steroids and cytotoxic treatments, predominantly mycophenolate. Such treatments are documented to diminish both B cells and plasma cells [53]. This prior study was an essential step to developing our current CODEX project with LN and RAR biopsy samples. Most notably absent from the HR and HMP datasets are the myeloid cell lineages, such as monocytes and macrophages due to the lack of inclusion of relevant myeloid markers such as CD14, CD16,HLAII, and CD68. As such, we decided to focus more on capturing myeloid cell lineages in our CODEX project to fill this knowledge gap.

CHAPTER 2

ALLOGRAFT REJECTION

The earliest recorded attempts at transplant surgery date back to around 1000 B.C., with the Indian surgeon Sushruta Samhita documenting detailed protocols for autologous tissue flap transplantation in nasal tissue reconstruction. More than two millennia passed before these surgical techniques were revived and rediscovered in 16th-century Renaissance Italy, notably by Gasparo Tagliacozzi [54, 55]. Since the innate vascular supply was preserved and autologous tissue was used, these early autograft procedures avoided the challenges associated with organ rejection and vascular anastomosis of allografts from another organism [55]. French surgeon Alexis Carrel, who won the Nobel Prize in Physiology or Medicine in 1912, was a significant pioneer of organ transplantation. In his seminal work published in 1902, Dr. Carrel exploited recent advances in suture technology to perform vascular anastomoses using animal models; these anastomotic techniques eventually served as the foundation for contemporary vascular anastomotic procedures [56].

Dr. Carrel eventually relocated to Chicago to collaborate in an experiment involving autotransplantation of a canine kidney to a different anatomical site within the same organism and performed subsequent experiments involving kidney allografts between genetically disparate animals of the same species. They noted that while the autograft remained functional, enabling the animal to live for an extended duration and produce offspring, the allografts conversely were less functional and had higher post-surgical complications [55, 56]. In these experiments, Dr. Carrel first proposed the concept of "biologic incompatibility" as the cause of allograft failure. This was one of the earliest proposals that immunological incompatibility was a barrier to successful transplantation. After decades of further research, organ rejection is now well recognized as an immunological response wherein the recipient's immune system reacts to donor-specific antigens.

2.1 Disease and pathophysiology

Renal allotransplantation, has now emerged as the most effective therapeutic intervention for patients with end-stage renal disease (ESRD); some of whom are Lupus Nephritis patients described in Chapter 1. This particular surgical intervention offers significant improvements in both life expectancy and in quality of life indices when juxtaposed against alternative renal replacement therapies such as traditional hemodialysis or peritoneal dialysis. It is imperative to underscore the persisting disparity in long-term survival metrics in allotransplantation patients; life expectancy for renal allotransplantation recipients remains approximately four times lower than their counterparts without ESRD [57, 58, 59, 60]. Despite advancements in post-operative management, there has been little improvement in long-term graft and patient survival rates; approximately 40% of kidney transplants fail within a decade post-transplantation [61]. Chronic kidney transplant rejection (CKTR) is primarily categorized into two major subtypes: Chronic active T cell-mediated rejection (TCMR) and chronic active antibody-mediated rejection (ABMR) [62].

Renal allograft biopsy is the primary diagnostic exam for identifying graft rejection; allowing for the determination of both the subphenotype and severity of the rejection episode. While biopsy specimens can be evaluated using light microscopy, immunofluorescence, and electron microscopy techniques, light microscopy is traditionally used most for assessing the allograft rejection phenotype [60, 61]. As such, our CODEX multiplex imaging dataset provides unprecedented detail of graft rejection. Aside from imaging, the clinical monitoring of allograft function in kidney transplant recipients involves a panel of indicators, such as serum creatinine levels, estimated glomerular filtration rate (eGFR), proteinuria levels, and donor-specific antibodies (DSAs) levels. Despite their widespread use in the clinic, these markers have great limitations such as low sensitivity and specificity, invasiveness of certain tests, and difficulty in exam interpretation by clinicians [63].

Initially introduced in 1993, the Banff classification serves as a standardized system for

pathological assessment of renal grafts [62]. The latest iteration of the Banff classification system includes six distinct clinical categories. The main categories are: Category 2, which focuses on antibody-mediated changes; Category 3, designated as 'borderline' for acute T-Cell Mediated Rejection (TCMR); and Category 4, which is explicitly related to TCMR. The pathological manifestations of rejection can be found across all four anatomical compartments of the kidney: the glomeruli, tubules, interstitium, and blood vessels. Based on the temporal context post-transplantation and the level of rejection activity, rejection episodes can be categorized as either acute/active or chronic. Although "acute" and "chronic", in the context of the Banff criteria, are indicative more of the activity or quiescence of the rejection process rather than the timing of the biopsy per se [60]. Acute (active) rejection is characterized by a range of histopathological features including tubulitis, interstitial inflammation, glomerulitis, peritubular capillaritis, and arteritis. Chronic rejection, on the other hand, commonly shows distinct features such as tubular atrophy, interstitial fibrosis, transplant glomerulopathy, multilayering of peritubular capillary basement membranes, and transplant arteriopathy [60]. Identifying prognostically useful initial features of tissue injury before the onset of irreversible graft damage continues to pose a substantial challenge. No immunotherapeutic interventions have yet been validated as effective in preventing or treating chronic kidney transplant rejection (CKTR), with the ABMR subtype as particularly challenging [61], necessitating the human biopsy research contained in this dissertation.

2.2 Risk factors

Insufficient immunosurpression or therapeutic nonadherence has long been recognized as the primary reason behind post-transplantation allograft rejection [61, 57, 64]. Sub-optimal adherence to the immunosuppressive therapy regimen has significant consequences for transplant recipients, such as elevated healthcare expenditures and medical complications, heightened rates of allograft rejection, and increased patient mortality [61]. Non-adherent pediatric

transplant recipients are subject to a twofold elevated risk of biopsy-confirmed organ rejection, culminating in an organ loss rate of 80% in these patients. The non-adherence rate among pediatric renal transplant recipients is estimated to oscillate between 30 to 70%. Furthermore, there is a direct correlation between levels of adherence and adverse outcomes; for each 10% decrease in adherence levels, there is a statistically significant 8% incremental hazard of graft failure and patient mortality [57, 65]. Pre-surgical risk factors known to contribute to allograft rejection are broken into donor- or recipient-related risk factors spoken in detail below.

2.2.1 Risk factors: donor

Donor gender has had mixed associations with organ rejection rates, with reports indicating that patients who received organs from females had worse outcomes, as well as contradictory reports of no statistical difference due to donor gender [57]. However, donor age's prognostic value surpasses donor gender for allograft outcomes. Allografts from advanced-age donors are predisposed to an array of post-transplantation sequelae, such as delayed graft function, acute immunological rejection, and eventual graft failure. Transplantation utilizing allografts from either extreme of the donor age spectrum, from very young or significantly aged donors, is an independent risk for worse post-transplant clinical outcomes. For example, allografts from donors aged 65 years and above demonstrate an elevated incidence of acute immunological rejection episodes. It is reasonable to assume that renal allografts harvested from aged donors have dubious long-term graft viability compared to young donor organs due to organ age. Consequently, to mitigate the risk of premature organ failure, organ donor should be aged matched to the recipients (young-young;old-old) [57, 66, 67, 68]. It is further known that alloimmune reactivity is diminished in renal allografts sourced from living donors versus deceased donors, conferring a demonstrable reduction in short-term morbidity and mortality rates while simultaneously increasing graft longevity. For example, 53% of cadaver-donor

renal grafts demonstrated increased neutrophilic infiltration, in stark contrast to the minimal occurrence observed in grafts procured from living donors. Nonetheless, recipients of kidneys from deceased donors experience a 68% reduction in mortality risk when juxtaposed against those who do not undergo allotransplantation and remain on standard dialysis. Therefore, deceased-donor renal allotransplantation is commonly done to increase the donor pool due to high demand despite increased organ rejection risks [57, 69, 68].

ABO incompatibility profiles have served as core markers of transplant matching since transplantation between individuals with discordant blood-group compatibility results commonly in hyperacute rejection episodes. ABO-incompatible transplantation is associated with an augmented risk of early organ rejection episodes, infectious complications, and subsequent patient mortality. Given the vast donor organ scarcity, medical strategies such as pre-transplant splenectomy, plasmapheresis, and intensified immunosuppressive regimens are employed to surmount discordant blood-group compatibility [57, 70]. Before transplantation, both HLA tissue typing and the quantification of anti-donor HLA antibody serum concentrations are routinely done on potential organ recipients as part of the allocation process for organ donors. HLA typing tests for the principal proteins complexing to form the major histocompatibility complex (MHC), including class Ia (HLA-A, -B, -C), class Ib (HLA-E, -F, -G, -H), and class II (HLA-DR, -DQ, -DM, and -DP) in both the donor and recipient. The sensitization of the recipient to donor-specific Human Leukocyte Antigen (HLA) serves as a critical event for shaping the prognostic landscape of the donor organ. Such sensitization can be quantitatively assessed by measuring donor-specific anti-HLA immunoglobulin antibodies (DSA) in the recipient's serum. Renal six-antigen-matched allografts exhibit superior survival rates, prompting many clinicians to meticulously align the complete array of associated HLAs during risk assessment. The extent of HLA mismatch between donor and recipient is correlated with graft survival [57]. Emerging research suggests that T follicular helper cells (Tfhs) may promote the emergence of donor-specific anti-HLA antibodies (DSA)

that is thought to contribute to graft loss. Consequently, early post-transplant monitoring of activated Tfhs could serve as a predictive biomarker for the subsequent appearance of DSA following renal transplantation [71].

2.2.2 Risk factors: recipient

African American patients are susceptible to worse clinical outcomes, with elevated rates of organ rejection compared to white peers [72]. However, organ recipient age stands as a significant determinant of renal allograft outcomes, with a younger demographic displaying a heightened risk for sub-optimal results; pediatric patients manifest a higher relative risk of acute immunological rejection episodes. This is likely related to the general loss of immune reactivity to antigens with biological age. Interestingly, within the pediatric age spectrum, recipients aged between 6 and 12 years had a reduced risk of organ rejection within the initial 90 days post-transplantation compared to the cohorts aged between 2–5 and 13–20 years. Complications such as thrombosis and primary non-function were predominantly observed in recipients younger than five years, while non-adherence-induced acute rejection episodes were more prevalent among juveniles [72, 73, 74]. Furthermore, the presence of concomitant pathologies, such as infectious diseases, coagulopathies, and neoplastic disorders, can further contribute to graft loss and poor post-transplantation outcomes. However, cardiovascular disease emerges as the principal etiological agent responsible for mortality after renal transplantation, with particular prominence in patients afflicted by autoimmune diseases such as systemic lupus erythematosus [57, 75].

Acute rejection rates are relatively elevated among renal re-transplant recipients, ranging from 33% to as high as 69% according to current data [76]. Re-transplantation recipients are predisposed to delayed graft function, a phenomenon principally attributable to prior sensitization events. Historically, the recurrence of HLA antigen mismatches from initial transplantation was implicated in the fast onset of alloimmune-mediated damage and subsequent

graft loss, attributed to the re-stimulation of the recipient's immune system. However, further research revealed that re-transplant patients with recurrent HLAII antigen mismatches display a heightened chance for developing rejection episodes and eventual graft loss [57].

2.2.3 Risk factors: other factors

Ischemia/reperfusion injury (IRI) stands as one of the predominant complications encountered in the post-operative phase of renal transplantation. It is thought that after the reperfusion event, the generation of free oxygen radicals leads to localized inflammatory responses and concurrently activates the complement and coagulation cascades. IRI is known to amplify graft alloreactivity, as well as increases humoral antibody response, subsequently escalating the risk for acute graft rejection episodes. IRI injury impedes donor organ function, a phenomenon that is histologically manifested through acute tubular necrosis [57, 77, 78]. Other factors that contribute to graft loss include interstitial fibrosis/tubular atrophy (IF/TA), recurrence of the original nephropathic disease, vulnerability to opportunistic infections due to immunosuppression, renal function delay, and metabolic dysregulation associated with diabetes mellitus. All these risk factors necessitate a multifaceted approach to post-transplant management for optimizing graft longevity and patient outcomes taking into account the prexisting comorbidities unique to each case [57, 59, 61].

2.2.4 Allograft rejection: T-cell-mediated

The identification of both acute and chronic T-cell-mediated rejection (TCMR) on histopathological examination is primarily based on morphological alterations within the tubulointerstitial region. The criteria for diagnosing acute TCMR have remained relatively stable since their initial outline in the 1991 Banff classification, and its presence is assessed based on the level of active inflammation observed in non-atrophic tubules, interstitium, and blood vessels [60]. Tubulitis is a hallmark feature of acute and chronic active TCMR, marked by the in-

filtration of inflammatory cells interposed between tubular epithelial cells. In the context of acute TCMR, tubulitis is typically found in non-severely atrophic tubules, while in chronic active TCMR, it may affect both atrophic and non-atrophic tubules. Interstitial inflammation is a characteristic feature of both acute and chronic active TCMR. In chronic active TCMR, infiltrating inflammatory cells are observed in both edematous and fibrotic stromal areas, accompanied by tubulitis affecting both atrophic and non-atrophic tubules. The infiltrate commonly consists of T cell lymphocytes and monocytes, although plasma cells, neutrophils, and eosinophils may also be present. Interstitial hemorrhage can be observed non-specifically in active Antibody-Mediated Rejection (ABMR) or acute T-Cell Mediated Rejection (TCMR).

As the name would suggest, the pathogenesis of TCMR involves persistent injuries mediated by T cells that can culminate in the development of chronic active TCMR. Specifically, alloreactive effector memory CD8+ Tmem cells, which are characterized by increased expression of markers such as CD44hi, CD45RO+, OX40, KLRG-1, and BLIMP-1, have been implicated in the pathogenesis of TCMR [79]. This is immunologically important as Tmem cells exhibit a lower activation threshold, potent effector functions, and notably resist conventional immunosuppressive treatments and costimulation blockade [80]. These memory T cells are thought to either arise from environmental antigenic exposures or be generated from prior rejection episodes. Upon activation, Tmem has been reported to infiltrate the renal interstitium and secrete an array of pro-inflammatory cytokines, including interferon-gamma (IFNγ), triggering an inflammatory cascade culminating in tubulitis [61].

Interstitial fibrosis and tubular atrophy (i-IFTA) stand as other hallmark features of chronic kidney transplant rejection (CKTR), alongside the concomitant presence of tubulitis mentioned previously [61]. Interstitial fibrosis is identified through the abnormally greater presence of collagen fibrils and extracellular matrix components within the renal interstitium. When observed in the setting of chronic active TCMR, this fibrotic interstitium may

also display inflammatory cell infiltration. Tubular atrophy is observed in both chronic rejections and non-rejection conditions and is defined by either a greater than 50% constriction of the tubular diameter or by thickening of the basement membrane. Furthermore, arteritis is a condition commonly observed in both ABMR and TCMR patients, characterized by the infiltration of inflammatory cells, predominantly T lymphocytes and macrophages, within the arterial intima [60]. In patients with i-IFTA, higher levels of Foxp3+ regulatory T cells (Treg) within graft infiltrates demonstrated a significantly superior five-year graft function trajectory compared to patients lacking intragraft Foxp3+ Treg cell infiltration [81]. Interestingly, methylation levels of the Programmed Cell Death Protein 1 (PD1) gene within the CD27-negative memory CD8+ T cell population were observed to be significantly elevated in transplant recipients experiencing rejection episodes [82].

2.2.5 Allograft rejection: antibody mediated

The Banff classification scheme denotes two primary phenotypes of antibody-mediated rejection (AMR): active AMR and chronic active AMR. ABMR is categorized into type 1, which occurs early in presensitized patients, and type 2, which occurs late and manifests as de novo antibodies. Among these, the latter is associated with a worse prognosis [61, 62]. While the precise mechanism of ABMR remains a mystery, prevailing theories suggest that initiation of a B cell alloresponse, which culminates in the generation of donor-specific antibody (DSA)-producing plasma cells, is a pivotal event in the allograft rejection process in ABMR. The interaction between donor-specific alloantibodies (DSAs) and donor Human Leukocyte Antigen (HLA) molecules, particularly HLA class II antigens displayed by endothelial cells in the microvascular circulation, is thought to serve as the initiating event for ABMR. The binding of DSAs to endothelial cells triggers a subsequent molecular cascade, including the activation of the complement system, which may contribute to endothelial dysfunction and microvascular inflammation and remodeling, leading to irreversible tissue injury [61, 83]. Fur-

thermore, mouse experiments indicate that B cell deficiency results in mitigated transplant glomerulopathy, reduced microvascular inflammation, diminished macrophage infiltration, and decreased interferon-gamma (IFNγ) transcripts in the allograft, further underscoring the central role of B cells in the pathogenesis of ABMR [84].

The role of NK cells in ABMR has garnered increasing scholarly interest as recent studies have shown that NK cells contribute to ABMR through their CD16a Fc receptors and the depletion of NK cells has been shown to significantly attenuate donor-specific alloantibody (DSA)-induced vasculopathy (CAV) [61]. NK cells can induce the production of IFNγ upon exposure to alloantigens via mechanisms akin to antibody-dependent cellular cytotoxicity. This elevated IFNγ production is correlated with an augmented risk for ABMR [85]. The presence of NK cell infiltration serves as a prognostic indicator for adverse outcomes following renal transplantation and some studies have also indicated that gene expression changes in endothelial cells or natural killer (NK) could serve as a valuable diagnostic tool for ABMR [86, 87]. Additionally, the ratio of T follicular helper cells to T follicular regulatory cells (Tfc/Tfr) has been identified as an independent risk factor for allograft dysfunction [61]. However, these potential biomarkers' diagnostic and prognostic utility still necessitates further study.

Complement C4d is a downstream byproduct of the complement activation pathway, and staining within peritubular capillaries and vasa recta commonly serves as an important diagnostic marker for ABMR. While C4d was initially considered a definitive marker for ABMR, ABMR can manifest even without C4d positivity, a phenomenon known as C4d-negative ABMR. Conversely, C4d staining may be observed without the occurrence of rejection, particularly in ABO-incompatible grafts. C4d deposition can occur without morphological signs of active rejection, and conversely, C4d may be absent in confirmed cases of ABMR. Additionally, donor-specific antibodies (DSAs) are far from a universal feature in ABMR [60, 61].

Glomerulitis on histology is often observed in the ABMR and is postulated to result from endothelial injury targeted towards human leukocyte antigens (HLA). Glomerulitis is

characterized by endothelial hypertrophy and the infiltration of immune cells, commonly leading to capillary luminal constriction and degradation. Other than B cells and plasma cells, the infiltrative cellular components may consist of T cells, monocytes, or neutrophils [60]. Transplant glomerulopathy is further characterized by the duplication or even multilayering of the glomerular basement membrane (GBM), and is often observed in ABMR and is believed to result from recurrent cycles of endothelial injury and subsequent repair. Another major histological feature, thrombotic microangiopathy (TMA) is frequently seen in the context of ABMR, particularly concerning endothelial injury. However, TMAs may also manifest in non-rejection scenarios, such as recurrent atypical hemolytic uremic syndrome or drug-induced conditions [60, 88]. TMAs are defined histologically by the presence of microthrombi, the widening of glomerular subendothelial spaces that appear electron-lucent, the deposition of amorphous material, and the neogenesis of a subendothelial basement membrane. Peritubular capillaritis is commonly associated with either active or chronic active ABMR, defined by the presence of both mononuclear and polymorphonuclear inflammatory cells within the frequently dilated lumens of peritubular capillaries. In ABMR, acute tubular injury is commonly seen; however, overt necrosis is relatively uncommon. Most frequently, the proximal tubular epithelial cells suffer injury, manifesting as cytoplasmic flattening, loss of brush borders, and luminal dilation [60, 61].

2.2.6 Allograft rejection: mixed phenotype

It is not infrequent for both chronic active TCMR and chronic active ABMR to co-occur, leading to an accelerated and particularly aggressive graft rejection phenotype called mixed-rejection (MR) [61]. Pre-existing TCMR has been empirically shown to correlate strongly with the subsequent development of chronic active ABMR with donor-specific antibodies (dnDSA) presence [89]. Additionally, histological analysis of biopsy-confirmed cases reveals that CD8+ T cells and macrophages are the predominant cellular infiltrates within the

glomerulus and TI in MR. Conversely, B cells are more frequently observed in the tubulointerstitial compartment. These observations would suggest that T cells and macrophages, and potentially their interplay, play a crucial role in the pathogenesis of renal chronic MR[90].

2.3 Common treatments

Immunosuppressive therapies adopted for graft survival can be categorized into three classes based on their functional roles in post-transplant care: induction agents, maintenance therapy, and rejection treatment agents.

Induction agents: These are employed to suppress the immune response acutely following transplant surgery to reduce the risk of early graft rejection. Induction therapy can be broken into two primary classes: Lymphocyte-Depleting Agents and Interleukin-2 (IL-2) Receptor Antagonists. Lymphocyte-depleting agents includes agents such as OKT3 (muromonab-CD3), equine anti-thymocyte globulin (ATGAM), rabbit antithymocyte globulin (rATG-Thymoglobulin), and alemtuzumab (Campath-1H). For IL-2 receptor antagonists, basiliximab is the predominant agent in this class. Relative to IL-2 receptor antagonists, lymphocyte-depleting agents exhibit higher potency, resulting in a lower incidence of acute rejection. However, this comes at the expense of an elevated risk for adverse complications, including susceptibility to infections and malignancies. Novel induction agents include alemtuzumab, efalizumab, and alefacept, which represent the emerging frontier in initial immunosuppression [57, 59].

Maintenance therapeutics: This category comprises agents administered over the long term to maintain a state of immunological tolerance towards the transplanted organ. Four major pharmacological subclasses exist within this framework: 1) Calcineurin Inhibitors (Cyclosporine and tacrolimus) 2) mTOR Inhibitors (Sirolimus and everolimus) 3) Antiproliferative Agents (Azathioprine and mycophenolic acid) and 4) Corticosteroids (Prednisone) [57, 59]. While calcineurin inhibitors (CNIs) have significantly improved kidney allograft

outcomes, there is growing apprehension in using CNIs due to concerns of CNI-induced nephrotoxicity. Alternative CNI-sparing strategies employing mTOR inhibitors or belatacept have been the subject of extensive investigation [59]. Belatacept can attenuate the activation of alloreactive B cells by interfering with the interactions between T-follicular helper cells and B cells in germinal centers, thereby inhibiting the formation of donor-specific antibodies (DSAs) [91, 83]. As it stands, Calcineurin Inhibitors (CNIs) continue to serve as the standard-of-care in the post-operative management of kidney transplant recipients. In multiple comparative studies, tacrolimus demonstrated a lower incidence of organ rejection, graft functionality and survival relative to cyclosporine. Accordingly, tacrolimus is recommended as the first-line CNI, except in cases where patients cannot tolerate its adverse effects [59].

Rejection treatment agents: These drugs are implemented when there are clinical signs of active graft rejection and typically constitute a more aggressive form of immunosuppression. The standard-of-care predominantly involves a much higher dose of calcineurin inhibitor-based regimen, with tacrolimus and mycophenolate mofetil as the primary therapeutic agents. Approximately 90% of kidney transplant recipients received either CNIs as monotherapy or in combination with adjunctive corticosteroid therapy [57, 92]. Tacrolimus is not without significant adverse effects that can critically influence patient well-being and graft longevity. Calcineurin inhibitors are efficacious in attenuating the incidence of acute rejection post-transplantation. However, CNI therapy can be accompanied by a constellation of adverse effects that range from nephrotoxicity and neurotoxicity, to metabolic dysregulation and electrolyte imbalances [57, 93, 94]. Immunosuppressive therapy, in general, also poses increased susceptibility to BK virus infection and disseminated varicella-zoster virus infection [57, 95].

CHAPTER 3

CELL DETECTION IN RENAL TISSUE

Multiplex microscopy (MMI) methods such as CODEX [96] and Imaging Mass Cytometry have revolutionized spatial biology and our understanding of the in situ context of cells, enabling us to capture an extraordinary level of data richness from biopsies. However, this same richness analyzes these images infeasible using traditional manual approaches. For our initial High-Resolution (HR) dataset, we hypothesized that differences in renal outcome would be related to differences in in situ adaptive immunity, such as frequency and organization of principal cellular effectors. Therefore, we stained each biopsy for 6 markers targeting the most prominent T cell lineages as well as dendritic cell subtypes: CD3, CD4, CD20, CD11c, BDCA2, and DAPI, to characterize: CD3+CD4+ T cells, CD3+CD4– T cells, CD20+ B cells, BDCA2+ pDCs, and CD11c+ mDCs.

Following the analysis of the HR dataset, we employed highly multiplexed (HMP) confocal microscopy to capture a more detailed picture of lymphocyte populations and a greater diversity of cell populations. Our HMP panel included additional markers to the ones in the HR panel, CD8, ICOS, PD1, FoxP3, CD20, CD138, and DAPI— to thoroughly characterize different aspects of the immune response within the renal tissue. To acquire this HMP dataset, we employed 4-color confocal microscopy in conjunction with iterative stripping and reprobing techniques to overcome the traditional limitations of fluorescent imaging. Furthermore, unlike traditional approaches focusing on isolated regions of interest (ROIs), this method involved imaging the entire biopsy sections; allowing for a more comprehensive and unbiased spatial analysis of the tissue, enhancing our understanding of the local immune landscape. With the experience gained in capturing these two renal datasets, along with months of marker development and validation, we have increased our MMI capture to an impressive 43 markers. Junting Ai spearheaded the bulk of this validation effort.

3.1 Biopsy samples

3.1.1 Sample selection

To probe the in situ differences between two common forms of renal inflammation, one autoimmune and one alloimmune, we acquired 54 archival blocks of kidney biopsies preserved as formalin-fixed, paraffin-embedded (FFPE) from the University of Chicago Human Tissue Resource Center. Within this, 25 blocks were from LN patients, 23 were from RAR patients, and six were from "normal" kidneys (Figure 3.1A). The LN biopsies were initially all clinically indicated diagnostic biopsies, while the RAR biopsies represented the earliest available rejection biopsy. It is crucial to emphasize that the procurement of renal biopsies is not a routine procedure and is typically conducted only when a notable clinical or laboratory anomaly necessitates such an invasive diagnostic approach. Consequently, this study's "normal" control samples were nephrectomy tissue derived from patients who did not have a preexisting autoimmune condition and exhibited no overt renal inflammation or damage on histological examination. In LN, biopsies are not routinely taken for surveillance but rather when a clinical or laboratory abnormality is highly suggestive of an LN diagnosis, and a biopsy is taken for confirmation of LN diagnosis in SLE patients [10, 38]. On the other hand, RAR biopsies are routinely taken as part of clinical surveillance and management of organ graft health, although the University of Chicago Medical Center does not adopt this invasive surveillance approach.

3.1.2 Patient demographics

Unfortunately, Dustin Shaw could only obtain limited clinical information from patient charts. Our LN cohort found that 14 LN biopsies were dsDNA positive, and the remaining 11 LN biopsies had unknown dsDNA status. (Figure 3.1C) Furthermore, 2 patients were noted as ESRD+, 8 patients were confirmed ESRD-, and the remaining 15 had unknown

ESRD status. Regarding pre-biopsy treatment, 4 patients were on prednisone therapy pre-biopsy, 4 patients were on pulse steroid therapy pre-biopsy, and 3 patients were confirmed to have received pre-biopsy MMF therapy. Interestingly, no patients reported using anti-CD20 Rituximab (Yes=0, No = 10, 15 Unknown). Unfortunately, the large number of "unknowns" means we cannot rule out that the additional samples have not received a therapeutic intervention that can alter the patient's immune profile. In terms of LN subtype representation, most of the biopsies are class 4 (n=11) and class 5 (n=7), while class 2 (n=2) and class 3 (n=3) were rare (Sup. 1A); 2 patients had unknown LN subtype. While our LN patients had a vast range in their respective age of SLE diagnosis (10-61 years), the average age of diagnosis was 25.75 $\pm$ 5.38 years. Interestingly, our biopsy samples were taken with an average of 4.08 $\pm$ 7.40 years post SLE diagnosis, with a wide range in age observed in this demographic as well (0-25 years post-diagnosis). As previously mentioned, in SLE, renal biopsies are only taken when there is a grave suspicion of LN, the wide range in which patients require a renal biopsy post-SLE diagnosis is further evidence of the heterogeneous nature of LN disease progression.

When looking at the patient characteristics of our RAR cohort, we find that we have a somewhat balanced representation of TCMR (n=10) and MR (n=14) graft rejection subtypes, while most of our biopsies come from deceased donors (n=15) versus living donors (n=3) (Figure 3.1D). It is good that we have a somewhat equal representation of TCMR/MR as that will decrease class-imbalance issues in our downstream analyses. Of these patients, 14 are medically compliant, 3 are not compliant, and 6 have unknown medical compliance status. We further find that 5 patients are diabetes Mellitus positive, while the majority (N=17) were negative. We again see a vast range of the patient's age at transplant (10-72 years) with an average age of 40.5 $\pm$ 19.5. Our RAR biopsies were on average, taken 2.43 $\pm$ 3.87 years post-transplantation with a range of 0 to 15 years. Interestingly, while our biopsies have no overt differences in the race or hypertensive status of our samples, we do see dissim-

ilarities in the mean age (25.75 ± 5.38 vs. 43.3±18.5) and sex ratio (88% Female vs. 35% Female) of our LN and RAR cohorts (Figure 3.1C-D), in line with expected demographic trends at initial diagnosis.

3.2 Marker panel development

The CODEX (CO-Detection by indEXing) technology employs an automated microfluidics system in conjunction with a standard fluorescent microscope to implement a series of processes, including hybridization, imaging, and removal of fluorescently labeled DNA probes. These probes are specifically designed to be complementary to antibodies that have been bound to tissue samples and conjugated with DNA. The system iteratively performs these steps, allowing for the high-throughput and multiplexed analysis of various tissue markers. This technological advancement addresses and mitigates the limitations of spectral overlap, a common issue encountered in multiplexing techniques. By doing so, not only improves the accuracy of the results but also minimizes batch-to-batch variations, enhancing the reliability and consistency of the data generated.

Using the LN accelerating medicines partnership (AMP) sc-RNA dataset and other descriptions of human LN in situ immunity, we developed and validated an antibody panel for 43 markers covering expected immune cells and common renal structures [97]. The panel is designed to encapsulate a broad range of cellular actors, targeting both renal cells vital to kidney physiology and various immune cell classes from innate and adaptive immune systems. Specifically, our panel encompasses renal cells such as inflamed tubules, proximal tubules, distal collecting tubules, and endothelial cells. Additionally, we incorporate probes for 15 different classes of immune cells alongside several markers indicative of cellular states. This multifaceted approach aims to provide a nuanced and comprehensive view of the cellular landscape involved in renal and immune functions.

Figure 3.1: Graphical abstract and patient demographics

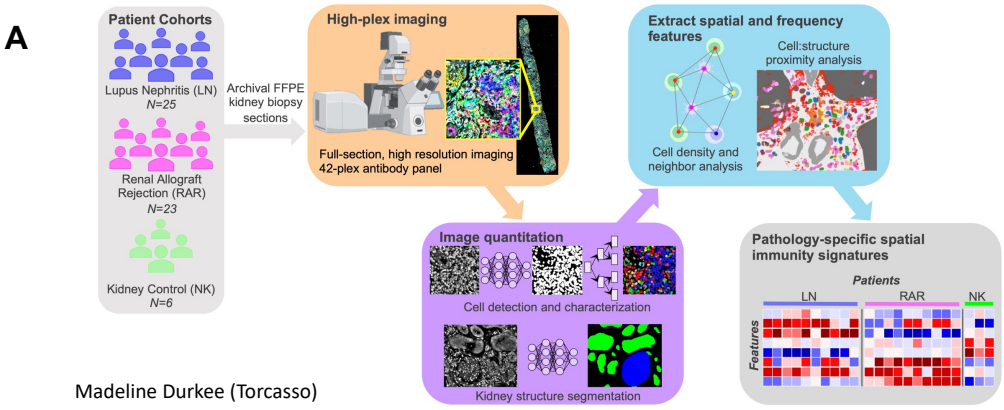

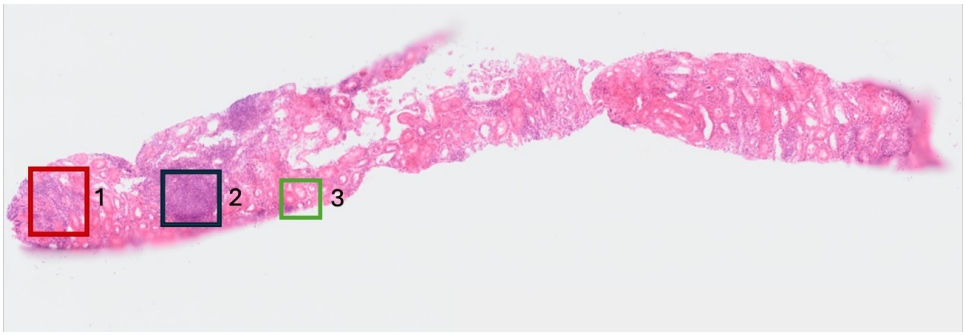

C

Patient characteristics				
Laboratory results	**μ**	**σ**	**n**	**Unknown (n)**
Serum creatinine at biopsy	3.67	±5.38	19	6
Serum creatinine (most current)	2.33	±2.39	16	9
C3	67.22	±26.55	10	15
C4	20.32	±28.93	10	15
Treatment Information		**Yes**	**No**	**Unknown (n)**
Pre-biopsy Prednisone > 20 ?		4	6	15
Pre-biopsy Pulse Steroid Therapy?		4	6	15
Pre-biopsy MMF Therapy?		3	8	14
Pre-biopsy Rituximab Therapy?		0	10	15
Other Information		**Yes**	**No**	**Unknown (n)**
dsDNA		14	0	11
ESRD+		2	8	15
Lupus Nephritis Subtype (n)				
2	2			
3	3			
4	11			
5	7			
Unknown	2			
Age at SLE diagnosis				**n**
Age, years (mean ± σ)	25.75	±16.0		12
Age range ,years	10-61			12
Post-diagnosis biopsy age				**n**
Age, years (mean ± σ)	4.08	±7.40		12
Age range ,years	0-25			12

D

Patient characteristics				
Laboratory results	**μ**	**σ**	**n**	**Unknown (n)**
Baseline Creatinine Post-Therapy	1.98	±0.76	16	7
Baseline Creatinine at Biopsy	3.25	±2.45	19	4
Tacroliminus levels	7.03	±3.40	14	9
Other Information		**Yes**	**No**	**Unknown (n)**
Medication Compliance		14	3	6
Diabetes Mellinus +		5	17	1
Acute Rejection Subtype (n)				
1A	13			
1B	7			
Unknown	3			
Allograft Rejection Subtype (n)				
T-cell Mediated Rejection	10			
Mixed Rejection	12			
Donor type (n)				
Deceased	15			
Living, Related	1			
Living, Unrelated	2			
Unknown	5			
Age at transplant				**n**
Age, years (mean ± σ)	40.5	±19.5		23
Age range ,years	10-72			23
Age at biopsy				**n**
Age, years (mean ± σ)	43.3	±18.5		23
Age range ,years	15-73			23
Post-transplant biopsy age				**n**
Age, years (mean ± σ)	2.43	±3.87		23
Age range ,years	0-15			23

A) Graphical abstract of the dissertation. B) Representative image of a core needle biopsy sample with Hematoxylin & Eosin staining. Gross anatomical features are shown: 1) interstitial inflammation 2) Glomerulus 3) tubules. C) Summary table of patient descriptors and characteristics for Lupus Nephritis patients. D) Summary table of patient descriptors and characteristics for Renal Allograft Rejection patients.

Figure 3.2: Renal cell markers: CD10, MUC1, and claudin-1

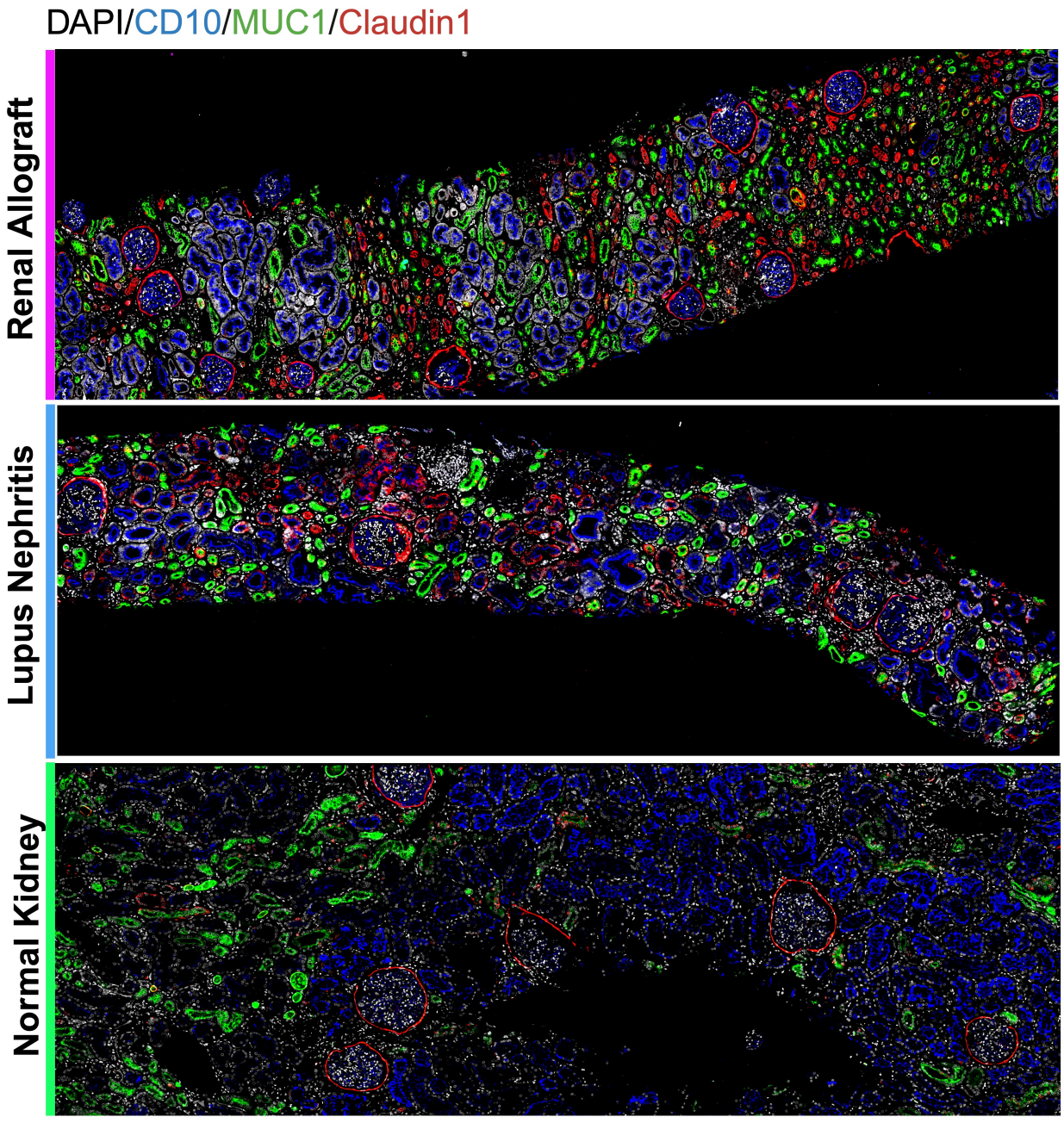

A) Representative images of renal cell markers, CD10 (proximal tubules), MUC1 (distal tubules), claudin-1 (tubular stress), and DAPI (cell nulcei) within our biopsy cohorts. (Bottom) normal kidney, (middle) lupus nephritis, and (top) renal allograft rejection.

Figure 3.3: Pan-lineage immunophenotyping: CD45, CD3, and HLAII

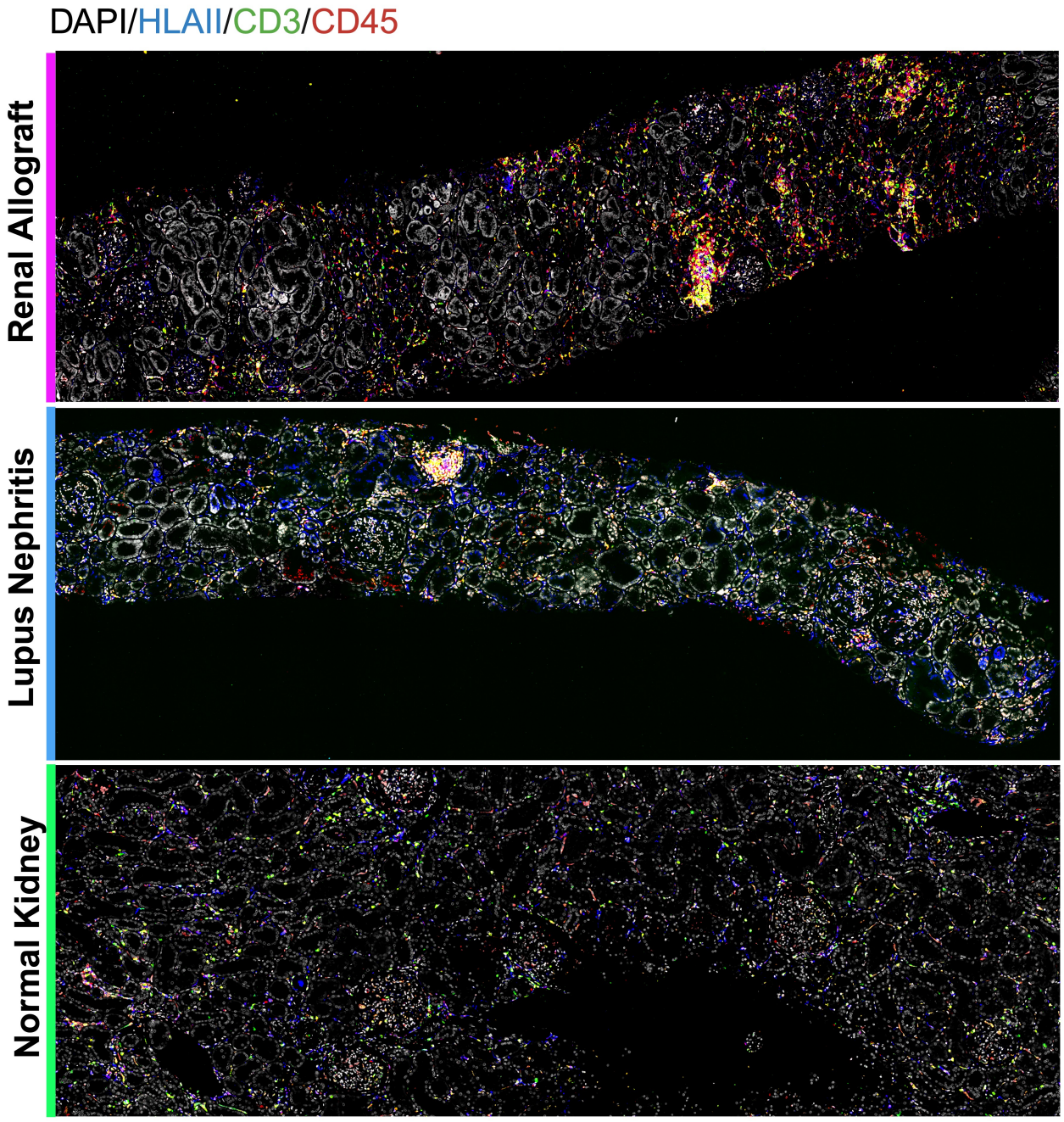

A) Representative images of immune cell markers, HLAII (professional antigen-presenting cells; APCs), CD3 (pan-T-cell marker), CD45 (pan-immune), and DAPI (cell nulcei) within our biopsy cohorts. (Bottom) normal kidney, (middle) lupus nephritis, and (top) renal allograft rejection.

Figure 3.4: Renal and pan-immune markers – zoomed

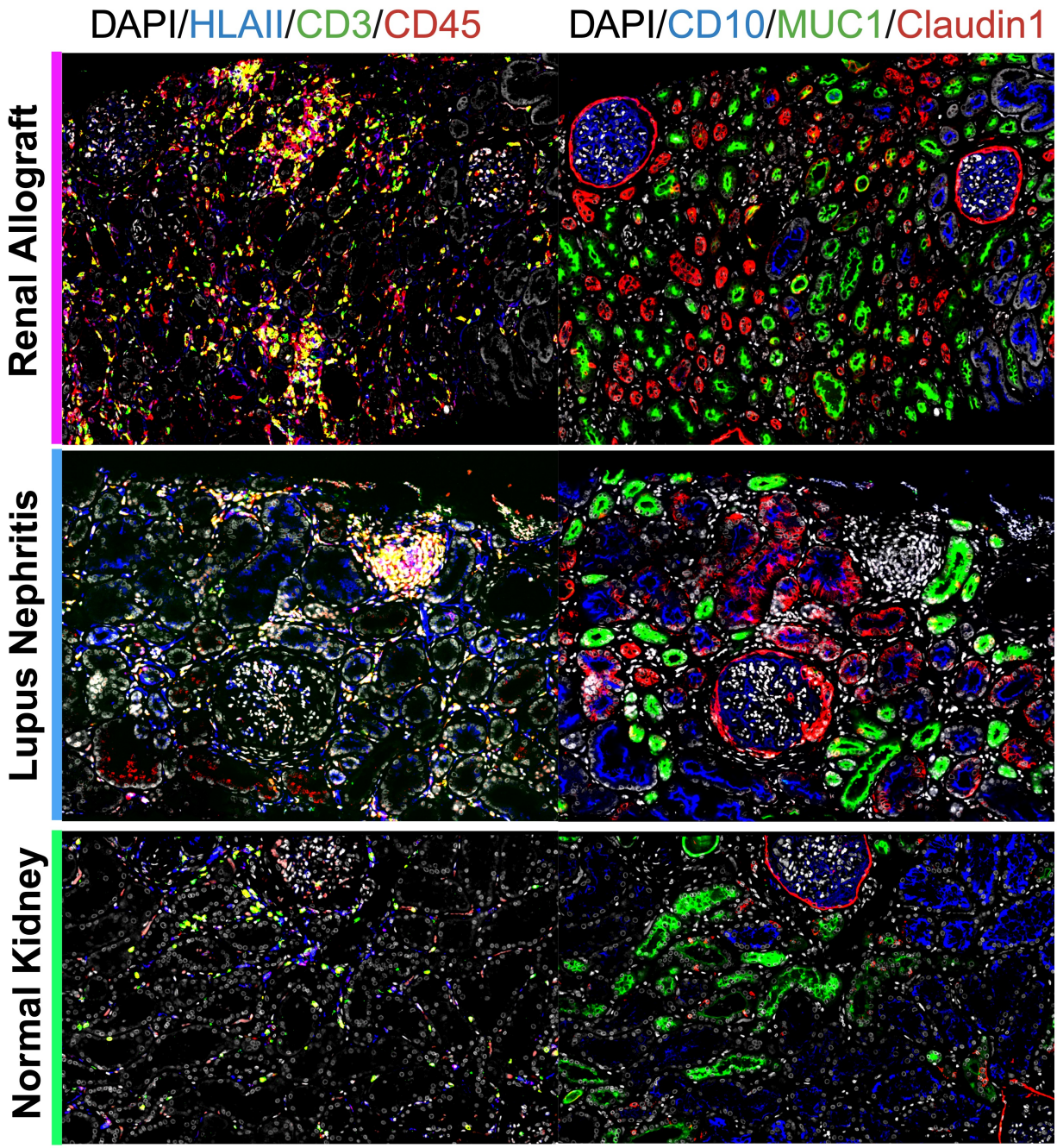

A) (Left) Representative images of immune cell markers, HLAII (professional antigen-presenting cells; APCs), CD3 (pan-T-cell marker), CD45 (pan-immune), and DAPI (cell nulcei) within our biopsy cohorts. (Right) Representative images of renal cell markers, CD10 (proximal tubules), MUC1 (distal tubules), claudin-1 (tubular stress), and DAPI (cell nulcei) within our biopsy cohorts. (Bottom) normal kidney, (middle) lupus nephritis, and (top) renal allograft rejection.

3.2.1 Renal cells: non-immune lineages

In this study we include canonical markers of renal non-immune cells: MUC1, CD10, CD31, and claudin1 (Figure 3.2). MUC1 (Mucin 1) is a glycoprotein expressed on the apical surface of epithelial cells, particularly the distal convoluted tubular cells in the kidney, where it protects the epithelial layer and maintains barrier function [97]. CD10, on the other hand, is expressed on the brush border of proximal tubular epithelial cells in the kidney and plays a role in reabsorption and peptide degradation. This enzymatic activity is essential for the breakdown of small peptides, helping to fine-tune physiological processes like fluid balance and blood pressure regulation by the kidney [97, 98]. CD31, also known as Platelet Endothelial Cell Adhesion Molecule-1 (PECAM-1), is primarily found on the surface of endothelial cells and platelets, including those in the kidney's vasculature. In the immune system, CD31 plays a role in leukocyte migration, facilitating the passage of immune cells through the endothelial layer to sites of inflammation or infection, as well as in maintaining vascular integrity [16, 99]. Claudin-1 and molecules can pass through the intercellular spaces between the tubular epithelial cells, thereby contributing to the overall regulation of electrolyte balance and fluid homeostasis. However, claudin overexpression in response to stress or injury has been reported previously, potentially serving as an indicator for renal stress [100, 101]. Within our cohorts, we also observe tubular overexpression of claudin1 in our LN and RAR samples. The NK control on, the other hand, has claudin1 expression limited to Bowman's Capsule. This data would align with literature reports of claudin1's link to tubular stress. Interestingly, we further see a generalized underexpression of the canonical tubular markers in the autoimmune and alloimmune cohorts, while the NK samples maintain higher basal levels of MUC1 and CD10 expression (Figure 3.2). This observation is later considered when we design our biology-based cell classification decision tree.

3.2.2 Non-lineage-specific protein markers

DAPI (4',6-diamidino-2-phenylindole) staining is a fluorescence-based technique used to visualize the nucleus of cells. DAPI primarily stains DNA and is thus not specific to any particular cell type, it is often used in conjunction with other markers to identify and localize cells in tissue [97, 26, 49] (Figure 3.2-4). Perforin and granzymes are cytotoxic proteins that play a crucial role in the immune system's ability to eliminate target cells. Granzymes (GZMK/GZMA/GZMB) are serine proteases released by cytotoxic T lymphocytes and natural killer (NK) cells to induce apoptosis in target cells, such as virus-infected or cancer cells. Perforin creates pores in the plasma membrane of the target cell, serving as the entry point for granzymes Once inside the target cell, granzymes activate various cellular pathways that lead to apoptosis, essentially instructing the cell to undergo a regulated form of death [16, 102]. The Microtubule Organizing Center (MTOC) is a cellular structure responsible for the nucleation and organization of microtubules; it is essential for various cellular processes, including cell division, cell movement, signaling, and intracellular transport. mTOC will notably position itself towards the lymphocyte:target cell-cell border during the immune synapse formation [103]. CD43, a large mucin molecule, exhibits spatial segregation during immune synapse formation by localizing away from the T cell receptor (TCR) engagement site, accumulating in a membrane domain on the opposite side [104].

Interferon (IFN) is a multifunctional cytokine synthesized in reaction to viral infections, playing pivotal roles in immunity, antiviral defense, and antitumor activities. IFNs are categorized into three primary types: Specifically, Type I IFNs encompass subtypes like IFN-alpha, IFN-beta, IFN-epsilon, IFN-kappa, and IFN-w; IFN-γ primarily represents Type II IFN; and Type III IFNs include IFN-lambda variants. IFN-γ, is chiefly produced by Th1 CD4+ T cells, cytotoxic CD8+ T cells, and natural killer (NK) cells. To a lesser extent, dendritic cells (DCs), macrophages, and B cells contribute to IFN-gamma production. IFN-γ has garnered particular interest in systemic lupus erythematosus (SLE) pathophysiology.

Elevated levels of IFN-γ have been observed in the serum of SLE patients compared to healthy controls; however, due to inconsistencies in serum laboratory results, the expression of interferon response genes is preferred. The abnormal accumulation of IFN-γ has been detected even before the clinical onset of SLE and before the emergence of autoantibodies and IFN-alpha. This suggests that IFN-γ may serve as an early biomarker and a key player in the pathogenesis of SLE and LN [105].

The human myxovirus resistance protein 1 (MxA), an example of an IFN response gene, is pivotal in the antiviral defense orchestrated by type I and III interferons. Its expression is stringently modulated via signal transducer and activator of transcription 1 (STAT1) signaling pathways rather than directly induced by viral infections or other external triggers. This makes MxA a versatile yet tightly controlled effector molecule in the interferon-mediated antiviral response against a broad spectrum of viral pathogens. MXA can also be utilized in tissue staining to study the presence of interferon response in tissue [49, 106]. Collagen III (often denoted as Collagen Type III or COL3) is a fibrous protein found in connective tissues, including those in the kidney, involved in the extracellular matrix structure and organ structural integrity. In the context of the immune system, collagen types can play a role in tissue repair and remodeling, especially during inflammation or injury. Abnormal collagen deposition, such as in fibrotic conditions, could affect kidney function and local immune responses. Type III collagen is a unique fibrillar collagen forming homotrimeric right-handed triple helixes. Secreted primarily by fibroblasts and various mesenchymal cells, this collagen subtype is a key component of the interstitial matrix and is significantly implicated in inflammation-related pathologies, such as pulmonary damage, hepatic diseases, renal fibrosis, hernia, and vascular anomalies. During tissue repair, Type III collagen is a dynamic scaffold that facilitates fibroblast attachment and modulates wound architecture, enhancing scar tensile strength over time [107]. The human Ki-67 protein serves as a precise marker for cellular proliferation due to its unique expression patterns across different cell

cycle phases. Exclusively nuclear in interphase, Ki-67 undergoes a striking relocalization to the chromosomal surface during mitosis. Its presence across all active cell cycle phases—G1, S, G2, and mitosis—while conspicuously absent in quiescent cells (G0), establishes Ki-67 as a robust indicator for evaluating the growth fraction within diverse cellular populations [108].

CD45 or leucocyte common antigen, is a crucial transmembrane glycoprotein found on nearly all hematopoietic cells, excluding mature erythrocytes. It is a vital modulator in the antigen receptor-mediated activation of T and B lymphocytes [109] (Figure 3.3). HLA class I molecules are ubiquitously displayed on nearly all nucleated cells, while HLA class II molecules are selectively expressed on B lymphocytes, antigen-presenting cells like monocytes, macrophages, dendritic cells, and activated T cells. These HLA molecules are instrumental in presenting a diverse range of antigenic peptides to T cells, thereby facilitating the immune system's ability to distinguish between self and foreign antigens [110, 111]. CD86 is a 70-kDa glycoprotein consisting of 329 amino acids and features a transmembrane region and a more extended cytoplasmic domain than CD80. It is inherently present in various antigen-presenting cells, including interdigitating dendritic cells (DCs), Langerhans cells, peripheral blood DCs, and memory and germinal center B cells and macrophages. Its expression is also inducible in monocytes, particularly when stimulated by IFN-γ [112].

CD69 is part of the C-type lectin family and is an early activation marker for leukocytes, notably T and B cells. CD69 is further expressed in tissue-resident memory T cells (CD4+/CD8+) [97, 113]. In some chronic human inflammatory disorders such as SLE, CD69 expression is upregulated and associated with tissue-infiltrating lymphocytes. In these settings, CD69 expression may contribute to perpetuating the inflammatory response. CD69 has also been reported to have an immunoregulatory function, highlighting a more nuanced role. In various studies, the absence of CD69 was associated with a predisposition to inflammatory and autoimmune conditions. The molecule is suggested to contribute to immuno-

logical homeostasis, mainly through the regulation of T helper cells (Th) and regulatory T cells (Tregs); it is believed that CD69 can favor the suppressive functions of Tregs [97, 114].

3.2.3 Renal cells: T-cell lineages

CD3 is the canonical pan-T-cell protein marker that serves as a critical T-cell co-receptor for activating cytotoxic T cells (CD8+ naive T cells) and T helper cells (CD4+ naive T cells). In mammals, the CD3-complex is a multi-chain assembly comprising CD3-γ, CD3-δ, and two copies of CD3-ϵ chains. These distinct chains work with the T-cell receptor (TCR) and the CD3-ζ chain, forming an integral part of the TCR-CD3 complex essential for T-cell activation and signaling. CD4, or cluster of differentiation 4, is a membrane glycoprotein that acts as a co-receptor for the T-cell receptor to facilitate T cell activation and signaling. This co-receptor plays a crucial role in the adaptive immune response by enabling specific binding to antigen-presenting cells. While primarily expressed on the surface of T helper cells, CD4 is also found on other immune cells, including monocytes, macrophages, and dendritic cells. Similarly, CD8 is a transmembrane glycoprotein functioning as a co-receptor to the T-cell receptor. It is predominantly expressed on the surface of cytotoxic T cells and plays an instrumental role in the effector function of these immune cells. By interacting closely with the TCR, CD8 enhances the specificity and strength of the cytotoxic T cell's interactions with antigen-presenting cells, thereby contributing to effective adaptive immune responses.

Most adaptive immune T cells express T-cell receptors α and β (TCR$\alpha\beta$) along with either CD4 or CD8 co-receptors. In contrast, double-negative (DN) T cells are CD3 positive but lack CD4 and CD8 co-receptors. These cells can express either TCR alpha-beta or TCR γ and delta and do not exhibit natural killer (NK) T cell markers. DN T cells functionally display innate and adaptive immune capabilities, setting them apart from conventional CD4+ and CD8+ T cells. $\gamma\delta$ T-cells possess a unique TCR composed of a γ and a delta chain,

distinct from the alpha-beta TCR found in conventional T cells [16, 49, 25, 103, 115]. In humans, about 95% of T cells express TCR alpha-beta and the remaining 5% express TCR$\gamma\delta$. Within the DN T cell population, both TCR$\alpha\beta$+ and TCR$\gamma\delta$+ subsets exist [115, 116].

The transcription factor RAR-related orphan receptor γt (RORγt) is critical for differentiating Th17 cells and their production of signature cytokines, and is commonly used as the hallmark protein marker for this Thelper subpopulation. RORγt is necessary for both homeostatic Th17 cells, which help regulate the commensal microbiota at mucosal barriers, and pro-inflammatory Th17 cells whose dysregulation can lead to autoimmune and chronic inflammatory diseases [117]. Interleukin-10 (IL-10) is a pleiotropic cytokine with diverse immunoregulatory functions produced by many immune cell types. In addition to macrophages and regulatory T-cells, IL-10 is secreted by CD8+ and CD4+ T cells, particularly the CD4+ Th2 cells, $\gamma\delta$ T cells, natural killer (NK) cells, natural killer T (NKT) cells, B cells, dendritic cells, eosinophils, and mast cells [118]. Another significant T-cell protein marker, Forkhead box P3 (Foxp3), is a crucial transcription factor that is the master regulator for developing and differentiating CD4+ regulatory T cells (Tregs). Initially considered the sole specific marker for Tregs, Foxp3 is crucial in down-regulating immune responses. Tregs, often abundant in tumor tissues and involved in human autoimmunity, specialize in negative regulation of the immune system [49, 97, 119].

T-cell markers such as Inducible T-cell COStimulator (ICOS), also known as CD278, play a critical role in T-cell activation and function. ICOS is a potent costimulatory molecule that can amplify T cell responses when ligated with ICOS-L (ICOS ligand). ICOS-L,is found constitutively on antigen-presenting cells such as dendritic cells (myeloid and plasmacytoid), macrophages, and B cells. ICOSL is also found on non-hematopoietic cells, like vascular and alveolar epithelial cells. The interaction between ICOS and ICOS-L initiates several downstream signaling pathways that contribute to cell survival, proliferation, cytokine production, and other functions that sustain an immune response over time. In the context

of Th2 cells, ICOS signaling can promote the secretion of Th2 cytokines like IL-4, IL-5, and IL-13, which are involved in B cell class switching, eosinophil recruitment, and other processes that characterize a Th2 response [120]. ICOS is particularly notable for its high expression on T follicular helper (TfH) cells in germinal centers. ICOS signaling in TfH cells is crucial for the regulation of B cell responses and for the formation of high-affinity antibodies. Its interaction with its ligand, ICOSL (or B7RP-1), enables the fine-tuning of humoral immunity, a critical arm of the adaptive immune system that involves antibody production. ICOS also plays a role in differentiating and functioning various T cell subsets besides TfH cells, such as Th1 and Th17 cells [16, 121].

Programmed cell death protein 1 (PD-1, or CD279) is an important immune checkpoint receptor critical in immune homeostasis and self-tolerance. Like ICOS, PD-1 is also a member of the CD28 superfamily of costimulatory molecules and is expressed mainly on activated T cells and B cells. It serves as a key regulator of immune responses by delivering inhibitory signals upon interaction with its ligands, PD-L1 and PD-L2, expressed on tumor and antigen-presenting cells. One of the primary mechanisms by which PD-1 prevents autoimmunity is promoting the apoptosis of activated, antigen-specific T cells; eliminating self-reactive T cells that could potentially cause autoimmune diseases. Ligation of PD-1 also inhibits the production of key cytokines IL-2, IL-7, IL-10, and IL-12. This has a dampening effect on the immune response by reducing T cell activation and proliferation, as well as affecting the function of macrophages and NK cells. This inhibition is relevant in autoimmune conditions, where immune suppression may be beneficial, and in cancer, where it can be detrimental by preventing effective anti-tumor responses. PD-1 also maintains the population of regulatory T cells, which are critical for suppressing inflammatory responses and maintaining immune tolerance [16, 121, 122]. The double expression of ICOS and PD1 on CD4+ T cells is often used to label TfH cells (CD4+ICOS+PD1+) [97, 49].

3.2.4 Renal cells: myeloid cell lineages

The advent of flow cytometry in the 1970s revolutionized the study of monocytes by allowing for the identification of specific subsets based on surface markers. Human monocytes are broadly categorized into three main groups: classical (CD14+CD16-), non-classical (CD14dimCD16+), and intermediate (CD14+CD16+). These subsets differ not only in their surface marker expression but also in their roles in homeostasis and disease states. Notably, the number of CD14+CD16+ intermediate monocytes increases in the blood of patients with systemic infections [123, 97, 124]. CD68 protein is considered a pan-macrophage/monocyte marker and is commonly used in research and clinical settings to identify macrophage lineage cells. CD68 is a glycosylated type I membrane protein primarily found in macrophages' late endosomes and lysosomes. It belongs to the scavenger receptor family and is a member of the lysosome-associated membrane protein (LAMP) family. In addition to macrophages, CD68 is also found on other cells within the monocyte lineage such as dendritic cells (DCs) and osteoclasts. It is highly expressed by circulating monocytes and tissue-specific macrophages like Kupffer cells in the liver and microglia in the brain [101].

To capture essential macrophage functional/immune subtypes we include markers such as iNOS, CD163, and Mertk. Nitric oxide (NO) is a versatile molecule involved in various physiological processes, including neurotransmission, vascular regulation, and immune function. It is synthesized by nitric oxide synthase (NOS), with the inducible form (iNOS) being particularly interesting in immune regulation. iNOS is often expressed in M1 macrophages, serving as a hallmark protein marker, and is induced by Toll-like receptor (TLR) ligands and inflammatory cytokines like IFN-gamma. This molecule is pivotal in host defense as a pro-inflammatory cytotoxic agent that can neutralize various pathogens. Interestingly, iNOS also impacts the balance between M1 and M2 macrophages by modulating the transcription factor IRF5. Additionally, NO has been found to inhibit the production of IL-12 in dendritic cells and macrophages, suggesting a regulatory role in innate immunity [16, 124, 125, 126].

CD163, a transmembrane scavenger receptor, is predominantly expressed on macrophages and serves as an endocytic receptor for several ligands, most notably the haptoglobin-hemoglobin complex. The receptor is commonly associated with anti-inflammatory or "M2" macrophages and is often used as a marker to identify this subset of macrophages. The local cytokine milieu regulates the expression of CD163. Anti-inflammatory cytokines like IL-6 and IL-10 tend to induce its expression, while pro-inflammatory stimuli such as IL-4, TNF-α, IFN-γ, and LPS generally repress CD163 expression. In pathological conditions like lupus nephritis, an increased infiltration of CD163+ macrophages is associated with worse renal function and a higher disease activity index [16, 124, 125, 127]. On the other hand, MerTK (Mer tyrosine kinase) is a member of the TAM (Tyro-Axl-MerTK) family of receptor tyrosine kinases, predominantly expressed on macrophages. MerTk plays a crucial role in efferocytosis, in which macrophages engulf and remove apoptotic cells. MerTK interacts with apoptotic cells via bridging molecules Gas6 or protein S, facilitating the recognition and binding to phosphatidylserine exposed on the surface of apoptotic cells. Upon activation through engagement with apoptotic cells, Gas6, or protein S, MerTK initiates two critical responses: anti-inflammation and pro-resolution. These processes are essential for maintaining tissue homeostasis and immune balance. The anti-inflammatory response is characterized by suppressing NF-kB (nuclear factor kappa B)-mediated signaling pathways, reducing pro-inflammatory mediators' production. In mouse models, genetic ablation of MerTK leads to the development of chronic inflammatory diseases, including a lupus-like condition in older mice and atherosclerosis in hypercholesterolemic mice. These findings underline the importance of MerTK in preventing inappropriate or excessive inflammation and facilitating the resolution of inflammatory processes [16, 128].

CD56, also known as Neural Cell Adhesion Molecule (NCAM), is a protein primarily recognized as a marker for Natural Killer (NK) cells. CD56 belongs to the immunoglobulin superfamily and is involved in homophilic (binding to the same molecule) and heterophilic

(binding to different molecules) interactions. Although the expression of CD56 is most strongly associated with NK cells, it is not exclusive to this cell type. In humans, NK cells are often defined phenotypically by the expression of CD56 in the absence of CD3, a TCR complex protein mentioned previously. CD3 negative expression helps differentiate them from T cells and categorizes them within the innate lymphoid cell (ILC) family, part of the broader immune system responsible for early, non-specific responses to pathogens. Besides NK cells, CD56 is found on other immune cells such as $\gamma\delta$T cells and activated CD8+ T cells. It is also expressed on dendritic cells (DCs), crucial for initiating adaptive immune responses [97, 129]. SLAMF7 (Signaling Lymphocytic Activation Molecule Family member 7), also known as CS1, CRACC, and CD319, is a receptor that has emerged as a key player in the regulation of immune responses, particularly in NK (Natural Killer) cells and monocytes/macrophages. SLAMF7 is a self-ligand receptor, found to downregulate the expression of pro-inflammatory cytokines like TNFs and IL-12p70 in human monocytes, although the exact mechanisms behind this regulation are not yet fully understood. Additionally, SLAMF7 has been shown to have a negative regulatory effect on inflammation in certain infectious diseases. For example, elevated levels of SLAMF7 in macrophages can reduce corneal inflammation by encouraging M2 macrophage polarization. It also diminishes IFN-α–mediated CXCL10 production in chronic HIV infections [125, 130].

3.2.5 Renal cells: dendritic cell lineages

BDCA1 (Blood Dendritic Cell Antigen 1, also known as CD1c), BDCA2 (Blood Dendritic Cell Antigen 2, also known as CD303), CD103, and CD11c are membrane proteins associated primarily with different dendritic cell subsets. Dendritic cells (DCs) serve as pivotal immune regulators that bridge innate and adaptive immune systems, playing a crucial role in initiating and modulating immune responses. DCs possess specialized pattern recognition receptors (PRRs) that detect both pathogen-associated molecular patterns (PAMPs) and

damage-associated molecular patterns (DAMPs). This recognition leads to DC activation, antigen uptake, cross-presentation, and the subsequent initiation of antigen-specific adaptive immune responses. In humans, three major DC subsets with distinct functional specializations are present in peripheral blood and lymphoid tissues: conventional DCs are classified into type 1 (BDCA3/CD141/CD103+ DCs, cDC1s) and type 2 (BDCA1/CD1c/CD11c+ DCs, cDC2s), and there are also plasmacytoid DCs (BDCA2+ DCs, pDCs). These subsets vary in aspects such as surface marker expression, localization, migratory capabilities, Toll-like receptor (TLR) expression, antigen processing and presentation capacities, as well as cytokine secretion profiles [97, 131, 49, 124, 125]. cDC2s represent the predominant DC population in peripheral blood and lymphoid organs and exhibit unique features that enable them to complement other DC subsets. However, our group has long reported that pDCs play a prominent in situ pathogenic role in LN biopsies [25, 26, 49].

3.2.6 Renal cells: humoral cell lineages

CD20, a surface protein encoded by the MS4A1 gene, is a crucial pan-B cell marker commonly used in immunohistochemistry. Its expression initiates at the pro-B cell stage and intensifies as the cell progresses toward full maturation [132]. CD138, or Syndecan-1, is a type I transmembrane heparan sulfate proteoglycan encoded by the SDC1 gene. It is a member of the syndecan proteoglycan family, integral to various cellular processes such as adhesion and signaling. In humoral immunity, plasma cells, which are pivotal producers of antibodies, can be uniquely identified by their expression of CD138 [6]. CD27 is a surface molecule expressed on various resting immune cells, including CD4+ and CD8+ T cells and natural killer (NK) cells. Interestingly, its expression is reduced in effector T cells but maintained in memory CD4+ T cells. In the B-cell lineage, CD27 is expressed across memory B cells (MBCs), germinal center (GC) B cells, and plasma cells (PCs), with the highest levels found in PCs. This marker is often employed as a key identifier for human memory B cells and an

indicator of B-cell activation [133]. CD21, is a membrane protein encoded by the CR2 gene in humans, specifically binding to complement components like iC3b, C3dg, or C3d. B cells express CR2 on their surfaces, implicating the complement system in B-cell activation and maturation processes. Importantly, elevated levels of CD21low B cells are often observed in patients with systemic lupus erythematosus (SLE), where they are associated with B cell lymphopenia [134, 135]. These cells are commonly found in patients with autoimmune disorders, suggesting a potential role in disease pathology. T-bet, also known as T-box transcription factor TBX21, is a protein encoded by the TBX21 gene in humans. This gene belongs to the T-box family, a group of evolutionarily conserved genes known for their shared DNA-binding domain. T-box genes function as transcription factors that play crucial roles in regulating various developmental pathways. The recently identified B cell subset, termed Age-Associated B Cells (ABCs), is characterized by its expression of the T-bet transcription factor. This subset tends to accumulate with aging and is observed in both viral infections and autoimmune conditions across mice and humans [136, 16]. defined their activated B cell subset as CD21-CD27+ B cells and age-associated B-cells as CD20+CD21-T-bet+ in their LN study [16].

3.3 Marker validation and imaging

3.3.1 Imaging and preprocessing

FFPE tissue sections underwent deparaffinization and were subsequently subjected to staining utilizing a combination of primary and secondary antibodies. These secondary antibodies were conjugated with fluorophores, including Alexa Fluor 488, Atto550, Cy5/AF647, and AF750. Comprehensive images of the entire biopsy sections were captured employing an Andor Dragonfly 200 Spinning Disk Confocal Microscope, with a pixel size of 0.1507μm. The implementation of the 42-marker panel was accomplished through iterative staining and

Figure 3.5: CODEX stain example

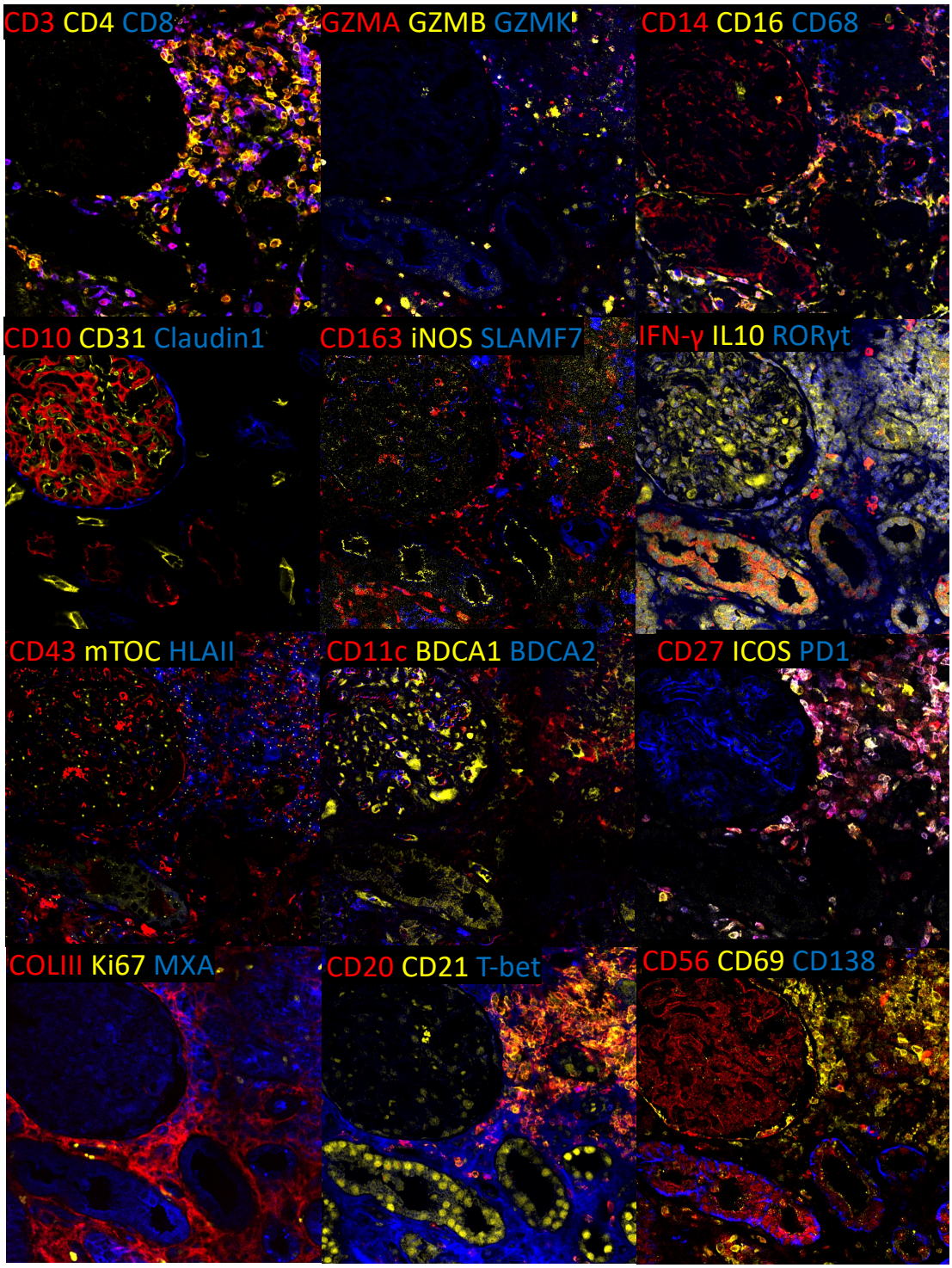

Example images of CODEX marker stains on renal FFPE core needle biopsy tissue; grouped thematically.

imaging, executed using the previously described PhenoCycler platform [96]. Additionally, Tissue Autofluorescence (TAF) images were procured at every imaging wavelength to facilitate background subtraction and spectral normalization. Subtracting TAF images from the captured images, was pivotal in enhancing the precision of the subsequent analyses by mitigating the impacts of inherent tissue fluorescence, thus ensuring the integrity and accuracy of the fluorescence signals attributed to the antibody-based staining. Ashlar [137] was used to stitch image tiles into a full-section composite and align the resulting channels. All computational tasks were performed on the MEL server in the Radiomics and Machine Learning Facility at the University of Chicago. MEL has 256 Xeon Gold 6130 CPU cores, 3 TB of DDR4 ECC RAM, 24 TB NVMe SSD storage space, and 16 Nvidia Tesla V100 32GB GPU accelerators.

Figure 3.5 shows representative staining of a peri-glomerular immune infiltrate in a LN biopsy. This example shows that our T-cell markers such as CD3/CD4/CD8 have good signal-to-background staining. We see evidence of CD3+CD4+ T-cells (Thelper), CD3+CD8+ T-cells (Tcytotoxic), as well as CD3+CD4-CD8- (DN T-cells) in line with our previous LN datasets. Granzyme expression within CD3+CD8+ T-cells displayed great heterogeneity, with GZMA-GZMB+GZMK- and GZMA+GZMB-GZMK+ cells. Notably, while the gene encoding human GZMB resides on chromosome 14, the genes for GZMA and GZMK are closely positioned on chromosome 5 [138, 139]. This physical separation of GZMB from GZMA and GZMK may imply distinct transcriptional regulatory control, though the specifics of which remain largely unexplored [140, 141]. Furthermore, we also see the expression of important T-cell functional markers ICOS, PD1, and CD27. This particular sample shows evidence of CD4+ICOS+ T-cells, CD4+PD1+ T-cells, and CD4+ICOS+PD1+ T-cells (T follicular helper).

Humoral lineage markers such as CD20, CD138, and CD21 also had the expected expression pattern. This particular immune infiltrate appears rich in CD20+ B-cells with some

presence of CD20+CD21+ B-cells, while CD138+ plasma cells were rare here. APC marker HLAII and the myeloid markers CD14, CD16, and CD68 had appropriate signal-to-noise levels. We note here the presence of classical HLAII+CD68+CD14+CD16- macrophages, as well as to a lesser extent non-classical HLAII+CD68+CD14-CD16+ macrophages. The intermediate HLAII+CD68+CD14+CD16+ macrophage phenotype discussed previously is also observed in rare frequencies. Dendritic cell markers CD11c, BDCA1, and BDCA2 displayed significant heterogeneity in expression. We observe evidence of CD11c+BDCA1-BDCA2- DCs, CD11c-BDCA1+BDCA2- DCs, and CD11c-BDCA1-BDCA2+ DCs. This immune cell infitrate is particularly rich in CD11c+ DCs with some BDCA2+ DCs. Interestingly, we see BDCA1 expression on non-immune renal cells within glomeruli.

The mTOC marker had the expected high-fidelity, high-intensity, punctate signal we observed previously [25]. Based on observation, we did not believe the current CD43 staining would be helpful for cognate cell identification as its staining pattern was too non-specific for our purposes. Renal markers such as CD10, CD31, and Claudin 1 also displayed low background staining and canonical expression patterns within Bowman's Capsule. Extracellular markers such as COLIII (tissue fibrosis/scarrification) and MXA (IFN-γ signaling) also displayed rubust expression. Here we observe that MXA expression is enriched within the peri-glomerular immune infiltrate, with some minor expression in tubules proximal to the immune infiltrate. On the other hand, we see that COLIII deposition is mainly limited to stromal areas between renal structures such as glomeruli and tubules and around the immune cell infiltrate (rather than within like MXA). Thus, I postulated that an MXA mask would be able to capture areas of high active inflammation while a COLIII mask would provide a general estimate of tissue health. Some other markers, such as RORγt, IL-10, and T-bet displayed high levels of background staining and, as a result, were not included in the downstream decision tree classifier gating scheme (a practical advantage of the method for dealing with undesirable signal). Overall, we were content with the development of this marker panel

and were confident we could move forward with this panel for all biopsy samples.

3.4 Cell detection in multiplex microscopy imaging

Multiplex microscopy imaging (MMI) at 40+ markers allows for the capture of an unprecedented level of detail from tissue samples. However, the complexity introduced by this same richness makes analyzing these images with traditional manual approaches infeasible. This can often take up to 100+ of manhours [142, 143, 144] on relatively more straightforward image tasks; the extension to a 40+ marker multiplex is overwhelming for a human to perform accurately, much less in a high-throughput manner. It quickly becomes apparent why digital pathology and spatial microscopy fields have turned to computer vision (CV) methods. CV techniques have become increasingly utilized for multiplex microscopy data; however, classical methods such as active contouring [145], pixel thresholding [146], and fuzzy c-means [147] have been fundamental for CV but do not generalize well across images of varying cell density, marker heterogeneity, and high levels of background staining, as is the case of severely inflamed renal biopsies.

According to the Universal Approximation Theory of neural networks (NN), this class of algorithms has the remarkable ability to model any linear or nonlinear relationship given the appropriate training data and model size (layer width and depth) [148]. NN models such as Cellpose [149] have proven to be powerful tools for the accurate, automatic, and high-throughput analyses of digitized biopsy images [26, 150, 151, 152, 153, 49, 154, 33]. The analysis of cell microscopy images traditionally relies upon the manual segmentation of cells for further downstream quantification. However, this can quickly become intractable, a "simple" task can take hundreds of man-hours and suffers from reader inconsistency [142, 143, 144]. Cellpose [149], Stardist [155], and Deepcell [156] are a few recently developed high-throughput computational methods for cell identification/segmentation. While they are a helpful starting point, these methods have not been benchmarked for use in kidney tissue,

notably heterogeneous and complex to image. While in our prior studies, we relied on Mask R-CNN for instance segmentation (simultaneous detection, segmentation, classification), we have decided to perform cell detection/segmentation separate from cell classification because: 1) having the tasks separated gives us greater flexibility to input better algorithms if needed. 2) creating cell-class-specific ground truth segmentations for a multiclass problem (20+ cell types) is infeasible to acquire. Creating accurate ground truth from 40 channels is difficult for a human, ultimately defeating the advantage of acquiring manual truth. Furthermore, the large amount of training images required for good performance on instance segmentation is intractable.

3.4.1 Prior work of the lab

LN is frequently associated with persistent and severe inflammation, and as a result the high cell densities and high background signal, precise cell segmentation becomes challenging [25, 154, 49]. To address this, deep convolutional neural networks (DCNNs) were used in the automatic cell detection, classification, and segmentation (termed as instance segmentation) on the HR dataset previously mentioned in Chapter 1. The 5-class cell detection was divided into two tasks: instance segmentation for lymphocytes and instance segmentation for DCs. An individual DCNN model, specifically Mask R-CNN, underwent separate training for each task. 246 manually segmented images were used for training, while a validation set comprising 65 manually segmented images was employed for hyperparameter adjustments. A cellular prediction was deemed accurate, or a true positive prediction, if its intersection-over-union (IOU) metric exceeded 0.25 when compared to a verified cell of the identical category; any cellular predictions with a network confidence score below 0.3 were excluded.

To detect cells in the HMP dataset, we had to adopt a modified approach with our Mask R-CNN networks. Two distinct Mask R-CNN models were developed to conduct both single-marker and dual-marker instance segmentation. ROIs derived from the HR dataset were

segmented into 512 × 512 pixel tiles to train each Mask R-CNN model initially. The single-marker Mask R-CNN was created to predict B cells (CD20+) and plasma cells (CD138+), in contrast, the dual-marker Mask R-CNN used for the prediction of single-positive and double-positive T cells. The latter Mask R-CNN was used for detecting CD4+, CD8+, and CD4–CD8– (DN) T cells in LN biopsy tissue. Moreover, the dual-marker Mask R-CNN was further used to determine ICOS and PD1 expression for each predicted T cell within the HMP dataset: cells were either single-positive (CD3+ICOS– or CD3+PD1–) or double-positive (CD3+ICOS+ or CD3+PD1+). The FoxP3 channel was binerized through the thresholding of individual image tiles. T cells with an overlap exceeding 25% of this binary mask were categorized as FoxP3+. Madeleine Durkee (Torcasso) and Rebecca Abraham performed most of this prior work.

3.4.2 Cellpose 2.0 and human-in-the-loop

There is a limit to the utility of human ground truth (GT) due the high variability in human performance, even when done by expert readers [144]. The traditional machine-learning approach of manual GT suffers from dataset feature specificity and requires careful normalization/standardization for future generalizability. Due to the laborious nature of ground truth collection for MMI, we did a qualitative analysis of DAPI segmentation before a quantitative experiment. After conducting a literature review, we decided to use cutting-edge computational methods such as Cellpose [149], Deepcell [157], Startdist [158, 159], and more traditional methods such as multiotsu-thresholding [160]. We made the further decision at the time to use a RAR sample for this qualitative test due to this particular cohort's complex and challenging nature, characterized by high tissue damage and resultant structural ambiguity. These methods were all applied without prior training or tuning (naive models).

As shown on Figure 3.6A, Cellpose qualitatively does DAPI segmentation well for an

off-the-shelf untrained model and it had the most minor issues with DAPI stain artifacts; Deepcell, on the other hand, specifically segmented DAPI background. Finally, "traditional" computer vision methods such as Multiotsu did not generalize well and could not appropriately compensate for DAPI background. As such, we adopted Cellpose 2.0 into our computational pipeline and sought to quantify Cellpose performance in segmenting our tissue samples. To this end, 50 512x512 images from 5 randomly sampled unique biopsies for a total of 250 images were collected from the RA cohort as well as the LN cohort. Using the lower bound IoU threshold of 0.25 (as we do with our prior HR and HMP datasets), the naïve F-1 performance of Cellpose was 0.58 in RAR and 0.81 in LN (Figure 3.6B), and the untrained average precision (AP) was 0.39 and 0.68 respectively (Figure 3.6C); the latter performance was surprisingly high for an untuned model. At this stage we attributed the relatively poor performance of Cellpose in RAR samples to the difficulty of manually segmenting the DAPI signal due to high tissue damage and inflammation.

To improve model performance, we leveraged the Human-in-the-loop (HITL) model retraining approach [161]. HITL AI model retraining refers to an iterative process wherein human experts correct the machine learning model predictions to enhance model performance progressively. This approach is pivotal in refining model predictions and mitigating the propagation of errors through continuous learning and adaptation. Initially, a model is trained with available data, which is then deployed to make predictions or classifications. The model's output is then reviewed and corrected as necessary by domain experts. The corrected output and the original data are then used to retrain the model, enhancing its accuracy and reliability. This cyclical interaction process between human expertise and automated learning facilitates the evolution of more robust and efficient AI models. After this retraining approach is performed, Cellpose DAPI nuclear segmentation achieves a much better F1 performance score of 0.73 in RAR (+.15) and of 0.88 in LN (+.08) at an IoU threshold of 0.25 (Figure 3.6B). The average precision score had similar trends in improve-

ment, with 0.54 in RAR (+.15) and 0.77 (+.09) in LN samples. The latter performance metrics are approaching the upper bounds of ML and human performance/agreement between readers. The lower relative performance of Cellpose in RAR compared to LN was expected since, as stated previously, these biopsy images are full of nuclear ambiguity due to tissue quality differences.

With this impressive predictive performance, we decided to move ahead and utilize the HITL Cellpose model to detect and segment DAPI+ cells in our LN and RAR samples. In doing so, we capture a total of 2.19 million cells, of which 681,674 cells are from the normal kidney samples, 784,113 cells are from the lupus nephritis samples, and 724,960 cells are from renal allograft samples. The average number of cells captured per patient averaged 63,651 cells, 31,520 cells, and 32,818 cells for NK, RA and LN samples, respectively. NK samples on average, have a greater cellularity due to the healthier tissue status and lack of fibrosis or destruction. The cell body was subsequently approximated by performing nuclear dilation with Voronoi tessellation. 512x512 images of DAPI segmentations are then knitted and aligned with the 42 fluorescent channels (Figure 3.6D).

3.5 COMBAT batch correction

In omics studies, such as genomics, transcriptomics, and proteomics, data are frequently collected in batches due to logistical constraints, thereby giving rise to a phenomenon known as batch effects. Batch effects are unintended and systematic variations arising from technical variations and non-biological factors, such as differences in sample preparation, handling, or array processing, which obscure the biological differences and potentially lead to incorrect conclusions. It is paramount to correct these batch effects to ensure the reliability and validity of the analyses and the reproducibility of the results. COMBAT [162] is a widely recognized and extensively used statistical method for the correction of batch effects in high-dimensional data; predominantly employed in the context of genomic studies. COMBAT employs an

Figure 3.6: Cell detection and batch correction

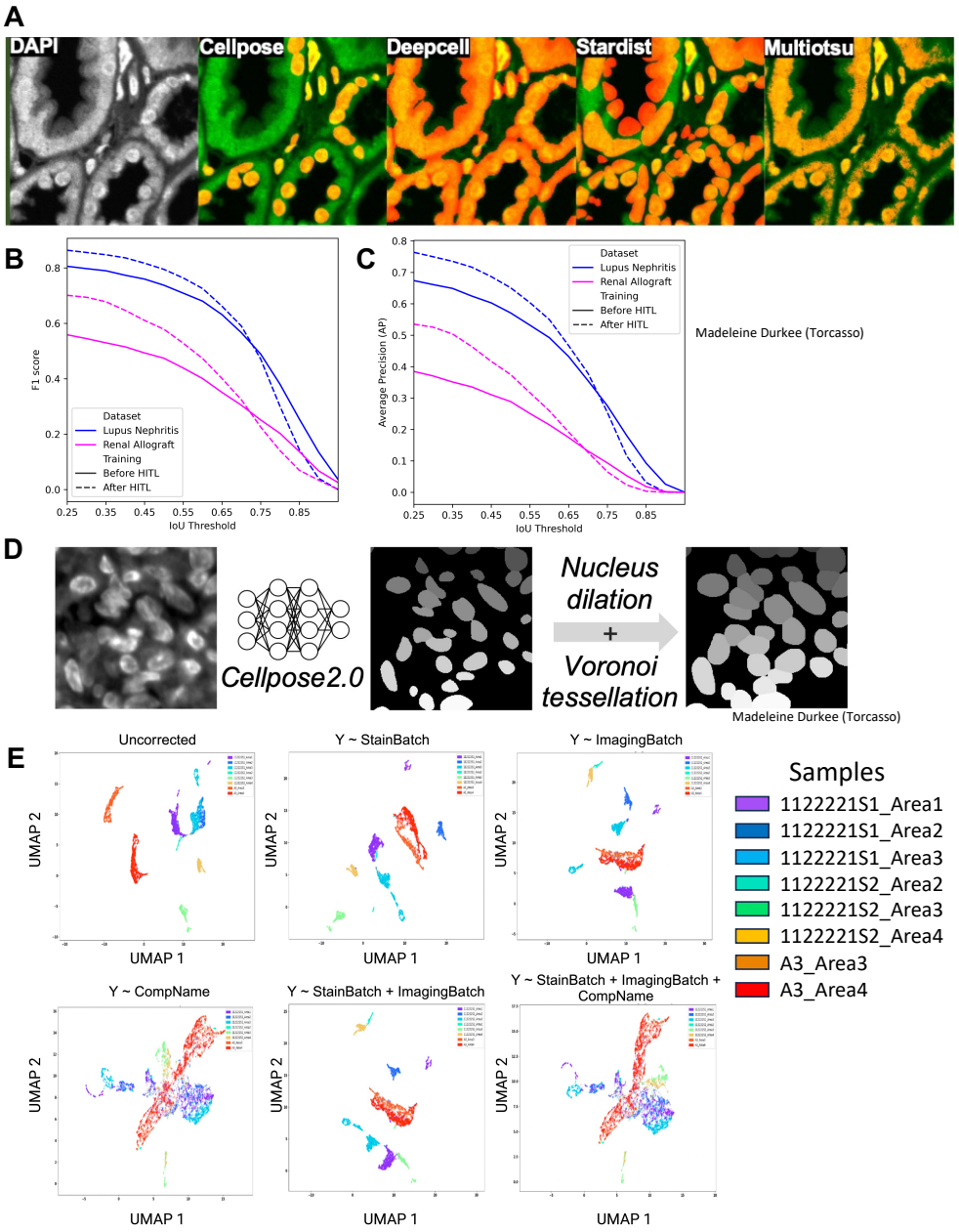

A) Qualitative examples of DAPI signal segmentation by multiple cutting-edge computational methods on a allograft rejection biopsy, imaged on the CODEX system. From the left: Cellpose, Deepcell, Stardist, and Multiotsu. B) Cellpose F1-score performance before human-in-the-loop retraining (solid line) and after HITL retraining (dashed line). Lupus nephritis is shown in blue. Renal allograft rejection is shown in magenta. C) Cellpose average precision performance before human-in-the-loop retraining (solid line) and after HITL retraining (dashed line). D) Workflow diagram of cell detection and segmentation procedure. E) UMAP plot of cellbody MFI COMBAT batch correction using various combinations of technical batch covariates. Y $\sim$ CompName was adopted.

empirical Bayes method to adjust for known and unknown sources of variation. By robustly estimating the parameters of the batch effect, COMBAT can efficiently correct systematic discrepancies between batches, making it possible to discern true biological variances from confounding technical variances. Similarly, we employ COMBAT to correct for potential confounding variables.

Two important sources of batch effects in our dataset are StainBatch, encoding samples that were stained with CODEX microfluidics system, and ImagingBatch, encoding samples that were imaged together. Another variable, CompName, is the unique combination of staining and imaging batch that a particular biopsy belonged to (equivalent to the interaction term StainBatch:ImagingBatch). Using each cell's estimated mean fluorescent intensity (MFI) signal for all markers within the dilated DAPI mask, I tested various combinations of technical covariates that would potentially contribute to batching: 1) Y $\sim$ Stainbatch, 2) Y $\sim$ ImagingBatch, 3) Y $\sim$ CompName, 4) Y $\sim$ StainBatch + ImagingBatch, and 5) Y $\sim$ StainBatch + ImagingBatch + CompName (Figure 3.6E). Batch correction approaches 1,2, and 4 did not sufficiently remove batching effects, as seen on the UMAP plot. However, approaches 3 and 5 appeared better at removing egregious batching effects.

In determining the effectiveness of the COMBAT batch correction method, I focused on the absence of distinct batch-based clustering as a primary indicator of success. Initially, a Uniform Manifold Approximation and Projection (UMAP) visualization of the dataset before batch correction revealed clear separations where cell clusters were primarily aligned with their batch of origin, suggesting batch effects influenced the data's structure. After implementing COMBAT, a subsequent UMAP analysis showed a significant reduction in these batch-aligned separations, indicating a more homogeneous distribution of cell clusters. This observation was critical, as the disappearance of batch-driven clustering in the post-correction UMAP visualization suggested that COMBAT successfully mitigated batch effects, allowing the underlying biological signals to dictate cell grouping. This result val-

idated the use of COMBAT in this context and reinforced the reliability of subsequent analytical interpretations based on these corrected data structures. Since both approaches were deemed ultimately similar, the most straightforward COMBAT correction approach 3 $Y \sim$ CompName was adopted. After correction, we proceed with the cell annotation process using the MFI expression as the core cellular feature for cell-type determination.

CHAPTER 4

CELL CLASSIFICATION AND VALIDATION

For cell classification, the Cellpose 2.0 nuclear segmentation mask of each cell was dilated 7 pixels (1.0549 um) to better approximate the capture of cytoplasmic components of cells. From this cell body mask, many features such as fluorescence intensity, morphology, and texture are exacted and standardized across all channels. While some antibodies were very specific, many of the antibodies displayed varying degrees of cross-reactivity (Figure 4.1A-B). Thus, a simple summation of stain MFIs cannot be used to assign cell class. Therefore, we decided to assign cell class using a flowcytometry-analogous gating approach with a subsample of 25 immunofluorescence markers encompassing well-established protein markers for the differentiation of cell populations with known phenotypes [33, 49, 163, 164]. We design and apply a decision tree that considers the known experimental covariance between marker MFI (i.e. CD3- expression would preclude CD4+ expression), and ultimately assigns cell classes based on an established definition of cell states (Figure 4.2A). These cells have been defined a priori for decades using this method of hierarchical classification (essentially a decision tree using cell MFI). The MFI thresholds used to define marker positivity are calculated using the multiotsu method [160] and manually selected based on cell body positivity thresholds confirmed by manual circling and MFI calculation of positive cells. Prior to any cell class assignment, we performed UMAP dimensionality reduction on 30,000 cells randomly sampled using each segmented cell's MFI using all antibody markers; 10,000 cells are sampled in a balanced manner from our NK, LN, and RAR cohorts (Figure 4.2B-C). When cohort colors are overlayed on the UMAP plot, we found that the majority of cells did not fall in cohort-specific UMAP coordinates, but rather were shared between disease and normal kidney cohorts. Presumably, the bulk of these cells are renal non-immune cells like tubules. However, we can already observe a UMAP cell territory that was clearly enriched in the disease cohorts which are likely immune cells.

Figure 4.1: Average MFI expression of our CODEX marker panel

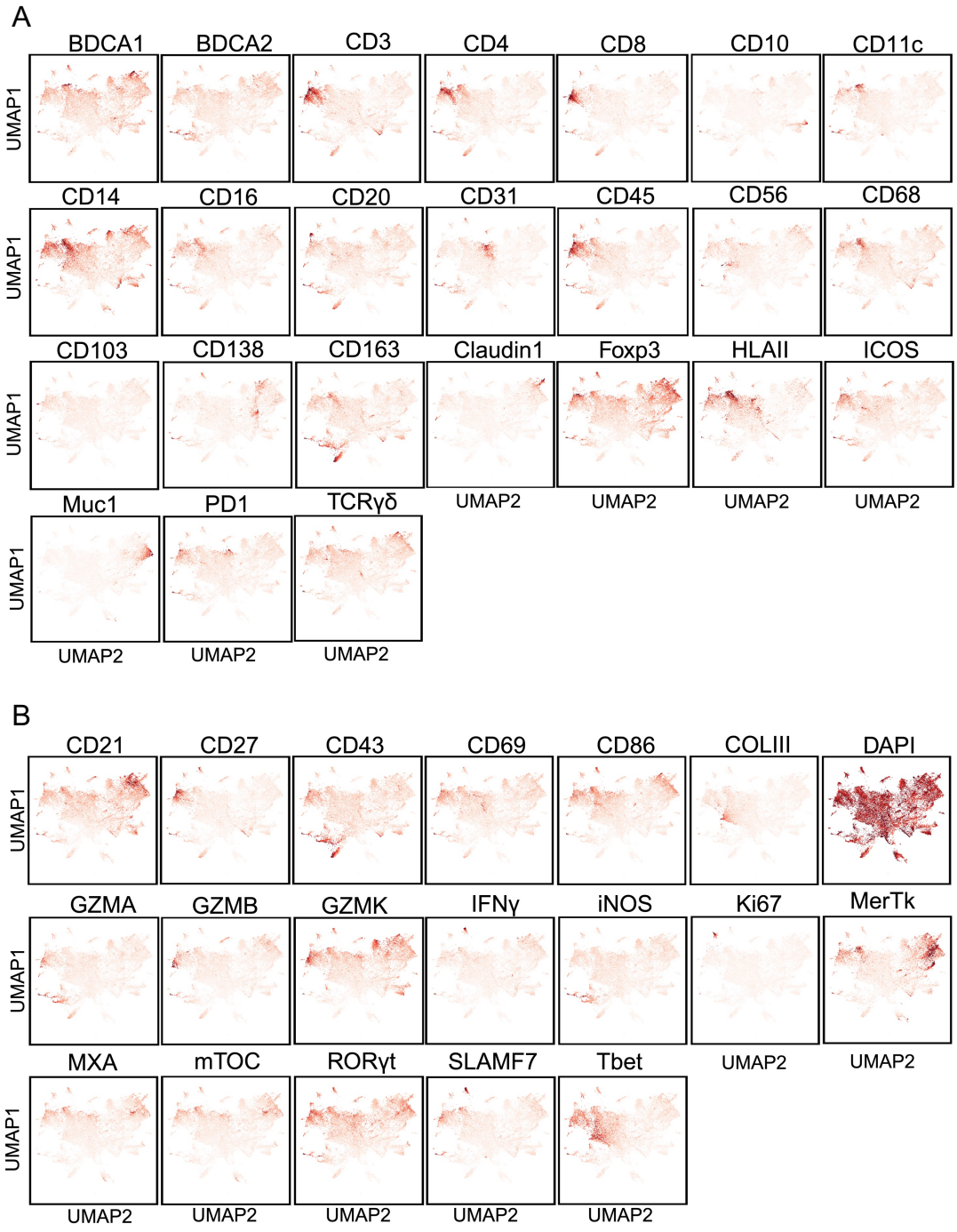

A) UMAP dimensional reduction of cell body MFI from 30,000 cells randomly sampled. 10,000 cells are sampled from each of our three cohorts: normal kidney, lupus nephritis, and renal rllograft. Color indicates MFI for the respective marker; shown are markers used for assigning cell class. B) UMAP dimensional reduction of cell body MFI as described prior. Color indicates MFI for the respective marker; shown are markers not used cell class assignment.

Figure 4.2: Lineage-specific markers and pre-classification UMAP

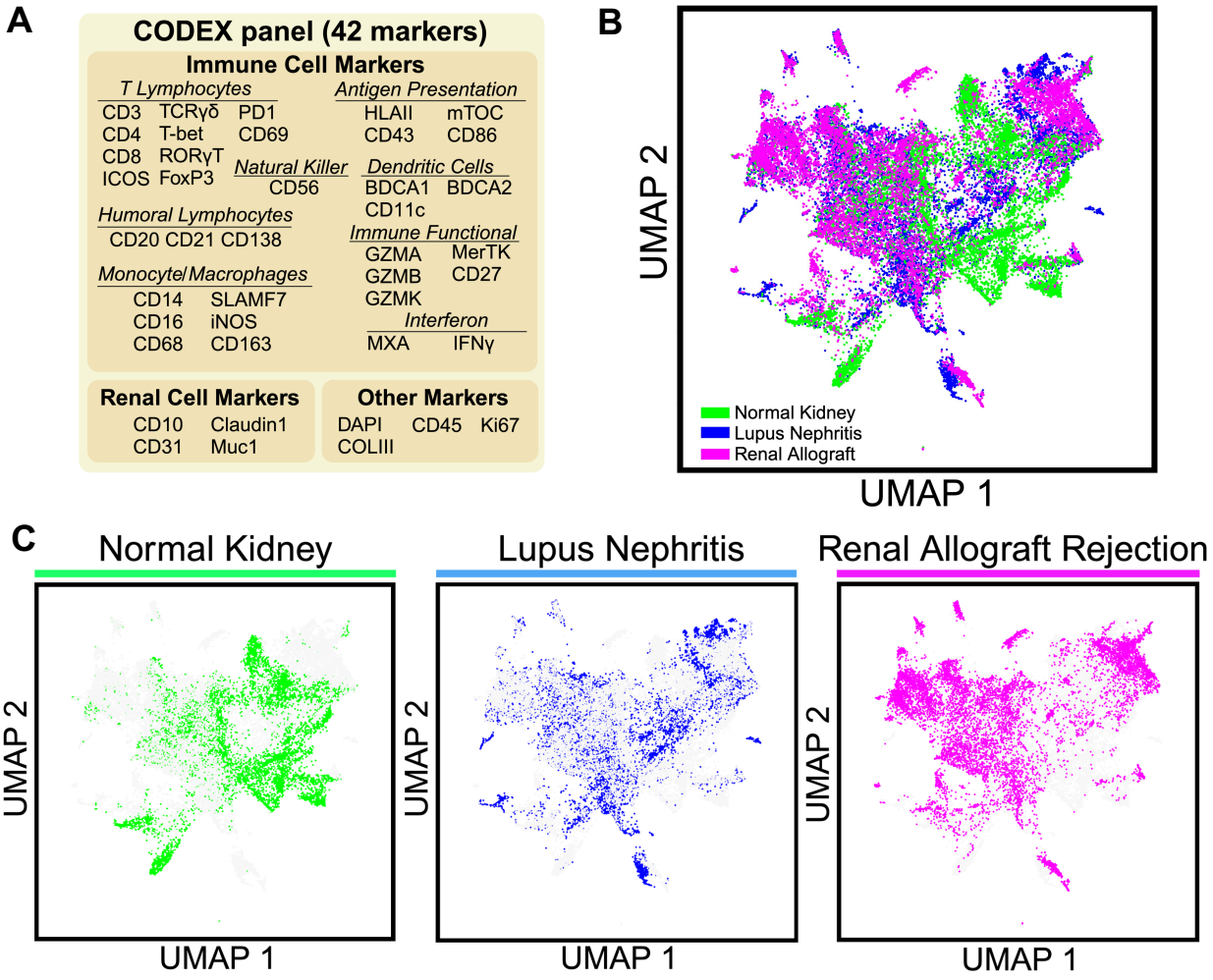

A) CODEX antibody marker panel grouped by cell lineage or cellular activity most associated with that marker. B) UMAP dimensional reduction of cell body MFI from 30,000 cells randomly sampled. 10,000 cells are sampled from each of our three cohorts: normal kidney, lupus nephritis, and renal allograft. Cells are colored according to their cohort of origin: NK, LN, and RAR. C) UMAP dimensional reduction of cell body MFI from 30,000 cells randomly sampled. Cells are colored according to their cohort of origin; showing one cohort at a time: NK, LN, and RAR.

4.1 Cell gating

4.1.1 Decision tree algorithm: renal immune cells

Since CD45 is widely recognized as a pan-immune marker, it was used as the first logical gate (decision tree branch), for binning cells into either mutually exclusive immune or non-immune lineages. Multiotsu thresholding was used to define cell marker positivity due to its desired statistical properties. In flow-cytometry, the threshold for immune marker positivity is qualitatively determined by visually/manually circling to select for prominent population densities, colloquially called 'gating'. Similarly to select for prominent cell populations, multiotsu method was chosen due to its maximization of intergroup variance and the minimalization of intragroup variance allowing for greater; desired biological as well as statistical behavior. The number of Otsu classes used, as well as the specific threshold ultimately used for marker positivity, was chosen in conjunction with manual checks of CODEX images by Junting Ai and myself. For example, a handful of CD45+CD3+CD4-CD8+ T cells were manually circled, and the cell's corresponding MFI for CD8 was calculated; the Otsu threshold that most closely matched this spot check was chosen. In this process, we noticed that myeloid cells have lower levels of CD45 expression in comparison to T and B lymphocytes. As such, to avoid the loss of myeloid cells due to the CD45+ positivity gate we repeated the myeloid gating scheme (described later) prior to gating for the non-immune renal markers (Figure 4.2A-B).

For the second logic gating branch, we focused on the two remaining pan-immune cell markers: HLAII and CD3. HLAII expression is universal among antigen-presenting cells such as myeloid cell lineages and humoral cell lineages. Conversely, CD3 is expressed by all T-cells as part of the TCR complex discussed in prior background. We can further leverage the fact that CD3 is also known to not be normally expressed by myeloid cells and humoral cells. CD3+HLAII+ double expression is expected in activated T-lymphocytes

that have internalized HLAII complexes (or are currently interacting with an HLAII+ cell). We leveraged this known biology to create the HLAII/CD3 logic branch for T-cell and myeloid/humoral cell binning. For those cells that are CD3+(HLAII), we apply the further canonical TCR co-receptors CD4/CD8 for differentiating between the main T-lymphocyte lineages: Thelper cells (CD4+) and cytotoxic T cells (CD8+).

In doing so, we observe the traditional "bird/butterfly" plot that is commonly seen with these T-cell populations in flowcytometry (Figure 4.2D). The CD4+CD8+ T-cell population is normally only seen as either part of the normal developmental process of thymocytes whereby the CD4+CD8+ co-expression is an intermediate stage, where TCRα rearrangement and maturation eventually leads to T-cells expressing a single co-receptor [165]. However, CD4+CD8+ T-cells have frequently been reported in human diseases such as cancer and autoimmunity [166]. In our case, we observed two phenomena in this CD4+CD8+ T-cell population: 1) The streak of cells that is "abnormal" are red blood cells (these cells have high cross-reactivity for most markers we use). We are able to "gate" this population out CD10/MUC1 positivity which does not occur in true T-cells. 2) True CD4+CD8+CD10-MUC1- T-cells do exist, the majority of which are actually CD4+ T-cel:CD8+ T-cell doublets. CD3+ CD4-CD8- double negatives are later combined with CD56/TCR$\gamma\delta$ gating to identify the $\gamma\delta$ T-cell and Natural Killer T cell-subtypes.

CD45+CD3-HLAII+ cells, APCs encompassing most myeloid cell lineages and humoral cells, are the second major decision tree branch at this level. CD14 and CD16 positivity were chosen as the next logical branches since these are the canonical macrophage markers for the major macrophage populations CD14+CD16- Mϕ, CD14-CD16+ Mϕ, and CD14+CD16+ Mϕ. Those cells that were CD14-CD16- were then passed unto CD20/CD138 positivity gating to capture CD45+HLAII+(CD20)CD138+ plasmablasts and HLAII+CD20+CD138- B-cells. The remaining CD45+HLAII+CD20-CD138- cells are then passed through BDCA and CD103, and BDCA1 and CD11c gating to capture the last APC cell populations: conven-

tional dendritic cells (cDC1/cDC2) and plasmacytoid dendritic cells (pDCs). CD45+CD3-HLAII- cells similarly underwent CD14/CD16 positivity gating to classify CD45+CD3-HLAII-CD14-CD16+ Neutrophils, and CD45+CD3-HLAII-CD14+(CD16) HLAII- monocytes. Those cells that were CD45+CD3-HLAII-CD14-CD16- underwent a final CD56 and CD138 gating step to identify CD45+CD3-HLAII-CD14-CD16-CD56+CD138- Natural Killer cells and CD45+CD3-HLAII-CD14-CD16-CD56+(CD138) plasma cells.

4.1.2 Decision tree algorithm: renal non-immune cells and second order cell classes

As previously mentioned, since CD45 levels in myeloid lineages were observed to be much lower than CD45 expression in lymphoid cells, we were worried that the Otsu threshold calculated across all cells would be biased towards capturing lymphocytes but not myeloid cells. As such, we decided that CD45- cells would also undergo an initial CD3/HLAII logic gating (Figure 4.3B). CD45-HLAII+ cells were shunted to the classical CD14/CD16 markers to capture CD45-HLAII+CD14+CD16- Mϕ and CD45-HLAII+CD14-CD16+ Mϕ. CD45-HLAII- cells also underwent the CD14/CD16 gating branch to classify CD45-HLAII-CD14+(CD16) HLAII- Monocytes. Finally, the remaining CD45-CD3-HLAII-CD14-CD16- and CD45-CD3-HLAII+CD14-CD16- cells were allowed to proceed with the renal cell markers. CD10 and MUC1 are the first set of renal markers that we apply to capture CD10-MUC1+ distal collecting tubules and CD10+(MUC1) proximal tubules. CD10-MUC1- renal cells were sequentially shunted to the CD31 and Claudin1 gates to classify CD10-MUC1-CD31+ endothelial cells and CD10-MUC1-Claudin1+ inflamed "stressed" tubules as seen in prior Figure 3.2,3.4. Renal cells that are DAPI+CD45-CD10-MUC1-CD31-Claudin1- were left unlabeled; this population of cells is presumably tubular cells whose DAPI mask dilation has insufficiently captured the membranous expression of renal non-immune markers

After cells are assigned a primary immune or non-immune cell class as above, we perform

further positivity gating for 2nd order functional phenotypes of particular immunological importance. For example, the main macrophage population in these samples CD14+ Mϕ, is further classified into M1 (MerTk+) and M2 (CD163+) cell populations (Figure 4.3C). CD14+CD163+MerTk+ cells are left as a distinct functional macrophage subpopulation, and CD14+CD163-MerTk- Mϕ were left as the conventional CD14+CD16- Mϕ phenotype. Similarly, ICOS/PD1/FOXP3 positivity is used to further functionally subclassify CD4+ T-cells into CD4+ICOS+ T-cells, CD4+PD1+ T-cells, CD4+PD1+ICOS+ Tfollicular cells, and CD4+PD1-ICOS-Foxp3+ regulatory T-cells. CD8+ T-cells, likewise, are also subclassified as CD8+ICOS+ T-cells, CD8+PD1+ T-cells, CD8+PD1+ICOS+ T-cells, and CD8+PD1-ICOS-Foxp3+ regulatory T-cells. Moreover, a final CD68 marker gate is applied to HLAII+ monocytes and HLAII- monocytes to classify CD68+ Monocyte-derived macrophages.

4.2 Cell class assignment marker expression validation

4.2.1 Leave-one-out Z-score

I use our MFI cell gating method to assign 35 cell classes, of which five are non-immune, and the remaining are immune. Figure 4.4A shows a summary table of these cells and the respective overall gating applied, grouped by the major cell lineages. As a quality check that our classified cells express their respective canonical markers, we look at the leave-one-out Z-score of MFI expression for all classified cells (Figure 4.4B). We calculate the Z-score using each cell's mean fluorescent intensity (MFI) within the cell body mask segmentation, the MFI expression of all cells of the current class of reference is then compared to the MFI expression of all the other cell classes together. As expected, our assigned cell classes broadly align with the Z-score for the desired class-specific protein expression, as in Figure 4.4A. For example, CD4+ T cells express high levels of CD45, CD3, CD4 as desired with log2 Z-score > 4 for those respective markers, much higher than the other cell populations. This heatmap plot

Figure 4.3: Decision tree algorithm for cell class assignment

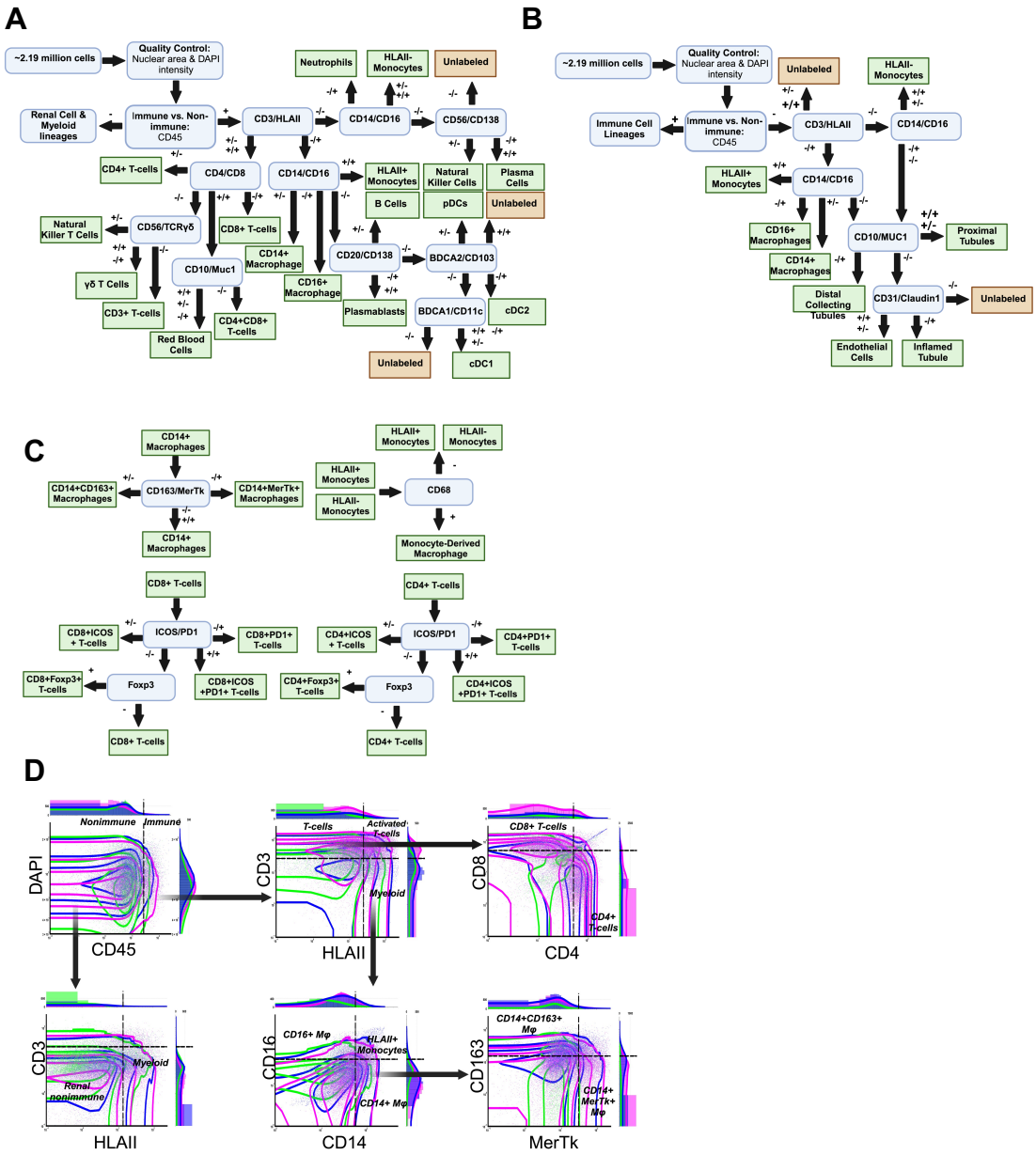

A) flow-cytometry analogous decision tree gating algorithm for immune cell classification based on cell body MFI. B) flow-cytometry analogous decision tree gating algorithm for non-immune cell and myeloid cell (CD45 low) classification based on cell body MFI. C) Decision tree gating algorithm for CD14+ Macrophages for CD163+ and MerTk marker positivity (top left). Algorithm for CD8+ T-cells for ICOS, PD-1 and marker positivity (bottom left). Algorithm for monocyte-derived macrophages using CD68 marker positivity (top right). Algorithm for CD4+ T-cells for ICOS, PD-1 and marker positivity (bottom right). D) Gating plots showing cell body MFI for the markers used for cell classification colored by cohort normal kidney (green), lupus nephritis (blue), renal allograft (magenta). Dotted line shows the gating threshold as determined using the multiostu method. A representative sample of 30,000 cells; 10,000 from each cohort is shown.

Figure 4.4: Cell classification of Cellpose 2.0 segmented cells

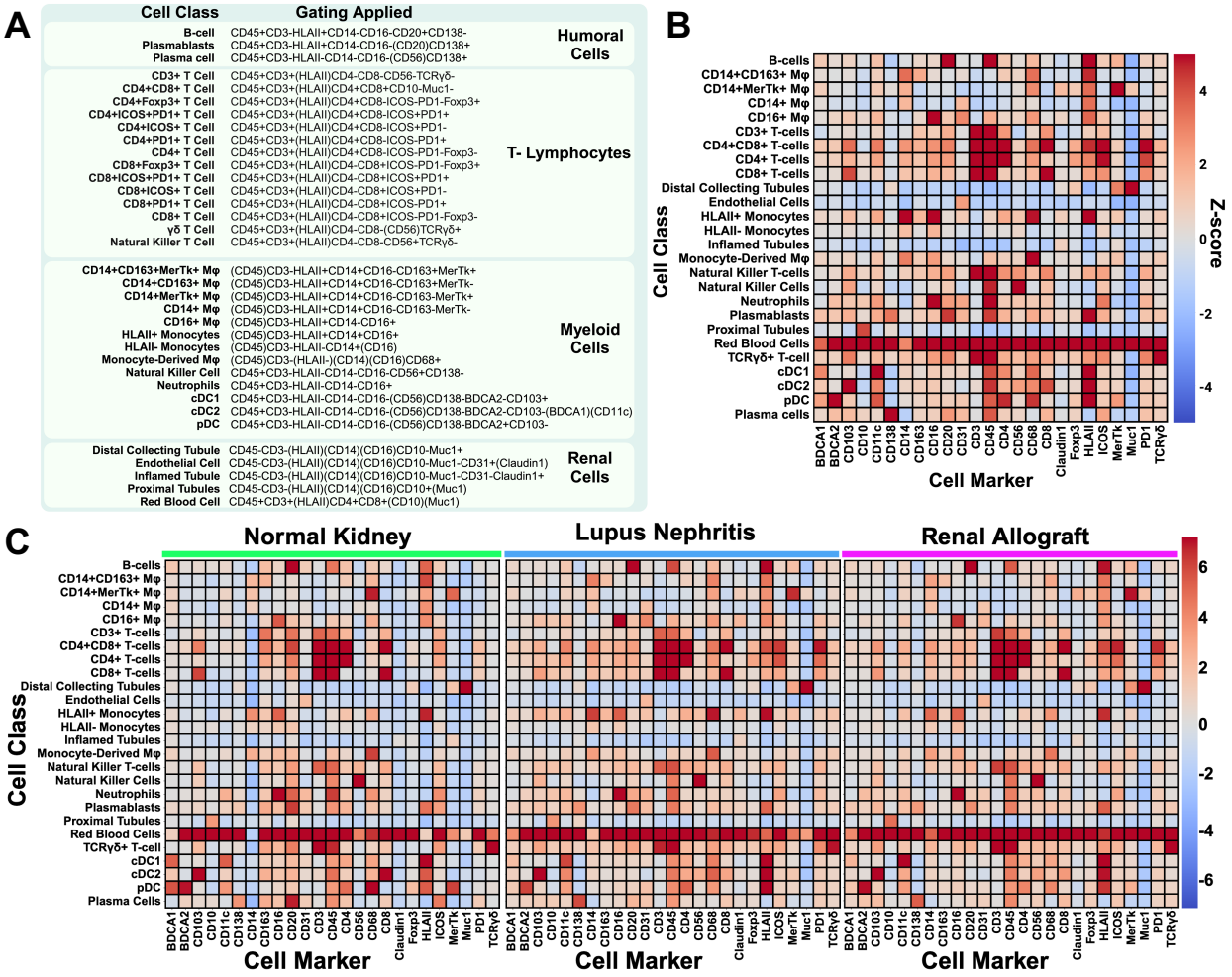

A) Summary table of the 30 immune and 5 non-immune cell classes ultimately assigned using the decision tree algorithm; cells are grouped by lineage. B) Heatmap of the leave-one-out Z score (current cell class vs. all others) of the cell body MFI for the cell markers used in cell class assignment for the main immune and non-immune cell classes. C) Heatmap of the cohort leave-one-out Z score (current cell class vs. all others) of the cell body MFI for the cell markers used in cell class assignment. Heatmaps for normal kidney (left), lupus nephritis (middle), and renal allograft (right).

further helps us identify any residual marker expression or any other potentially interesting expression patterns that were not explicitly considered. However, with these data, we are not worried about any residual marker expression or missing any cell classes of interest for our assigned cell classes.

We further generate cohort-specific leave-one-out Z-score plots to validate if the canonical MFI expression is consistent across our clinical cohorts (Supplemental Figure 3C). These plots again show that our assigned cell classes broadly align with the desired class-specific protein expression irrespective of cohort of origin. This indicates that cell definitions are consistent across cohorts for statistical comparisons. This allows us to perform comparative analyses without worrying about improper class assignment/sampling. Furthermore, we observe no obvious marker bias in the "Unassigned" category, across all 3 cohorts. This makes us confident that we are not missing essential populations or underutilizing any markers. These cohort-specific plots are a vital quality control step for cell class assignment. Otherwise, if these plots do not agree, that is a sign of either noisy/poor data or cell classification being amiss.

CHAPTER 5

DISTINCT IMMUNE TRAJECTORIES

5.0.1 UMAP plots

To explore cohort-specific cell populations we generated further UMAP plots by sampling 10,000 cells from NK, LN, and RAR cohorts. UMAP dimensionality reduction was performed on the calculated cellbody MFI (captured through DAPI mask dilation) as previously stated in Chapter 4. When overlaying the assigned cell classes, we see that cells segregate according to their lineage similarities with a clear immune-nonimmune axis and a lymphoid-myeloid axis (Figure 5.1A). When we plot each cohort separately but preserving the joint UMAP embeddings, we can see apparent population differences among our cohorts with the under-representation of immune cells in the NK cohort, as well as an enrichment of the T-lymphoid compartment in RAR samples and the enrichment of the myeloid lineages in LN; suggesting a disease-specific immune lineage polarization. The shared overlap of NK with LN and RA cells in the non-immune cell territory is expected since all these samples are renal biopsy tissue. The lack of NK cells in the immune cell territory is a crucial quality control milestone, as these are the negative controls. The greater amount of T lymphocytes in RA and the greater amount of myeloid cells in LN is expected, and prior data confirms this. When we look back at each cell's MFI using the exact UMAP embeddings in Figure 4.1, we can see how the fluorescent marker expression broadly aligns with the assigned cell classes and gating approach. For example, the T-lymphoid axis is enriched for the expected lineage markers CD3/CD4/CD8, and the myeloid-axis is enriched for HLAII/CD14/CD16, confirming cell class assignment aligns with the desired marker expression in UMAP space as well.

Figure 5.1: Visualization of assigned immune and non-immune cell classes

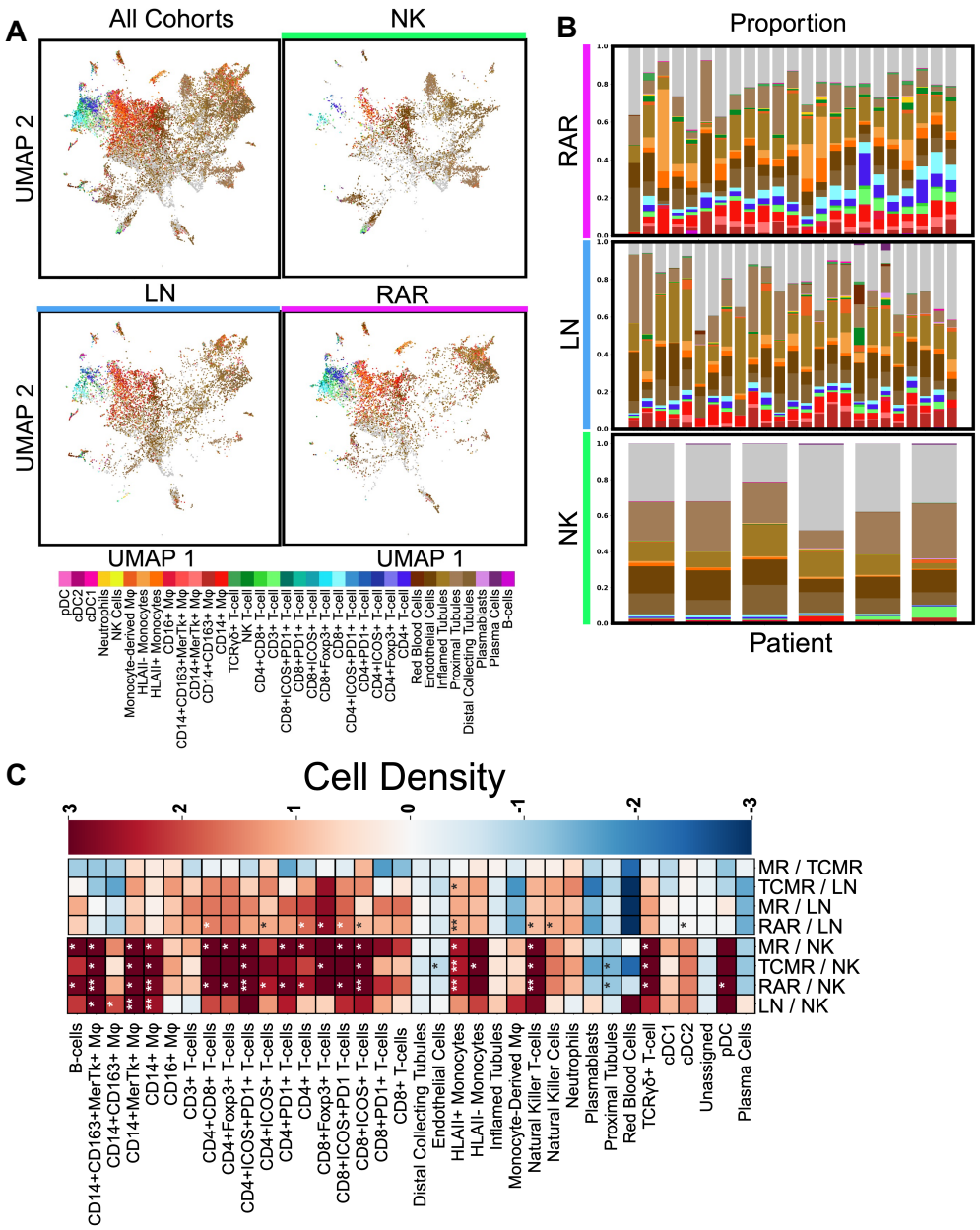

A) UMAP dimensional reduction of cell body MFI from 30,000 cells randomly sampled. 10,000 cells are sampled from each of our three cohorts: normal kidney, lupus nephritis, and renal allograft. Cells colored according to their cell class identity; 35 total classes are shown. B) Patient-level proportions of the 30 immune and 5 non-immune cell classes by cohort. normal kidney (bottom), lupus nephritis (middle), and renal allograft (top). C) non-parametric Mann-Whitney-U difference of the mean test for population differences in classified cell density between patient cohorts; from the bottom row : LN-NK, RA-NK, TCMR-NK, MR-NK, LN-RA, LN-MR, LN-TCMR, and MR-TCMR. Color indicates log2 fold change. Benjamini-Hochberg p-value correction is performed. * $p < 0.05$, ** $p < 0.01$, *** $p < 0.001$.

5.1 Differential presence of immune cell populations

5.1.1 Cell count data

Next, we sought to quantify the observed immune T-cell:Myeloid cell polarity on the UMAP plots by looking at classified cell frequency data. When doing so, we note that the "undefined" cell class is the dominant cell class at 38.8% (250,987 cells) in NK, 24.0% (188,199 cells) in LN, and 22.0% (159,622 cells) in RAR respectively (Figure 5.2A). This undefined cell class likely represents mostly tubular cells as the marker used to categorize these cells, CD10/MUC1/Claudin1, is primarily expressed at the cell surface and is not fully captured by nuclear dilation of these large cells. In NK, non-immune cells dominate with proximal tubules (136,016 cells; 19.9%), endothelial cells (79,185 cells; 11.6%), inflamed tubules (77,049 cells, 11.6%), and distal collecting tubules (72,926 cells; 10.6%) representing the bulk (53.7%) of cells classified. Similarly, non-immune renal cells were the dominant cell classes in LN and RAR, albeit at lower numbers. However, in both LN and RAR, inflamed CD10-MUC1-Claudin1+ tubules were the top assigned class representing 17.6% (138,193 cells) and 13.2% (96,113 cells) of cells respectively. In LN, proximal tubules (109,330 cells; 13.9%), endothelial cells (87,288; 11.1%), and distal collecting tubules (66,103 cells; 8.4%) were the following most frequent cell classes. In RAR, proximal tubules (63,629 cells; 8.7%), distal collecting tubules (62,211 cells; 8.5%), and endothelial cells (8.3%) were the most abundant renal cell classes. Non-immune cells ultimately constitute a total of 51.0% of cells in LN and 38.7% of cells in RAR in comparison to 53.7% of all cells in NK.

When we consider the immune cell lineages we find that, as expected, NK has a much lower frequency of immune infiltrate across all cell lineages. The main immune cell populations captured in this control cohort are CD3+ T-cells (11,604 cells; 1.7%), CD14+ Mϕs (9,058 cells; 1.3%) and CD14+CD163+ M2 Mϕs (7,076 cells; 1.0%). In LN samples, while non-immune cells are also the most frequent cell population, immune cell frequencies

were much higher, especially for myeloid cells like CD14+ Mϕs (34,871 cells; 4.4%) and CD14+CD163+ Mϕs (32,581 cells; 4.1%). Similarly, in RAR, renal non-immune cells are amongst the most frequent; however, we see a larger percentage of myeloid and T-cells relative to NK. For example, the myeloid CD14+ Mϕs (41,138 cells; 5.6%), CD14+CD163+ Mϕs (18,813 cells; 2.5%), and CD14+CD163+ Mϕs (17,802 cells; 2.4%). In regards to T-cells in RAR samples, we see elevated frequencies of CD3+ T-cells (22,253 cells; 3.0%), CD4+ T-cells (16,551 cells; 2.2%), and CD8+ T-cells (14,151 cells; 1.9%). These aforementioned cell trends are further evident when looking at the per-biopsy proportion of cell classes, both with all cell classes included (Figure 5.1B) and only immune cell classes included (Figure 5.2 C). In doing so, we observe great heterogeneity in the immune infiltrate across all patients, irrespective of the cohort. However, we again see an expansion of the myeloid compartment with relatively minor T-lymphocyte presence in LN, while in RAR we see a greater expansion of the T-lymphocyte population relative to the myeloid cell compartment. While the NK cohort in general has less immune infiltrate, we see a greater relative proportion of CD3+ CD4-CD8-CD56-TCR$\gamma\delta$ T-cells.

5.1.2 Density analysis

We find that the total cell counts captured per patient vary vastly across all three of our cohorts (Figure 5.2B). However, when we normalize by the area of capture (in mm^2) to retrieve cell density, we see that this between-patient variance is reduced; cell frequency data trend changes when we normalize by area (density). In this CODEX dataset, $1mm^2$ is equivalent to 44,032,515 pixels at a pixel size of 0.1507 microns. While we observe some heterogeneity in cell count density within each cohort group, we find no overall differences in this variance. The simple normalization step of dividing cell frequency data by the area of imaged tissue is presumed to correct for some sources of technical variance. This is crucial to prevent potential sampling bias due to greater tissue capture that may occur due to

Figure 5.2: Cell class frequency data and heterogeneity

A

Normal Kidney

Cell Class	Total Count	% of Total
Undefined	250987	36.819
Proximal Tubules	136016	19.953
Endothelial Cells	79185	11.616
Inflamed Tubules	77049	11.303
Distal Collecting Tubules	72926	10.698
CD3+ T-cells	11604	1.702
CD14+ Mφ	9058	1.329
CD14+ CD163+ Mφ	7076	1.038
HLAII- Monocytes	4911	0.720
HLAII+ Monocytes	4437	0.651
CD8+ T Cells	3817	0.560
Monocyte-Derived Mφ	3418	0.501
Neutrophils	3094	0.454
Plasma Cells	3033	0.445
CD16+ Mφ	2927	0.429
CD4+ T-cells	2576	0.378
Plasmablasts	1906	0.280
Natural Killer T-cells	950	0.139
CD4+ ICOS+ T-cells	818	0.120
TCRγδ T-Cells	682	0.100
CD8+ Foxp3+ T-cells	672	0.099
CD8+ PD1+ T-cells	654	0.096
cDC1s	587	0.086
CD14+ MERTK+ Mφ	392	0.058
CD4+ CD8+ T-cells	372	0.055
B-cells	310	0.045
CD4+ PD1+ T-cells	309	0.045
CD8+ ICOS+ T-cells	302	0.044
Red Blood Cells	299	0.044
Natural Killer Cells	294	0.043
CD8+ ICOS+ PD1+ T-cells	269	0.039
CD14+ CD163+ MERTK+ Mφ	254	0.037
CD4+ ICOS+ PD1+ T-cells	223	0.033
CD4+ Foxp3+ T-cells	218	0.032
cDC2s	29	0.004
pDCs	20	0.003
Total	681674	100.000

Lupus Nephritis

Cell Class	Total Count	% of Total
Undefined	188199	24.001
Inflamed Tubules	138193	17.624
Proximal Tubules	109330	13.943
Endothelial Cells	87288	11.132
Distal Collecting Tubules	66103	8.430
CD14+ Mφ	34871	4.447
CD14+ CD163+ Mφ	32581	4.155
HLAII- Monocytes	16918	2.158
HLAII+ Monocytes	15377	1.961
Monocyte-Derived Mφ	13695	1.747
CD3+ T-cells	9958	1.270
CD14+ CD163+ MERTK+ Mφ	9519	1.214
CD14+ MERTK+ Mφ	8800	1.122
CD8+ T-cells	6777	0.864
CD4+ T-cells	5804	0.740
Natural Killer T-cells	4851	0.619
CD4+ ICOS+ PD1+ T-cells	3552	0.453
TCRγδ T-cells	3086	0.394
CD16+ Mφ	3069	0.391
CD4+ ICOS+ T-cells	2825	0.360
Red Blood Cells	2672	0.341
Plasma Cells	2297	0.293
Plasmablasts	2017	0.257
B-cells	1944	0.248
CD4+ PD1+ T-cells	1815	0.231
Neutrophils	1754	0.224
CD8+ ICOS+ T-cells	1637	0.209
CD8+ PD1+ T-cells	1621	0.207
CD8+ ICOS+ PD1+ T-cells	1589	0.203
CD4+ CD8+ T-cells	1489	0.190
cDC1s	1330	0.170
CD8+ Foxp3+ T-cells	1266	0.161
CD4+ Foxp3+ T-cells	1001	0.128
pDCs	515	0.066
Natural Killer Cells	293	0.037
cDC2s	97	0.012
Total	784133	100.000

Renal Allograft

Cell Class	Total Count	% of Total
Undefined	159622	22.018
Inflamed Tubules	96113	13.258
Proximal Tubules	63629	8.777
Distal Collecting Tubules	62211	8.581
Endothelial Cells	60877	8.397
CD14+ Mφ	41138	5.675
HLAII- Monocytes	30435	4.198
HLAII+ Monocytes	29348	4.048
CD3+ T-cells	22253	3.070
CD14+ CD163+ Mφ	18813	2.595
CD14+ MERTK+ Mφ	17802	2.456
CD4+ T-cells	16551	2.283
CD8+ T-cells	14151	1.952
Natural Killer T-cells	11475	1.583
CD8+ Foxp3+ T-cells	7963	1.098
CD8+ ICOS+ PD1+ T-cells	7954	1.097
TCRγδ T-cells	6804	0.939
CD16+ Mφ	6310	0.870
CD14+ CD163+ MERTK+ Mφ	6291	0.868
CD4+ ICOS+ T-cells	6237	0.860
Monocyte-Derived Mφ	4962	0.684
CD4+ CD8+ T-cells	4948	0.683
CD4+ PD1+ T-cells	4491	0.619
CD8+ ICOS+ PD1+ T-cells	4447	0.613
B-cells	3774	0.521
CD8+ PD1+ T-cells	3456	0.477
CD8+ ICOS+ T-cells	3391	0.468
Neutrophils	2864	0.395
CD4+ Foxp3+ T-cells	2587	0.357
cDC1s	1151	0.159
Plasma Cells	971	0.134
Plasmablasts	644	0.089
Natural Killer Cells	611	0.084
pDCs	365	0.050
Red Blood Cells	222	0.031
cDC2s	99	0.014
Total	724960	100.000

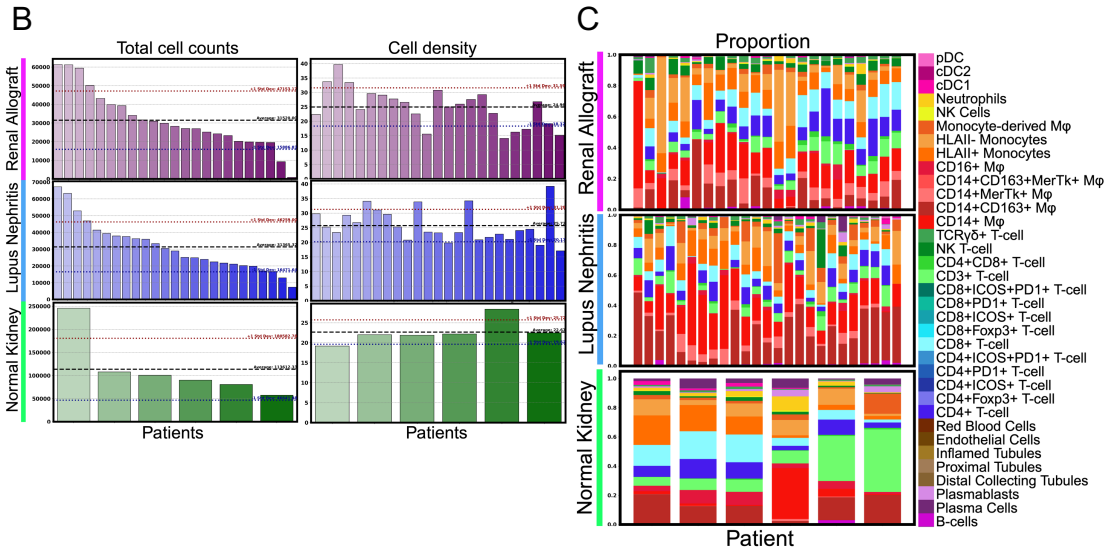

A) Summary table of cell class total count and total proportion by disease cohort. Normal kidney (left), lupus nephritis (middle), and renal allograft (right). B) Patient-level total cell counts and total cell densities by cohort. Normal kidney (bottom), lupus nephritis (middle), and renal allograft (top). C) Patient-level proportions of only the 30 immune cell classes by cohort. Normal kidney (bottom), lupus nephritis (middle), and renal allograft (top).

technical/logistical factors; which traditional methods like RNAseq are unable to account for as effectively as using the literal image of the tissue area. For example, the most abundant NK sample had ∼248,000 cells in total, while the most abundant LN and RAR samples contained ∼61,000 cells and $\tilde{6}$7,000 cells, respectively. However, those same samples once normalized by area have ∼18.1 cells/mm^2, ∼24.9 cells/mm^2 and ∼23.2 cells/mm^2. This discrepancy reflects the technical/clinical nature of these samples. The NK biopsies are negative nephrectomy resections as previously mentioned, and as such, are physically much larger than the LN and RAR core needle biopsies. However, LN and RAR have higher cellularity than NK presumably due to the presence of immune cell infiltrate (inflammation by definition). This is visually evident in Figure 3.2 and Figure 3.3 from Chapter 3. Furthermore, Figure 5.2B is an essential plot for advocating for the benefit of spatial methods, or at least in the necessity of normalizing by tissue area when analyzing such cell data.

To statistically test our cohorts for the differential presence of particular cell classes, we perform a non-parametric Mann-Whitney-U (MWU) test for population differences using cell densities [167]. We perform the following comparisons: LN-NK, RA-NK, TCMR-NK, MR-NK, LN-RA, LN-MR, LN-TCMR, and MR-TCMR. Benjamini-Hochberg p-value correction is performed to control for multiple p-value hypothesis testing. The Mann-Whitney-U is commonly used when the assumptions for the independent t-test are not satisfied, mainly when the population is not normally distributed. The test involves ranking all the observations from both groups together, then summing the ranks for each group and calculating the U statistic for both. I prefer this test to avoid imposing the assumptions of independence or normality required for T and Z tests.

Comparing disease cohorts, we observed a significant enrichment of myeloid and T-cell lineages comparing LN and RAR to the NK control (Figure 5.1C). In LN samples, we find that CD14+CD163+MerTk+ Mϕ ($p < 0.05$), CD14+CD163+ Mϕ ($p < 0.05$), CD14+MerTk+ Mϕ ($p < 0.01$), HLAII+ Monocytes ($p < 0.01$), and CD14+ Mϕ ($p < 0.01$) cells have higher

densities in renal tissue in comparison to NK. Similarly, in RAR we find statistically significant increases in the density of CD14+CD163+MerTk+ Mϕ ($p < 0.01$), CD14+MerTk+ Mϕ ($p < 0.05$), CD14+MerTk+ Mϕ ($p < 0.01$), and HLAII+ Monocytes ($p < 0.01$) Interestingly, only the LN cohort had a significant increase in the density of CD14+CD163+ Mϕ. While we see a generalized increase in the density of T-cells in LN compared to NK, none of these differences are statistically significant, potentially due to the high heterogeneity within this cohort. On the other hand, in RAR and in the respective TCMR and MR subtypes we do find statistical significance in the comparison to the NK control. In RAR, CD4+ICOS+PD1+ T-cells ($p < 0.1$), CD8+ICOS+ T-cells ($p < 0.1$), and Natural Killer T-cells ($p < 0.1$) had the greatest statistical significance. This is followed by CD4+CD8+ T-cells ($p < 0.05$), CD4+FoxP3+ T-cells ($p < 0.05$), CD4+ICOS+ T-cells ($p < 0.05$), CD4+PD1+ T-cells ($p < 0.05$), CD4+ T-cells ($p < 0.05$), and TCR$\gamma\delta$ T-cells ($p < 0.05$). When comparing between disease states, we observe a significant enrichment of various T-cell lineages, as well as in HLAII+ monocytes ($p < 0.01$) in RAR when compared to LN. (Figure 2C). For example, CD4+CD8+ T-cells ($p < 0.05$), CD4+ICOS+ T-cells ($p < 0.05$), CD4+ T-cells ($p < 0.05$), CD8+Foxp3+ T-cells ($p < 0.05$), CD8+ICOS+PD1+ T-cells, CD8+ICOS+ T-cells ($p < 0.05$), and natural killer T-cells ($p < 0.05$) all display statistically significant increases in RAR tissue.

Other statistically significant differences to highlight are higher levels of pDCs in RAR ($p < 0.05$) when compared to the NK control, although upregulation of this population is seen in all disease cohorts. While not statistically significant, we observe higher densities of B-cells, plasma cells, and plasmablasts in LN tissue compared to the NK control, in line with expectation[97, 49]. Furthermore, in both RAR-NK and TCMR-NK comparisons, we note a statistically significant decrease in proximal tubules ($p < 0.05$ and $p < 0.05$) and endothelial cells in TCMR-NK ($p < 0.05$). We postulate that this difference in non-immune renal cells may be due to a bias in tissue sampling. As previously mentioned in Chapter 3,

the clinical context of these biopsies is vastly different. A nephrectomy (the NK control), in theory, would have a greater variance in the sourcing of renal tissue since the biopsy is not diagnostic in nature but rather a surgical resection of tissue. LN and RAR in contrast, are diagnostic core needle biopsies taken interventionally and not surgically. Furthermore, the pattern of renal CD10 and MUC1 staining on the representative biopsy images in Figure 3.3 is vastly different between LN/RAR and NK.

In all, these statistical comparisons are essential for us to better understand the inherent differences between alloimmunity in RAR and autoimmunity in LN on a "global' level. In prior chapters, we previously saw qualitative signs of a generalized increase of T-lymphocytes in RA and myeloid cells in LN. However, here we get statistical confirmation of these trends using a MWU test. I consider the statistically significant increase in T-cells in RAR to be an important quality/sanity check for this study, since by definition TCMR/MR are T-cell rich pathologies.

5.2 T-cell:myeloid cell lineage polarity

To investigate global trends in immune cell infiltrate and explore the differential presence of cohort-specific immune cell structures, I generate a pairwise heatmap of non-parametric Spearman's correlations [168] between patient-level immune cell proportions and immune cell densities. I generate these heatmaps for LN, RAR, NK, TCMR and MR separately. Spearman's rank correlation is ideal for ordinal or continuous data that defy the assumptions of parametric tests. By not assuming a specific distribution shape, nonparametric methods provide a more flexible approach to discerning statistical significance. They can be particularly powerful in biomedical research, where data distributions can be unpredictable, and sample sizes are often small. I prefer to use Spearman's rank correlation to avoid the assumptions of linearity or bivariate normality required for the more commonly used Pearson's linear correlation.

Using Spearman's rank correlation on immune cell densities and immune cell proportions has revealed striking patterns of covariance between commonly related and divergent cell populations in each disease (Figures 5.3-5). I include a secondary heatmap that only displays the uncorrected statistically significant Spearman's correlations ($P < 0.05$; Figure 5.3B; Figure 5.4B,D,F; Figure 5.5B,D). As expected, the significance heatmaps are identical for both density and proportion since Spearman's correlation measures the intensity of a monotonic relationship between two variables. In other words, the observed relationship between frequency data is preserved regardless if we normalize by the density or proportion. I initially used immune cell densities directly for these plots due to the intuitive and real biological meaning in using such a metric. I initially did not want to use proportion here since this feature is physically more abstract and depends on the particular inclusion of cell classes (ie proportion of all cells, the proportion of all classified cells, the proportion of only immune cells, etc). However, we find that generating these heatmaps using the proportions of all classified cells can help visualize global self-organization better.

In our LN cohort, globally, we see the self-organization of 3 main immune groups of common cells: 1) a T cell group that contained both CD4+ and CD8+ T-cells, 2) CD14+MerTk+ Mϕ, and 3) B cells CD14+CD163+ Mϕ (Figure 5.3A-B; Figure 5.6C-D). We observe additional co-variance blocks containing NK, NKT and neutrophils as well as a DC/pDC block. However, all of these latter populations were infrequent in situ. In addition to co-variance within each block, each separate block was, to some degree, inversely related to the others. This inverse or negative correlation was most striking for the blocks containing M1 (CD14+MerTk+) and M2 (CD14+CD163+) macrophages. Similar relationships were observed in RAR, although the correlations, both negative and positive, were less striking (Figure 5.5A-B,E-F). NK, on the other hand, has no clear patterns of immune-self organization.

We then performed a similar Spearman's analysis using patient-level immune cell densities

for both TCMR and MR subtypes of allograft rejection. In doing so, we observe apparent differences in global covariance of immune cell types between these cohorts. TCMR has a large T-cell-specific block of cells that covaries together, primarily independent of the myeloid cell compartment (Figure 5.6A-B). In MR on the other hand, the T-cell block covaries along with the myeloid cell lineages (Figure 5.6C-D). Interestingly, M1 (CD14+MerTk+) and M2 (CD14+CD163+) macrophages appear to compartmentalize separately once more, with a greater covariance of M1 with the T-cell block (Figure 5.6C-D). These data suggest that each disease is associated with specific, self-reinforcing immune states. In all, broadly shows that there are clear cell architectures/structures in LN and RAR that are not present in NK samples. This would agree with the tissue Figures in 3.3-4, which globally show dense immune cell aggregates/structures in LN/RAR that are absent in NK.

To better understand patient heterogeneity and immune cell polarization, we plot the per-patient density of the 3 immune cell lineages: myeloid cells (innate immunity), T-lymphocytes (adaptive immunity), and humoral cell lineages (adaptive immunity. For this plot we define the myeloid cell lineages as follows: CD14+CD163+ Mϕ, CD14+MerTk+ Mϕ, CD14+ Mϕ, CD16+ Mϕ, HLAII+ Monocytes, HLAII- Monocytes, Monocyte-Derived Mϕ, natural killer cells, Neutrophils, cDC1a, cDC2a, and pDCa. We further define the T-lymphocyte lineages with the following cell classes: CD3+ T-cells, CD4+CD8+ T-cells, CD4+ T-cells, CD8+ T-cells, NK T-cells and TCR$\gamma\delta$+ T-cells. Finally, B-cells, plasma cells, and plasmablasts are all binned into the humoral lineages.

Indeed, when we plot the per-patient myeloid cell density vs. T cell densities, we observe that biopsies either polarized towards a more myeloid-rich phenotype or a more T-cell-rich phenotype (Figure 5.3C). A representative image of some of the different in situ areas of inflammation is shown in Figure 5.4A. The T-cell axis is almost exclusively populated by the RAR cohort and the myeloid axis is mixed with mostly LN and some RAR. Very few samples have relatively higher in situ levels of B-cells/Plasma cells/plasmablasts, most of

which are LN patients. As expected, NK samples reside near the X,Y origins, indicating low basal levels of inflammation for all immune cell lineages. When we generate a similar plot overlaying TCMR/MR cohort identity, we observe that the samples that have the highest density of T-cells are mostly MR samples (Figure 5.6E). This greater T-cell infiltrate in MR matches reports of the particularly aggressive autoimmune phenotype observed in these patients [61].

5.3 M1 MerTk+ vs. M2 CD163+ polarity

Similarly, when we plot the biopsy density of CD14+MerTk+ M1 Mϕ and CD14+CD163+ M2 Mϕ we see a great heterogeneity in density data, yet these two populations tend to manifest reciprocal relationships (Figure 5.3D; Figure 5.6F) as seen in the prior heatmaps. We previously mentioned how in our Spearman's heatmaps we noted not only covariance within individual blocks but also a discernible inverse relationship among separate blocks. We observed that this negative correlation was particularly prominent between the blocks that included M1 (CD14+MerTk+) and M2 (CD14+CD163+) macrophages. This becomes obvious when comparing the X/Y relationship between these two populations in Figure 5.3C , with the X/Y relationship of T-cell density and myeloid cell density in Figure 5.3C). In particular, we find that LN biopsies lie along either a CD14+MerTk+ Mϕ and CD14+CD163+ Mϕ trajectory. Furthermore, no LN biopsies manifest a high density of both. In contrast, RAR biopsies tend to lie along the M1 Mϕ trajectory and do not display high M2 Mϕ densities. We further find that CD8+ T cell densities tended to co-occur more frequently with MerTk+ than CD163+ Mϕ, suggesting linked functions. Again, NK has a low density of both populations of M1 Mϕ and M2 Mϕ, as well as CD8+ T cells (Figure 5.3D). A representative image of some of the different in situ areas of inflammation is shown in Figure 5.4B. When we overlay TCMR/MR biopsy identity, we find that there are no overt cohort differences in M1/M2 Mϕ polarity between MR and TCMR, other than a slight shift towards

CD163+ macrophages in MR. However, up to this point, we are looking at global versus local relationships or features; we need to delve deeper into local cell-cell relationships to get a better understanding of the in situ immunity. For example, we want to answer questions about where these cells are. Are these cells actually interacting with one another in tissue?

Figure 5.3: Distinct immune trajectories are associated with distinct pathological states

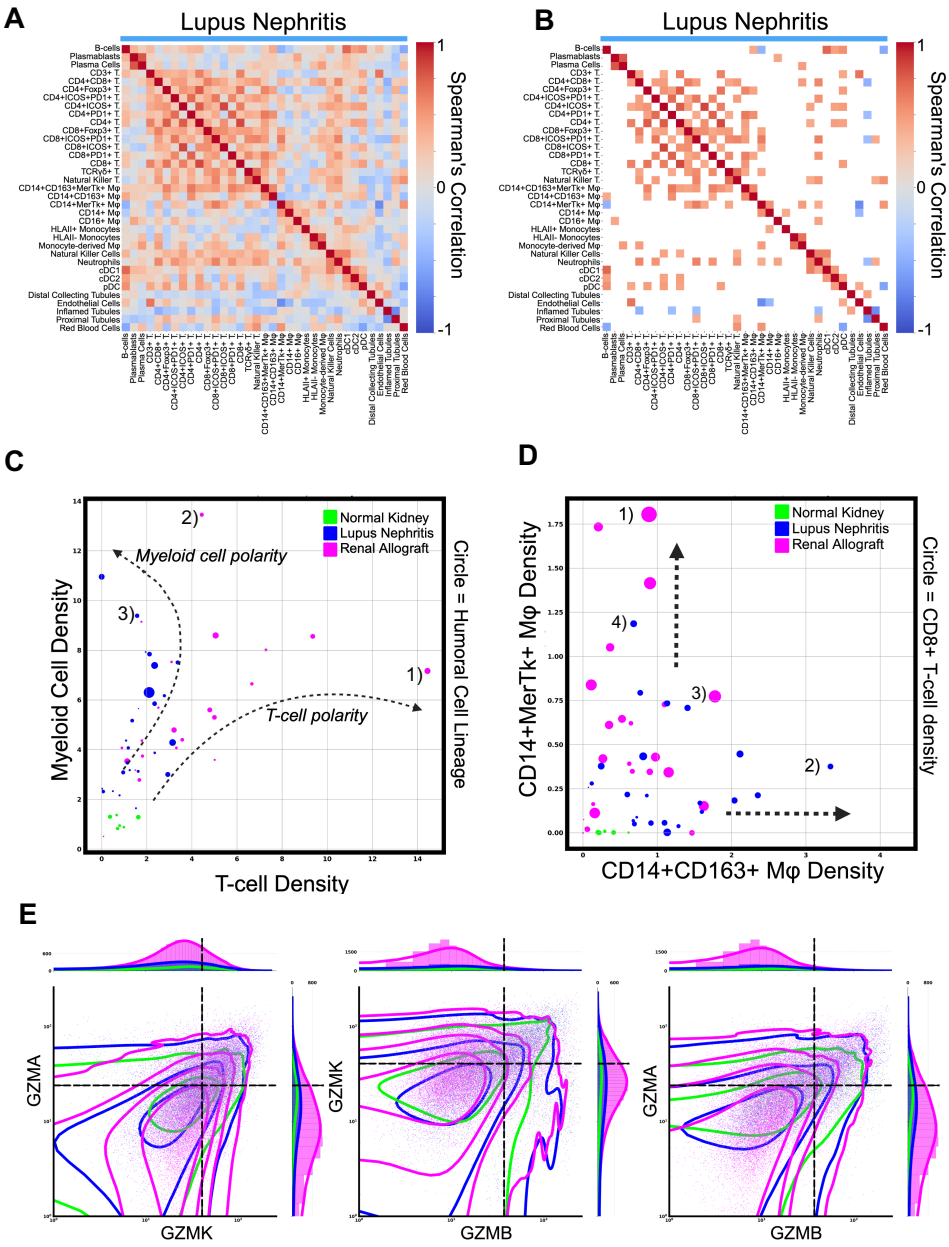

A) Heatmap of the non-parametric spearman's correlations between patient-level immune cell proportions for lupus nephritis patients. B) Heatmap of the uncorrected statistically significant Spearman's correlations $p < 0.05$ from A. C) Plot of the patient-level T-cell density (x-axis) and myeloid cell density (y-axis) colored by cohort Normal Kidney (green), Lupus Nephritis (blue), Renal Allograft (magenta). Representative images of tissue inflammation are shown in the following figure. D) Plot of the patient-level CD14+CD163+ macrophage density (x-axis) and CD14+MerTk+ macrophage density (y-axis) colored by cohort Normal Kidney (green), Lupus Nephritis (blue), Renal Allograft (magenta). E) Mean fluorescent intensity plots of GZMA, GZMB, and GZMK expression in CD8+ T-cells.

Figure 5.4: Distinct immune trajectories – microscopy examples of inflammation

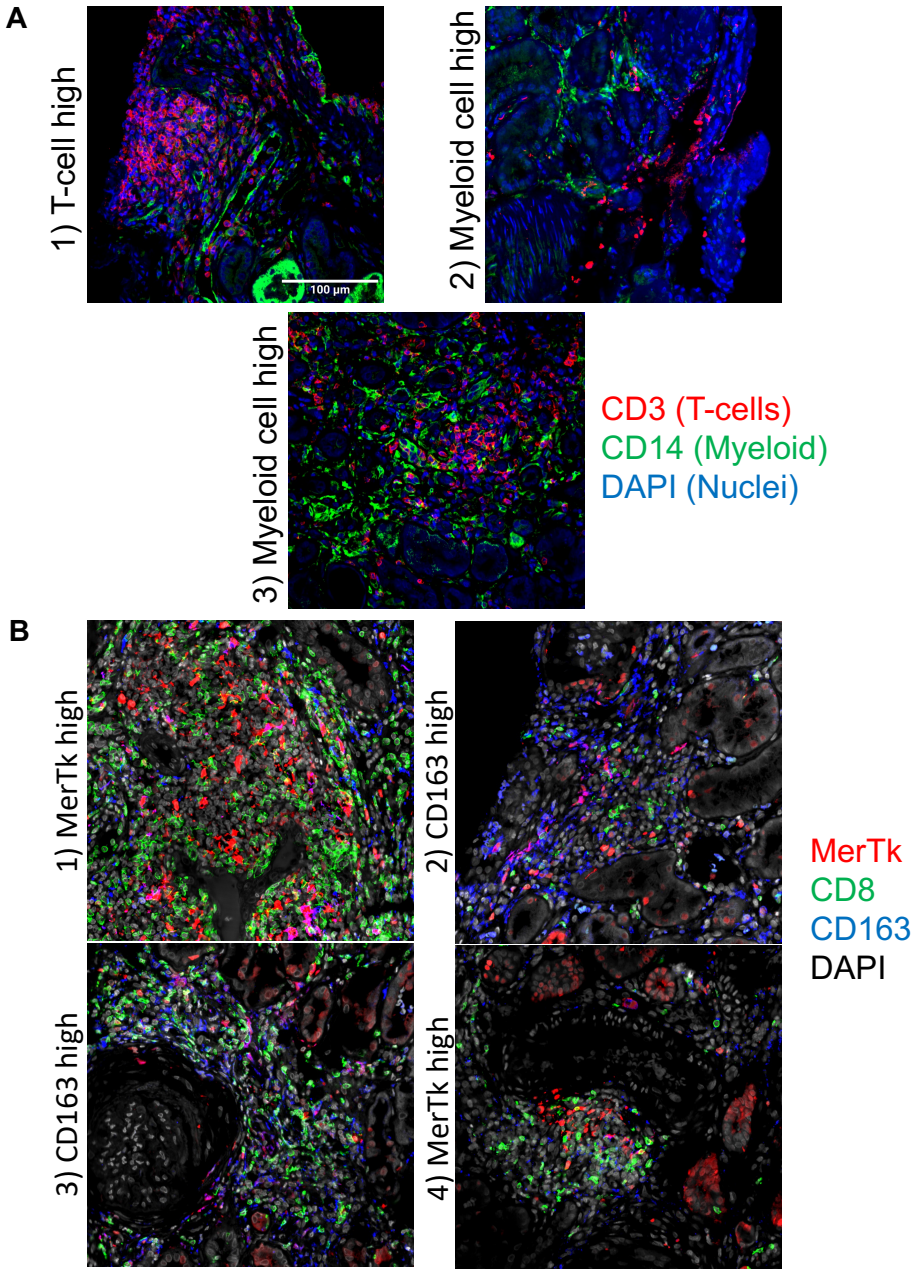

A) Representative images of tissue inflammation from 5.3C: 1) T-cell rich inflammation in RAR. 2) T-cell:Myeloid cell mixed inflammation in RAR. 3) Myeloid cell rich inflammation in LN. B) Representative images of tissue inflammation from 5.3D: 1) CD14+MerTK+ macrophage rich inflammation in RAR. 2) CD14+CD163+ macrophage rich inflammation in LN. 3) CD14+CD163+ macrohpage rich inflammation in RAR. CD14+MerTk+ macrophage rich inflammation in LN.

Figure 5.5: Cell class density and proportion correlation

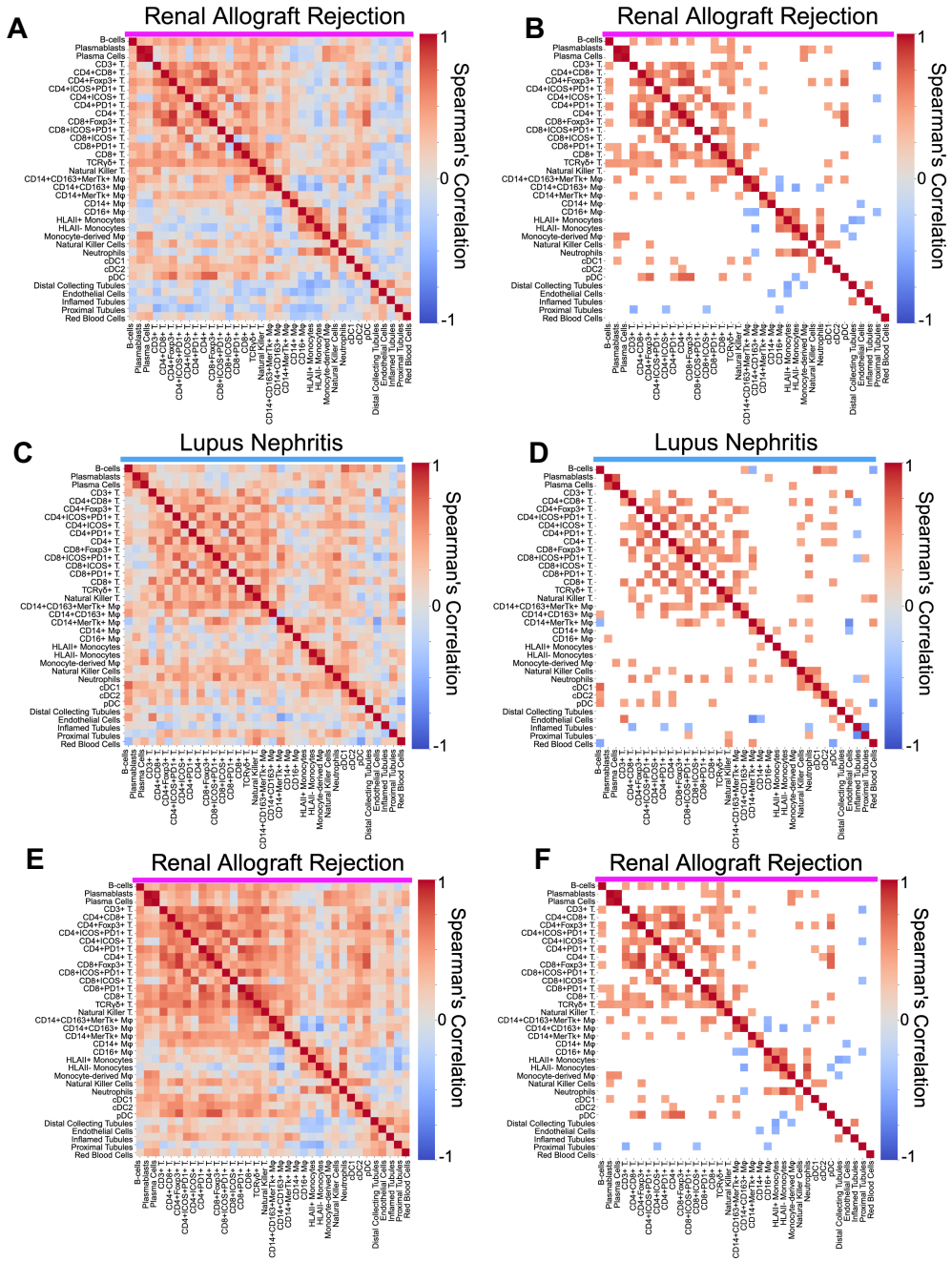

A) Heatmap of the non-parametric spearman's correlations between patient-level immune cell proportions for renal allograft patients. B) Heatmap of the uncorrected statistically significant Spearman's correlations $p < 0.05$ from A. C) Heatmap of the non-parametric spearman's correlations between patient-level immune cell density for lupus nephritis patients. D) Heatmap of the uncorrected statistically significant Spearman's correlations $p < 0.05$ from C. E) Heatmap of the non-parametric spearman's correlations between patient-level immune cell density for renal allograft patients. F) Heatmap of the uncorrected statistically significant Spearman's correlations $p < 0.05$ from E.

Figure 5.6: Distinct immune trajectories: MR – TCMR

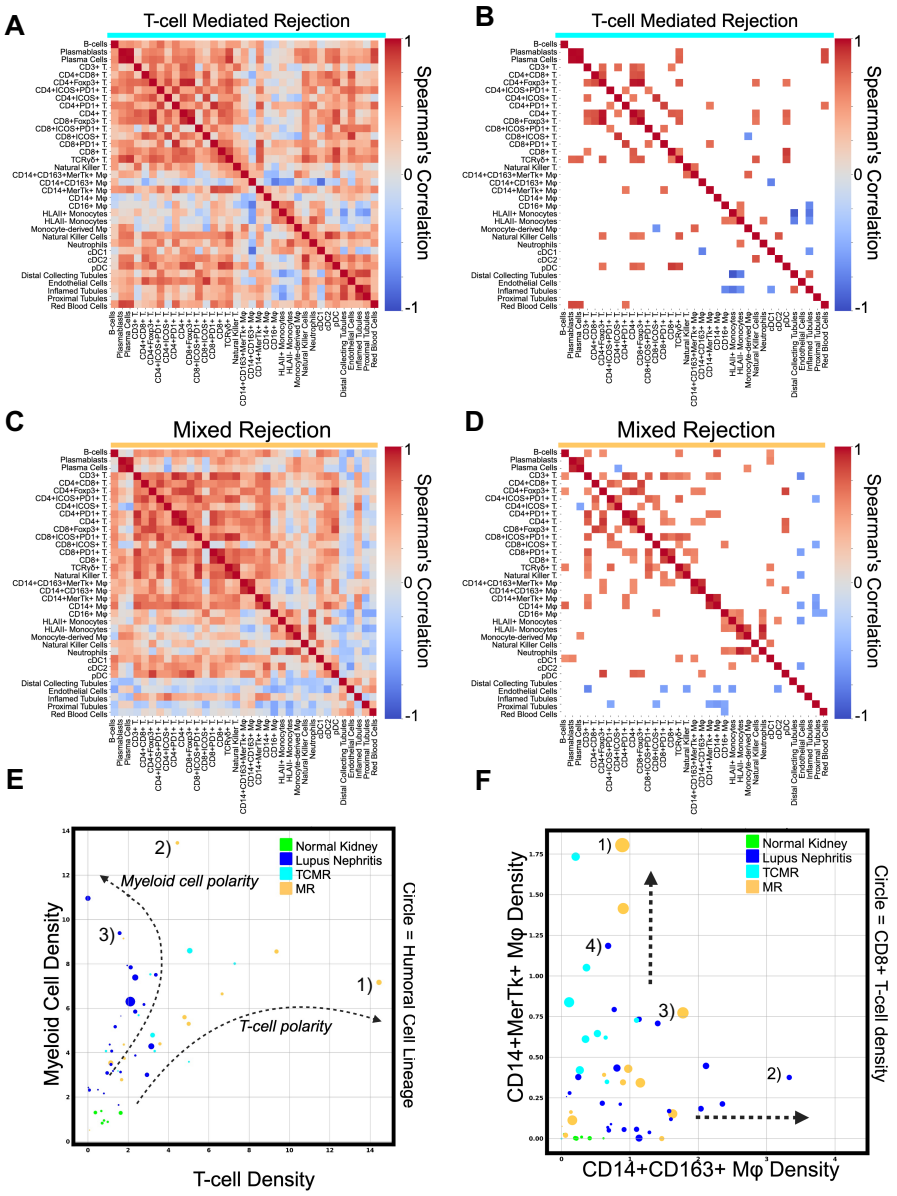

A) Heatmap of the non-parametric spearman's correlations between patient-level immune cell density for T-cell Mediated Rejection patients. B) Heatmap of the uncorrected statistically significant Spearman's correlations $p < 0.05$ from A. C) Heatmap of the non-parametric spearman's correlations between patient-level immune cell density for Mixed Rejection patients. D) Heatmap of the uncorrected statistically significant Spearman's correlations $p < 0.05$ from C. E) Plot of the patient-level T-cell density (x-axis) and myeloid cell density (y-axis) colored by cohort normal kidney (green), lupus nephritis (blue), T-cell mediated rejection (light blue), and mixed-rejection (orange). F) Plot of the patient-level CD14+CD163+ macrophage density (x-axis) and CD14+MerTk+ macrophage density (y-axis) colored by cohort normal kidney (green), lupus nephritis (blue), T-cell mediated rejection (light blue), and mixed-rejection (orange).

CHAPTER 6

CELLULAR DRIVERS OF INFLAMMATION

6.1 Promoters of tissue inflammation

We sought to explore the relationship between the density of CD8+ T-cells, M1 MerTk+ $M\phi$ and M2 CD163+ $M\phi$s with in situ inflammation and damage. We use the following definitions of tissue inflammation due to their biological relevance, simple interpretability, and ability to be generalized to other datasets that lack good quality clinical or histological features of tissue stress (as is our case): 1) total immune cell density (immune cell infiltration), 2) inflamed tubule density, 3) MXA coverage of the tissue, and 4) COLIII coverage of the tissue. Inflamed tubules were characterized by their diminished expression of MUC1/CD10, the canonical tubule markers, coupled with an elevated expression of Claudin1 as described in the cell marker background in Chapter 3 and shown in Figure 3.2 and Figure 3.4. MXA and COLIII coverage is characterized by segmenting positive marker signal with Otsu's method [160] to generate a mask of MXA/COLIII high regions. The MXA/COLIII score in our case is the IoU score of this MXA/COLIII high mask with a DAPI tissue mask (described in great technical detail in Chapter 7). To examine the cellular correlates of these tissue inflammation features we perform a standard Ordinary-Least-Squares (OLS) linear regression [169] between each cell population and the inflammation metric – by cohort. The P-values shown are uncorrected.

6.1.1 Immune cell density

Immune Cell Density in the biopsy tissue, aka immune infiltrate, is being used as a proxy for clinical inflammation. This is relatively self-explanatory as to why it is okay for us to do, as immune cell infiltrate is immune inflammation by definition. For example, in RAR and LN tubulointerstitial inflammation is histologically defined by the presence of immune cells

Figure 6.1: Cellular correlates of tissue inflammation and damage

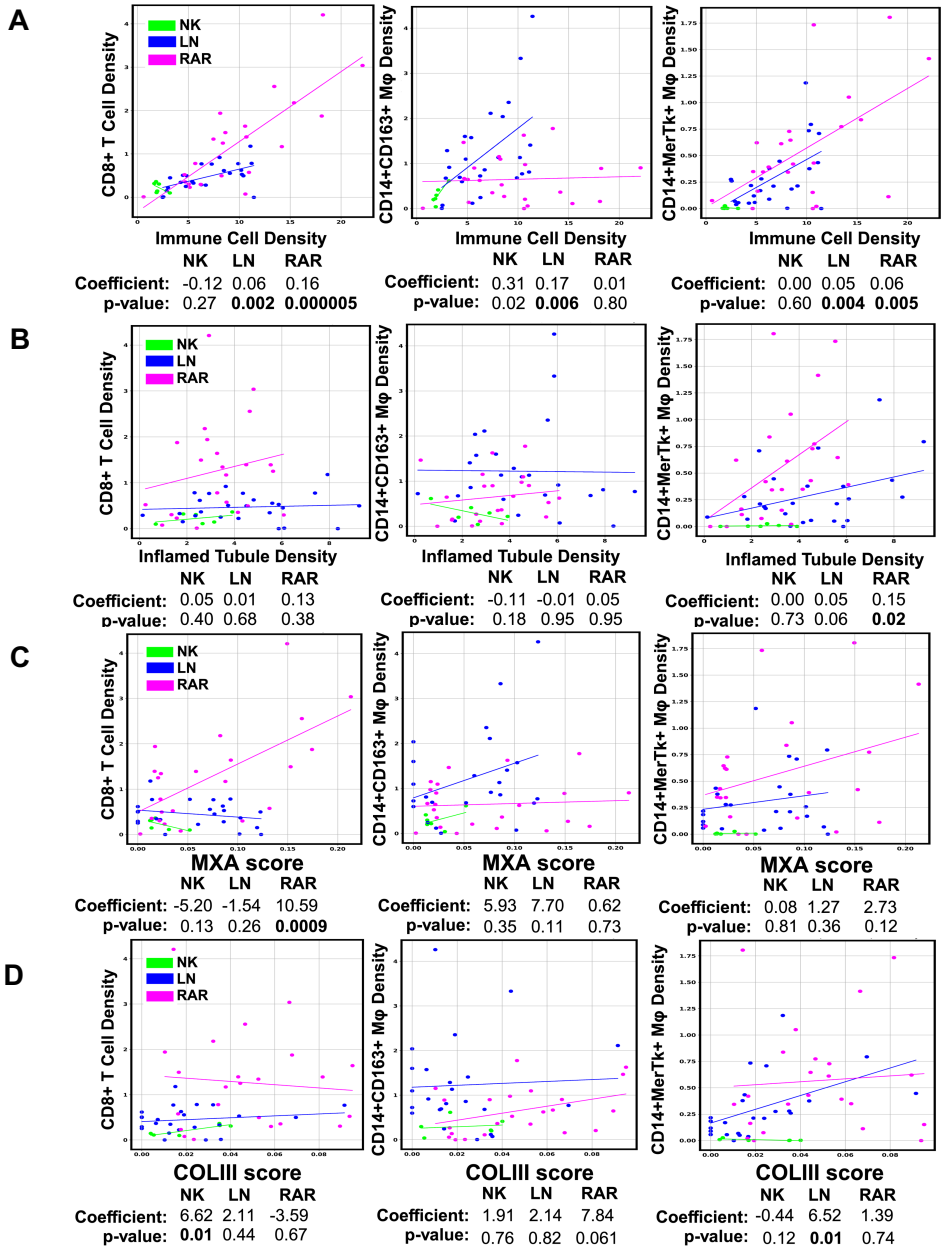

A) Immune cell density as a function of CD8+ T cell density (left), CD14+CD163+ macrophage density (middle), and CD14+MerTk+ macrophage density (right). Color indicates patient cohort: normal kidney (green), lupus nephritis (blue), renal allograft (magenta). Line shown is for linear trends assuming Ordinary Least Squares; the corresponding coefficients and p-values are shown. B) Inflamed tubule density as a function of CD8+ T cell density (left), CD14+CD163+ macrophage density (middle), and CD14+MerTk+ macrophage density (right). C) MXA score as a function of CD8+ T cell density (left), CD14+CD163+ macrophage density (middle), and CD14+MerTk+ macrophage density (right). D) Collagen III score as a function of CD8+ T cell density (left), CD14+CD163+ macrophage density (middle), and CD14+MerTk+ macrophage density (right).

Figure 6.2: Main cellular drivers of tissue inflammation – proportion

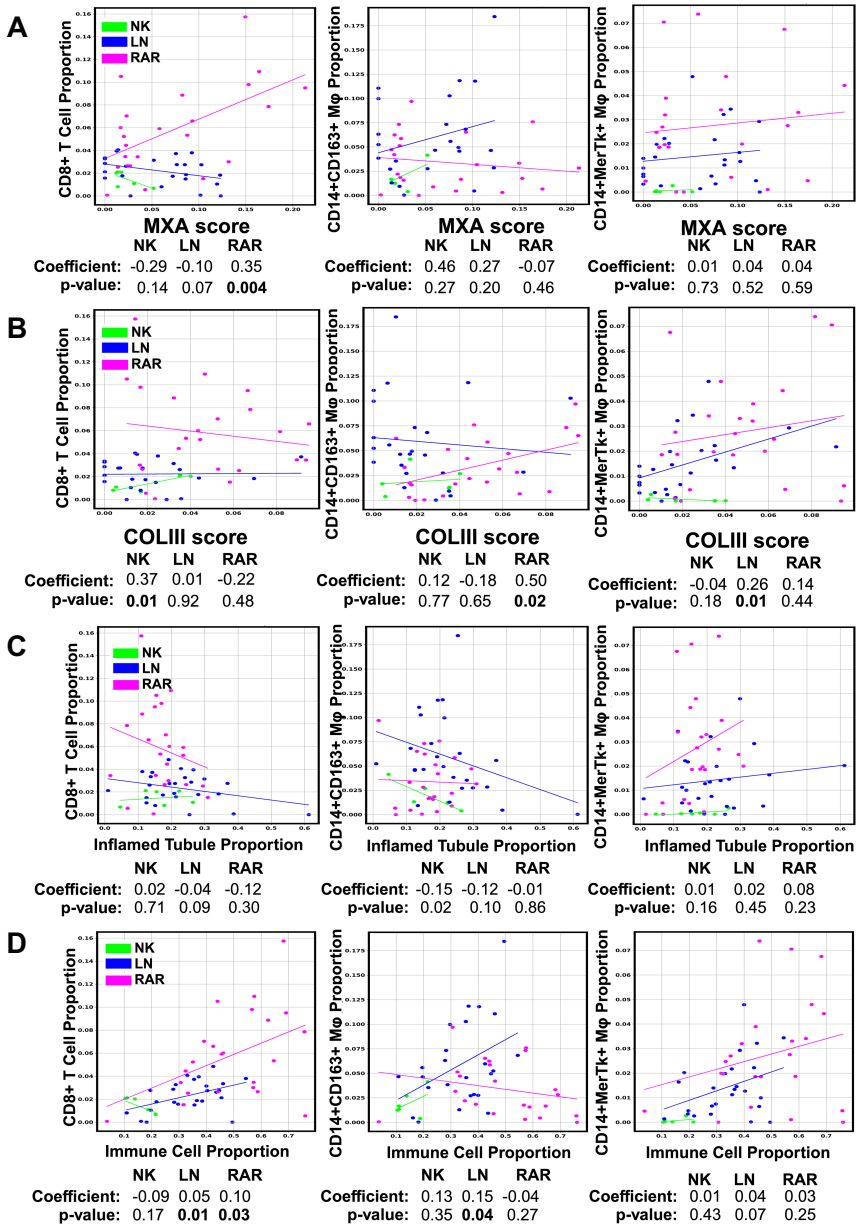

A) Immune cell density as a function of CD8+ T cell density (left), CD14+CD163+ macrophage density (middle), and CD14+MerTk+ macrophage density (right). Color indicates patient cohort: normal kidney (green), lupus nephritis (blue), renal allograft (magenta). Line shown is for linear trends assuming Ordinary Least Squares; the corresponding coefficients and p-values are shown. B) Inflamed tubule density as a function of CD8+ T cell density (left), CD14+CD163+ Macrophage density (middle), and CD14+MerTk+ macrophage density (right). C) MXA score as a function of CD8+ T cell density (left), CD14+CD163+ Macrophage density (middle), and CD14+MerTk+ macrophage density (right). D) Collagen III score as a function of CD8+ T cell density (left), CD14+CD163+ macrophage density (middle), and CD14+MerTk+ macrophage density (right).

Figure 6.3: Main cellular drivers of tissue inflammation – microscopy

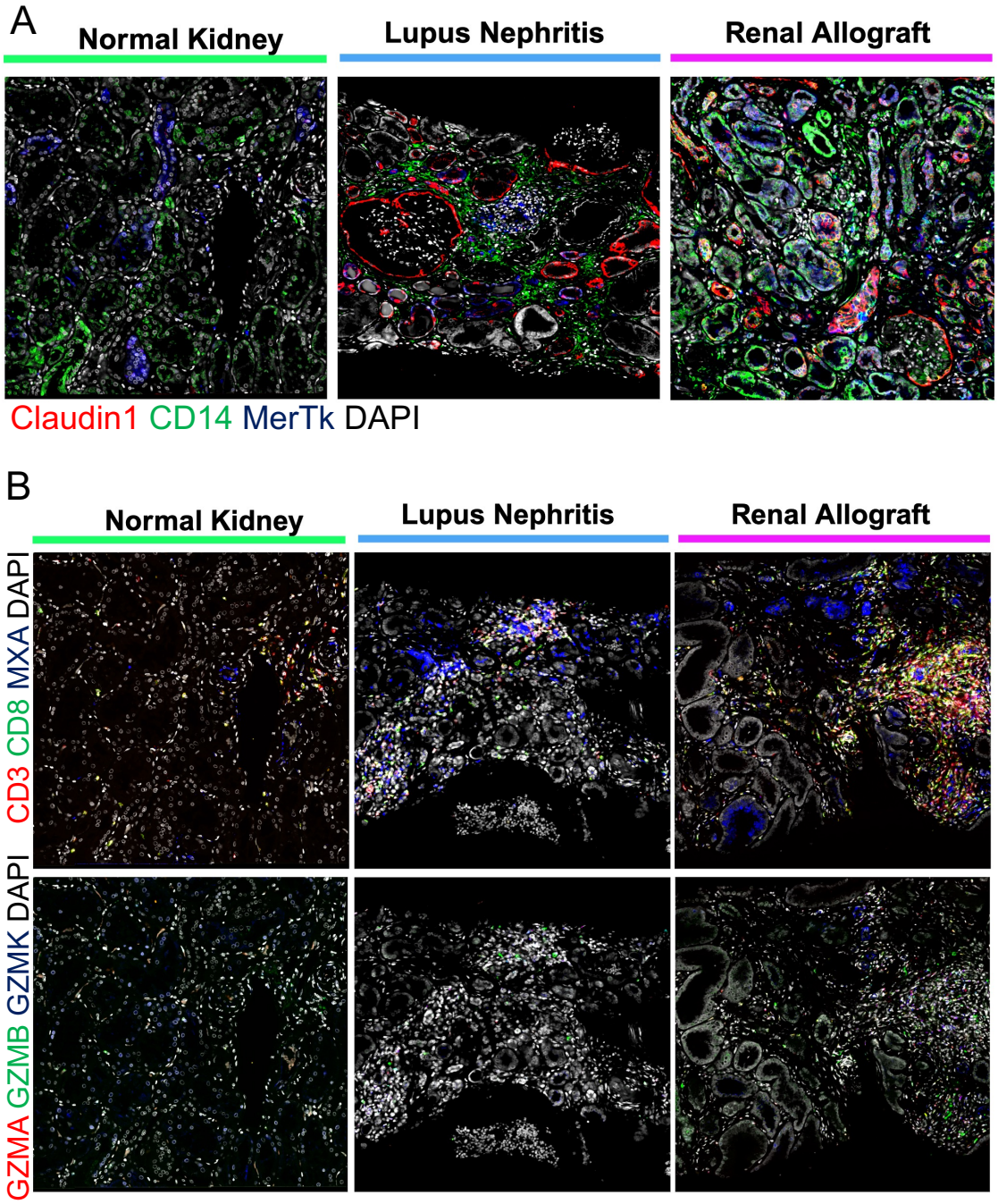

A) Representative examples of the relationship between CD14+MerTk+ and inflamed tubules in normal kidney (left), lupus nephritis (middle) and renal allograft (right) biopsies. Claudin1, CD14, MerTk, and Dapi is shown. B) Representative examples of the relationship between CD8+ T-cells and MXA in normal kidney (left), lupus nephritis (middle) and renal allograft (right) biopsies. CD3, CD8, MXA, and Dapi is shown (top row). GZMA, GZMB, GZMBK, and Dapi is shown (bottom row).

in the tubulointerstitial compartment.

When we examine total immune cell density we find that CD8+ T-cell density in tissue is significantly associated with immune cell infiltration in LN (β = 0.06; p = 0.002) and particularly RAR (β = 0.16; p = 0.000005), but not in NK controls (β = 0.16; p = 0.27) Figure 6.1A. We further find that, CD14+CD163+ M2 $M\phi$ density is significantly associated with immune cell infiltration in only our LN cohort (β = 0.17; p = 0.006), but not in RAR (β = 0.01; p = 0.80) and NK patients (β = 0.31; p = 0.02). Finally, when looking at the density of CD14+MerTk+ M1 $M\phi$ in tissue and immune infiltrate, we again see a statistically significant association in our autoimmune LN (β = 0.05 ; p = 0.004) and alloimmune RAR cohort (β = 0.06 ; p = 0.005), but not the NK control (β = 0.05 ; p = 0.60). For the sake of a comprehensive overview and feature consistency, we further explore the relationship between the proportion of CD8+ T-cells, M2 CD163+ $M\phi$, and M1 MerTk+ $M\phi$s and total immune cell proportion Figure 6.1D. In doing so, we find that CD8+ T-cell proportion is associated with a greater total proportion of immune cells in situ in LN (β = 0.05; p = 0.01) and RAR (β = 0.1; p = 0.03), but not in NK (β = -0.09 ; p = 0.17) similar in trend to density data. We further find a significant association between M2 CD163+ $M\phi$ and total immune cell proportion only in our LN cohort (β = 0.15 ; p = 0.04), and not RAR (β = -0.04 ; p = 0.27) and NK (β = 0.13 ; p = 0.35) respectively. We find no significant associations between M1 MerTk+ $M\phi$s and total immune cell proportion, although the positive trends agree with the density data.

The positive association of CD8+ T cells and Immune cell infiltrate in RAR is expected due to the cytotoxic activity of these cells in RAR, a defining feature of adaptive alloimmuity. Interestingly, the unexpected significant positive association in LN a appears to suggest that there may be a CD8+ T-cell inflammatory subphenotype in LN, aside from the observed M1/M2 Mϕ polarity. Moreover, both RAR and LN appear to have a positive association between M1 MerTk+ Mϕ and immune cell infiltrate. However, what complicates the inter-

pretation of this data is that we don't know if a cell is a bystander or is actively recruiting further immune infiltrates. We believe that the MXA and COLIII score would be more appropriate for capturing this potential relationship.

6.1.2 Inflamed tubule density

Inflamed tubules, defined by low CD10/MUC1 expression and the relative overexpression of Claudin1, were analyzed next as a proxy for tissue inflammation. When looking at CD8+ T-cell density in tissue, we do not find any significant relationships with total inflamed tubule density across all cohorts; NK (β = 0.05; p = 0.40), LN (β = 0.01; p = 0.68) and RAR (β = 0.13; p = 0.38) Figure 6.1B. Similarly, we find no significant association between M2 CD163+ $M\phi$ and inflamed tubule density; NK (β = -0.11; p = 0.18) , LN (β = -0.01; p = 0.95) and RAR (β = 0.05; p = 0.95). However, we do find a single significant association between M1 MerTk+ $M\phi$s in RAR (β = 0.15; p = 0.02), but not NK (β = 0.00; p = 0.73) and trending in LN (β = 0.05; p = 0.06). Conversely, we find no significant relationship between the proportion of CD8+ T-cells, M2 CD163+ $M\phi$, and M1 MerTk+ $M\phi$s and the total proportion of inflamed tubules in biopsy tissue (Figure 6.2A). Furthermore, the lack of statistical significance and completely flat trend lines for M2 CD163+ $M\phi$ density and inflamed tubule density leads us to believe that these cells do not induce tubular inflammation *directly*. Representative examples of the relationship between CD14+MerTk+ and inflamed tubules in our cohorts is shown in Figure 6.3A.

On the other hand, we know that MerTk plays a crucial role in efferocytosis, the process by which macrophages engulf and remove apoptotic cells. MerTK interacts with apoptotic cells via bridging molecules Gas6 or protein S, facilitating the recognition and binding to phosphatidylserine exposed on the surface of apoptotic cells as mentioned in the marker background in Chapter 3. Thus, considering this fact and the significant positive association between M1 MerTk+ $M\phi$s and inflamed tubules, I believe that these M1 cells interact with

tubules either for the resolution of tissue inflammation or as a maladaptive efferocytosis process leading to tubular injury. The much higher slope between M1 MerTk+ $M\phi$s and inflamed tubules in RAR might be indicative of a positive feedback loop with cytotoxic T-cells, given that CD8+ T-cells also trend positively and these cells co-vary together in RAR as seen in Chapter 5.

6.1.3 MXA and COLIII coverage

As described previously, MXA coverage is defined as the total proportion of the biopsy covered by the MXA-high tissue mask. When we use MXA as a proxy for tissue inflammation (or more precisely IFN-γ-driven inflammation), we find a single significant association between CD8+ T-cell density and MXA score in RAR (β = 10.59; p = 0.0009) only; but not in LN (β = -1.54; p = 0.26) and NK (β = -5.20; p = 0.13); Figure 6.1C. We find similar relationships between these variables when using proportion instead of cell densities; CD8+ T-cell proportion is significantly associated with MXA score in RAR (β = 0.35; p = 0.004), but not LN (β = -0.10; p = 0.35) and NK (β = -0.29; p = 0.14). Interestingly, the lack of a significant association here in LN, would suggest that CD8+ T-cell-driven inflammation is mostly independent of IFN-*gamma* signaling in LN biopsies. However, IFN-*gamma* signaling (MXA expression) does appear to be associated with cytotoxic CD8+ T-cell infiltrate particularly in RAR. The statistically significant trend here with CD8+ T-cells can be considered a "positive control", as we know cytotoxic T-cells drive alloimmune inflammation in RAR. Representative microscopy examples of the relationship between CD8+ T-cells and MXA in our cohorts is shown in Figure 6.3B.

When we use COLIII score as a proxy for tissue inflammation we find a more complex story. COLIII is a marker that is used to either capture tissue structure (essential for maintaining organ integrity), fibrosis/scarification, or tissue regeneration. The complication we have here is that we do not know if collagen deposition is maladaptive or not; so context

is extremely important. COLIII is redeposited in damaged tissue as a normal part of tissue repair, however, this repair in itself can be pathological in nature (ie liver scarring). In our analysis, we find that CD8+ T-cell density in tissue is significantly associated with COLIII score only in the NK control (β =6.62; p = 0.01), but not in our LN (β = 2.11 ; p = 0.44) and RAR (β = -3.59; p = 0.67) samples; Figure 6.1D. While this association does come as a surprise, we believe that this significant relationship in NK may be due to the nephrectomy sourcing of these biopsies. While these NK biopsies were deemed "negative" for inflammation by a pathologist, in theory, there may still be sub-clinical levels of immune cell infiltrate that is missed by the human eye. Moreover, we find no significant association between M2 CD163+ $M\phi$ density and COLIII score in NK (β = 1.91; p = 0.76), LN (β = 2.14; p = 0.82) and RAR (β = 7.84; p = 0.06) in line with MXA score results. However, when we consider the relationship between M1 MerTk+ $M\phi$s and collagen we find another single significant association in LN (β = 6.52; p = 0.01), and not RAR (β = 1.39; p = 0.74) and NK (β = -0.44; p = 0.12). This observed relationship may point to a more classical M1-like behavior (resolution of inflammation and tissue repair) of the MerTk+ Mϕs in LN.

Unremarkably, we find similar trends in COLIII score using proportion instead of density. CD8+ T-cell proportion is significantly associated with COLIII score only in NK (β = 0.37; p = 0.01), but not LN (β = 0.01; p = 0.92) and RAR (β = -0.22; p = 0.48). Similar to density, we see a significant relationship between M1 MerTk+ $M\phi$s proportion and COLIII in only LN (β = 0.26; p = 0.01), but not NK (β = -0.04; p = 0.18) and RAR (β = 0.14; p = 0.44). The important distinction with density metrics is that we now find a significant relationship between CD14+CD163+ M2 $M\phi$ proportion and COLIII score in RAR (β = 0.50; p = 0.02) , but not NK (β = 0.12; p = 0.77) and LN (β = -0.18; p = 0.02). Because of this data, we suspect that these CD14+CD163+ Mϕs may be directly contributing to scarification and stromal fibrosis in RAR biopsies.

CHAPTER 7

SPATIAL FEATURES OF AUTOIMMUNITY

Up to this point, we have mainly focused on global biopsy densities, however, the great intrabiopsy heterogeneity necessitated that we delve deeper into local spatial features to actually get a clearer understanding of the *in situ* local immune cell organization. Ie. We sought to answer questions such as: 1) Where are these cells in tissue? 2) Which immune cells are co-localized *in situ*? 3) Are immune cells directly interacting with one another through cell-cell contacts? We were particularly interested in local interactions between CD8+ T-cells and CD14+CD163+ Mϕ.

7.1 Higher-order spatial features

7.1.1 DBSCAN

Since areas of dense immune infiltrate are immunologically active and clinically important, we sought to capture these dense immune infiltrates in our biopsies. Furthermore, we had the secondary goal to phenotype these cellular communities for prognostically or immunologically important cellular networks. Therefore, we use DBSCAN [33] again [49] to find these cellular "neighborhoods" in our multiplex microscopy imaging data. We have already seen prior examples of these areas of dense immune aggregates in our LN and RAR samples in Figure 3.3 and Figure 3.5. However, when applying unsupervised clustering techniques for phenotyping, we have to consider that all clustering algorithms have two problems to solve essentially, 1) the number of latent “states” 2) feature space to characterize these said "states". The user must provide either or both, both cannot be unknown as that is unsolvable mathematically. In the case of K-means clustering [170], the user has to provide *a priori* a number of ideal clusters for the calculation of feature space centroids. Similarly, for algorithms like Leidan clustering [171], the user has to provide a resolution parameter for the feature space to solve

Figure 7.1: DBSCAN cell networks

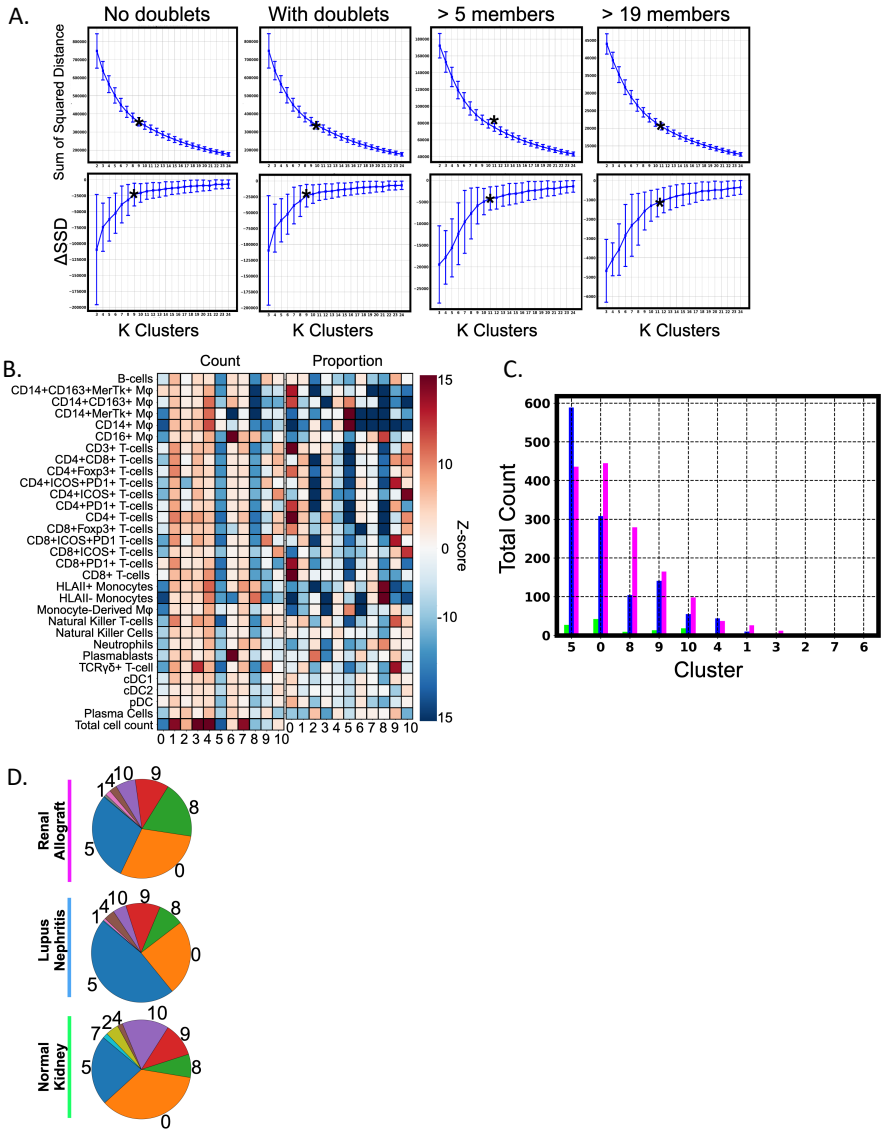

A) Bootstrap estimate of optimal K Clusters DBSCAN cell networks using: no doublets, with doublets, and above 5 cell members, and above 19 cell members respectively. Points are the average of 3000 repetitions with corresponding error bars. (Bottom) Δ sum of squared distances, and (top) sum of squared distances is shown. Asterisk indicates heuristic K optimal clusters for respective bootstrap experiment. B) Heatmap of the Z-score of Extracted Features from DBSCAN cell networks using an optimal K=11 means clustering, using above 19 cell members. (Left) cell count of the immune 30 cell types classified and the total cell count in the cell networks, (right) proportion of the same immune cells in the cell networks. C) Barplot showing the total count of the various K=11 DBSCAN cell networks colored by patient cohort: (green) normal kidney, (blue) lupus nephritis, and magenta) renal allograft. D) Piechart showing the proportion of the various K=11 DBSCAN cell networks by patient cohort: (bottom) normal kidney, (middle) lupus nephritis, and (top) renal allograft.

for the clusters.

Thus, to mitigate this issue, I employ a bootstrapping approach to estimate the ideal number of distinct latent (hidden) states, ie how many unique cell networks do we have? A similar approach was adopted in our prior work [49] shown in Figure 1.1C-E. Ideally, these estimated ideal number of states can then be used to guide further downstream algorithms, such as K-means and Leidan clustering. DBSCAN segmented cell networks represent areas of high immune infiltration and activity, this is salient for trying to understand active pathogenesis. To generate these cell networks, we apply DBSCAN at 150 pixels centroid-to-centroid using immune cell coordinates, the approximate size of a cell body, as done in our prior work. In doing so, we consider multiple bootstrapping scenarios: 1) inclusive of doublets -which are neighborhoods of N = 2 total cells- , 2) exclusive of doublets, 3) greater than 5 members, and 4) greater than 19 members.

In our prior LN paper we noticed that phenotyping cell neighborhoods exclusive of doublets was more beneficial; otherwise the doublets dominate the analysis and obscure the signal from large, infrequent, cellular aggregates [49]. That experience drove our choice of testing scenario 2 and scenario 3, and scenario 4 was suggested by our clinical collaborator Anita Chong. Consequently, I performed a bootstrap experiment using sklearn.cluster.DBSCAN in python, subsampling 75% of the DBSCAN data for a total of 3,000 repetitions; far above the N=250 bootstrap estimate experiment shown in Chapter 1 (Figure 1.1C). To phenotype these DBSCAN segmented cell neighborhoods, we perform feature extraction by characterizing each neighborhood using the cell class count and total proportion for each of our 30 immune cell classes; we include the total cell count as another descriptor. By using interpretable features like total number (effectively network size), and cell class count/proportion we can assign biologically meaningful phenotypes to our fitted cluster labels. For each iteration of the bootstrap, a 75% subsample of the DBSCAN neighborhoods is taken and then subsequently multiple K=2 to K=25 K-means clustering models are fitted to the boot-

strapped data using the features previously described. The sum of the squared distances for each fitted k is calculated and saved for downstream plotting. Using the average bootstrap sum of squared distance plot and the delta sum of square distance plot we find that the empirically best fit (using the 'elbow' method) K-clusters is around 9-11 (Fig. 4A). We use 11 as optimal K for downstream analysis; moving forward with phenotyping only those cell neighborhoods with 20 and more cell members, as suggested by Anita.

Afterwards, to find unique defining features for each of our clusters, I generate a heatmap of the leave-one-out Z-test for every cluster (Figure 7.1B) as done previously (Figure 1.1D). Based on the total cell count we find that clusters 0, 5, 8, and 9 have a smaller number of cells, while clusters 1,3,4 and 7 constitute large cell aggregates. Cluster 0,5,8, are the most biologically interesting, aside from being the most abundant neighborhood clusters in all of the cohorts (Figure 7.1C). Cluster 0 is rich in CD14+CD163+MerTk+ Mϕ, CD14+CD163+ Mϕ, CD3+ T-cells, CD4+ T-cells, and CD8+ T-cells. Cluster 5, on the other hand, is rich in CD14+ Mϕs and CD14+MerTk+ Mϕs, with residual amounts of Monocyte-derived Mϕs and CD14+CD163+ Mϕ. Finally, Cluster 8 is particularly rich in CD16+ Mϕ, HLAII+ Monocytes and HLAII- Monocytes.

This data is important on 3 fronts: 1) cluster 0 represents a CD163+ M2 Mϕ:T-cell network, where presumably antigen recognition occurs. 2) Cluster 5 represents a M1-like myeloid-rich cell network. 3) the in situ compartmentalization of cluster 0 and cluster 5 mirrors the M1/M2 antagonistic relationship seen in Spearman's correlation heatmaps and Figure 5.3D. The observed global M1-M2 polarization occurs at the in situ tissue level as well. The most abundant clusters are 5, 0, 8, 9, 10, 4, 1, 3, 2, 7, and 6 respectively; neighborhood abundance appears inversely proportional to number of cell members (7.1C). The vast majority of DBSCAN-segmented aggregates are found in LN and RAR but not in the NK control. This data would agree with the general lack of inflammation in NK controls. We further find that there is a great heterogeneity in the cohort-specific proportion of these

clusters (7.1D). Interestingly, in LN we observe a higher proportion of cluster 5 (M1) than cluster 0 (M2), while the proportion of these two clusters is more equal in RAR. Notably, we further see an expansion of Cluster 0 in RAR as well.

7.1.2 Cognate polarization algorithm

Cognate recognition (CR) is crucial for the effector function of the adaptive immune system, playing a role in cell-to-cell signaling, cell activation, and cytolysis [103, 172]. Immune synapse (IS) formation, driven by cognate recognition (CR), is a highly dynamic process broken into three phases 1) cell spreading 2) cell contraction, and 3) mature IS formation, which can be persistent for up to several hours. mTOC polarization towards the T-cell: antigen-presenting cell boundary is well documented as a characteristic of this process [103, 26]. A further polarization of CD43 to the distal end occurs when a mature IS is established after successful CR [104, 173]. An example diagram of this cellular/immunological process is shown in Figure 7.2A, as well as a representative three-dimensional surface reconstruction of this from lupus TII biopsy, utilizing Imaris software from the Clark-Giger lab's prior paper [26]. Although two-photon excitation microscopy has been a great tool for studying immune CR and the IS [174, 172], it is infeasible for the study of human tissue. The ability to detect cognate events in human tissue would allow us the unique opportunity to study how CR organizes and drives in situ immune responses.

There is a limit to the utility of human ground truth (GT) due to the high variability in human performance, even when done by expert readers. The traditional machine learning approach of using manual GT suffers from dataset feature specificity and would require careful normalization/standardization for future generalizability. mTOC polarization towards the T-cell:APC boundary is by definition, required for distinguishing between cognate and noncognate cells for the generation of manual GT segmentations. Thus, we are using extracted cell features as a proxy for mTOC polarization when mTOC polarization using

CV segmentation can be used directly instead. However, this increased specificity comes at the trade-off of limiting the application of this tool to datasets in which mTOC is present. Due to the aforementioned limitations, I decided to use computationally segmented images and mTOC polarization towards the APC:T-cell boundary directly, rather than using extracted features. This approach should be more generalizable versus using dataset-specific cell features.

To explore important biological behaviors such as cell-cell relationships, cytotoxic cell lysis, as well as immune cognate interactions, we have developed a computational method to detect mTOC cell polarity in MMI that is dataset agnostic. We consider this mTOC polarity algorithm to be essentially another spatial feature extraction method (since we use spatial data directly) that is indicative of high cell-cell interactions. In this approach, we use mTOC segmentation and cell body segmentations directly, giving us the flexibility to explore mTOC polarity between many possible cell-cell pairwise relationships in an unbiased manner. This method further avoids having to collect human expert segmentations of multiplex images, a notably difficult task as noted in the background in Chapter 3. Our mTOC tool is useful for detecting if cells are present locally either due to similar cytokine and chemokines leading co-recruitment or if a given pair of cells is interacting directly through cell-cell contacts.

In the development of this algorithm we collected two preliminary datasets. The first pilot dataset consisted of 2 LN FFPE renal biopsies stained with DAPI/CD3/CD4/BDCA2/mTOC to capture CD4+ T-cells (CD3+/CD4+/DAPI) and pDCS (BDCA2+/DAPI). The second expanded dataset consisted of 7 LN FFPE biopsies stained with DAPI, CD3, CD4, CD8, BDCA2, and mTOC to capture CD4+ T-cells, CD8+ T-cells (CD3+/CD8+/DAPI), and pDCS (Figure 7.2C). Both these datasets were imaged on a Leica SP5 laser-scanning confocal microscope, capturing 1024x1024 pixel images of immune infiltrate at a pixel size of 0.14 μm. After imaging, I used the prior T-cell Mask R-CNN and pDC Mask R-CNN segmentation networks developed, by Madeline Durkee (Torcasso) and Reba Abraham [49],

Figure 7.2: mTOC polarization background and preliminary data

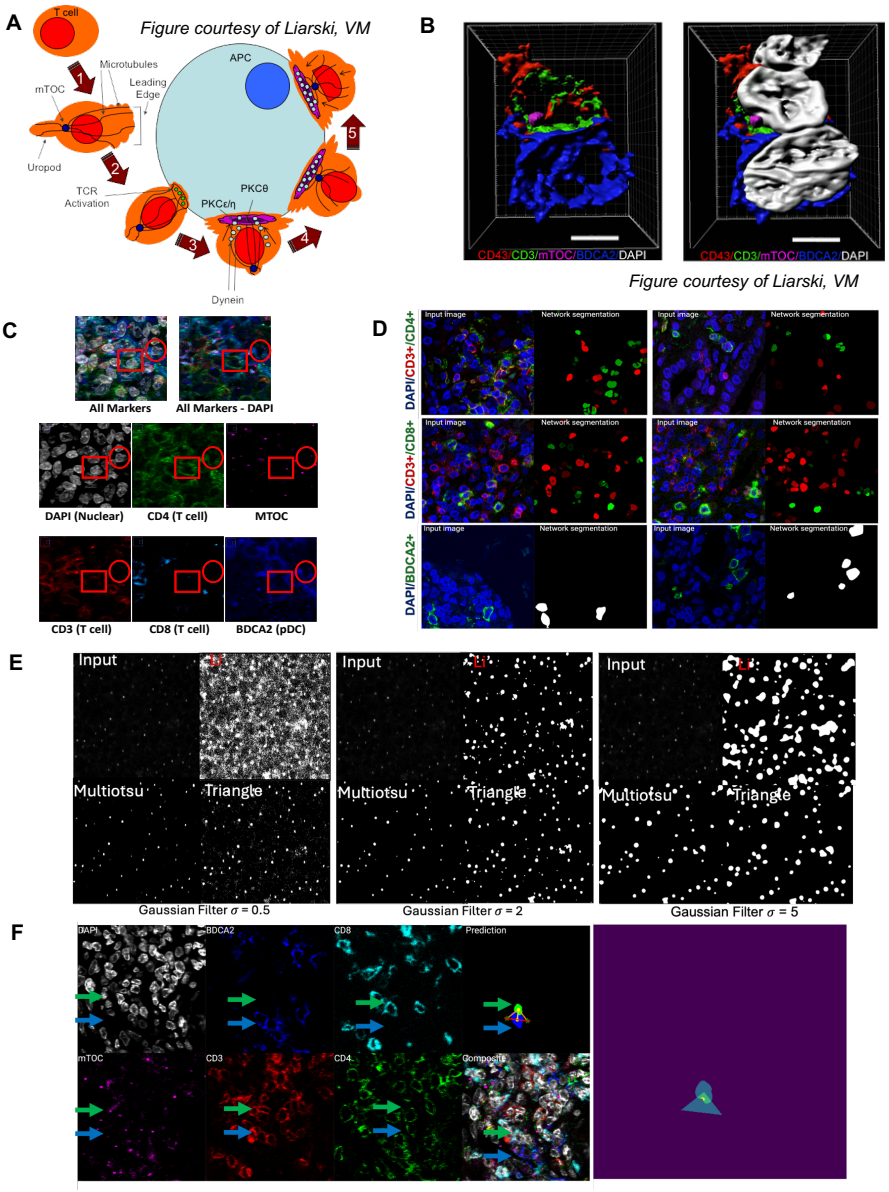

A) Representative diagram of mTOC polarization and TCR engagement with APC. Figure provided by Liarski VM [25]. B) Three-dimensional surface reconstructions from lupus TII, utilizing Imaris software. T cell abutting a pDC is shown with (left) and without (right) nuclei. Scale bar: 4 μm. C) Example imaging of mTOC expanded pilot dataset. LN biopsies from 7 de-identified patients obtained from the Human Tissue Resource Center. 1024 x 1024 pixel images. Pixel size is 0.14 μm. D) (left) input marker channels into T-cell Mask R-CNN network and pDC Mask R-CNN network. (right) resulting Mask R-CNN segmentation masks. E) Example images of various gaussian filters (ie $\sigma = 0.5, 2.0, 5.0$) and pixel thresholding methods (Multiostu/Li/Triangle) for mTOC segmentation. F) pDC:CD3+CD8+ T-cell polarization identified using the mTOC algorithm. DAPI/BDCA2/CD3/CD4/CD8/mTOC markers are shown. Green arrow points to T-cell, blue arrow points to pDC. (right) corresponding cell and mTOC segmentation masks

to perform instance segmentation for the aforementioned cell classes. The T-cell Mask R-CNN network segmented double positive (CD3+/CD4+ or CD3+/CD8+) or single positive (CD3+) cells, while the pDC Mask R-CNN network segmented a single positive cell class based on BDCA2+ expression and DAPI signal (Figure 7.2D). After experimenting with various combinations of gaussian filters (ie $\sigma = 0.5, 2.0, 5.0$) and pixel thresholding methods (Multiostu/Li/Triangle), I find that a gaussian filter of $\sigma = 2.0$ and Multiotsu thresholding (3 class, 2nd threshold) gave the best mTOC segmentations qualitatively (Figure 7.2E).

The algorithm begins by considering the mTOC object size, proceeding only with mTOC segmentation objects within a specific pixel range (5-160 pixels) of expected physical size (Figure 7.3A). Only cells with a single mTOC segmentation object are considered; cells without a mTOC segmentation are not included. In a subsequent step, two lines $L1$ and $L2$ are generated. $L1$ is the line connecting the centroid of the cell of interest (ie T-cells) to the centroid of a reference cell (ie APCs like pDC). $L2$ is then generated to be perpendicular to $L1$. The algorithm then takes a user-defined parameter, angle θ from line $L1$, to generate a triangle mask connecting the centroid of the cell of interest to two points along line $L2$ as shown in Figure 7.3A. These two points on $L2$ are calculated using linear algebra and the given angle θ. The resulting triangle mask is then merged with the cell body mask (of the current cell under consideration) to create a "proximal" mask; a "distal" mask is generated by subtracting the "proximal" mask from the cell body mask. If the majority of the pixels in the mTOC segmentation mask are located in the "proximal" mask the cell is classified as being polarized. Conversely, if the majority of the mTOC segmentation mask pixels are located in the "distal" mask the cell is classified as non-polarized. Our mTOC polarity method can capture putative cognate interactions between target cells of interest, in this case, a pDC:CD8+ T-cell pair in the pilot dataset (Figure 7.2F) and a CD4+ T-cell:CD8+ T-cell pair in the CODEX dataset (Figure 7.3B).

When looking at the violin plots of absolute counts of mTOC polarization between B-

cells:CD4+PD1+ T-cells and B-cells:CD4+ICOS+ T-cells, we find an enrichment of these interactions in the MR cohort in particular (Figure 7.3). This is important as it validates prior findings of an association of cognate interaction between these cells and MR [25]. When we perform a WMU test, we find a statistically significant increase in the polarization of B-cells:CD4+PD1+ T-cells comparing RAR-NK ($p = 0.009$), and of B-cells:CD4+ICOS+ T-cells comparing RAR-NK ($p = 0.04$) and RAR-LN ($p = 0.01$) respectively (Figure 7.3 F). The cell segmentations acquired from Cellpose is analogous to features extracted using a mathematical function (in this case a network). We can use these "features" to identify CR using a decision tree classifier which is based upon known biology Figure 7.3A. The direct use of cell segmentations and mTOC make this algorithm compatible with the other CV pipelines, expanding the accessibility of this tool to MMI methods other than CODEX. This algorithm integrates mTOC segmentation and cell body segmentations, analogous to feature extraction, to evaluate cell polarity in a geometric manner. I assume that there are no cohort-specific biases or errors in applying this algorithm across our biopsies.

We were further interested in using this tool to explore T-cell mTOC polarization with CD14+CD163+ M2 Mϕs and CD14+MerTk+ M1 Mϕs. In doing, so we find a statistically significant enrichment of polarization between CD14+MerTk+Mϕ:CD8+ T-cells comparing NK-LN ($p = 0.02$), NK-RAR ($p = 0.003$), and LN-RAR ($p = 0.004$). Similarly, we find a significant enrichment between CD14+MerTk+Mϕ:CD4+ T-cells comparing NK-LN ($p = 0.006$), NK-RAR ($p = 0.0009$), and LN-RAR ($p = 0.009$). When looking at CD163+ Mϕ, we find a significant enrichment between CD14+CD163+Mϕ:CD8+ T-cells comparing NK-LN ($p = 0.009$), NK-RAR ($p = 0.009$); CD14+CD163+Mϕ:CD4+ T-cells comparing NK-LN ($p = 0.03$), NK-RAR ($p = 0.03$) as well. (Figure 7.3 E-F). The enrichment of mTOC polarity in T-cells, particularly CD8+ T-cells, further suggests that T-cells drive inflammatory activity in RAR. We believe that MerTk+ macrophages in-migrate to tubules (causing tubulitis) in RAR, where they phagocytose tubular material, and sequentially present antigen to CD8+

Figure 7.3: mTOC polarization tool

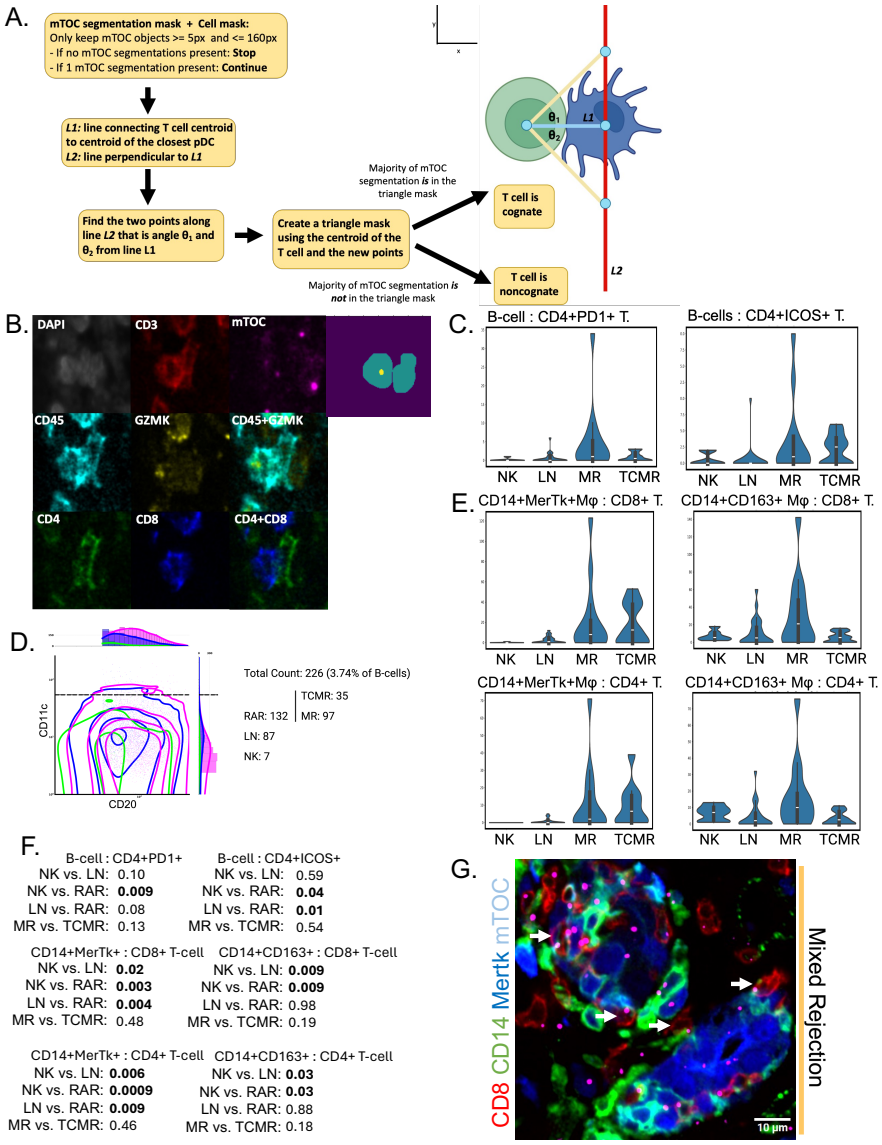

A) Biology-based decision tree classifier for computationally detecting mTOC polarization between cells; putative for immune cognate interactions. The network segmentation is analogous to performing feature extraction on the images. B) Example of a CD4+ T-cell and CD8+ T-cell identified as in a cognate pair. CODEX markers for T-cells are shown. mTOC segmentation (yellow), and cell segmentations (cyan). C) Violin plot of absolute counts of pairwise mTOC polarization between major immune cell-cell relationships detected by algorithm. Counts are shown by patient cohort. D) Mean fluorescent intensity plot of CD11c expression in B-cells (left). Absolute count of CD11c+ B-cells by cohort, positivity determined using Otsu's method. E) Violin plot of counts of pairwise mTOC polarization between CD8+ T-cells/CD4+ T-cells and M1 or M2 macrophages. F) Mann Whitney-U test of the differential abundance of mTOC polarization between cohorts. G) Representative example of CD14+MerTk+:CD8+ T-cell cognate events within tubules in a mixed rejection sample (RAR).

T-cells (as captured by polarized mTOC) for the activation of T-cell inflammatory cell programs. A representative example of CD14+MerTk+:CD8+ T-cell cognate events within tubules in a mixed rejection sample (RAR) is shown in Figure 7.3G.

7.2 Compartment analysis

While there seems to be no difference in the Tubular density in the tissue between our cohorts, 355± 31 tubules/mm2 in NK, 339 ± 53 tubules/mm2 in LN, and 367 ± 81 tubules/mm2, we see that the morphological features such as Area, Perimeter, Major Axis length, and Equivalent diameter are greater in LN and RAR cohorts (Figure 7.4). This increase in tubular morphology features can most likely be attributed to the presence of immune infiltrate within tubules under pathologic conditions. On the other hand, there are no obvious cohort differences in our glomerular features. The average tissue area per biopsy is much larger for our NK cohorts (14.39 ± 4.03) than for LN (2.19 ± 0.91) and RAR (2.80 ± 1.24) cohorts. This can be attributed to the different clinical contexts of these biopsies, our NK cohort is a nephrectomy sample while our LN and RAR cohorts are diagnostic biopsies. As expected, the total biopsy area covered in COLIII high areas, putative for fibrotic tissue, is more significant in LN (0.07 ± 0.04) and RAR (0.07 ± 0.03) than the normal NK control (0.04 ± 0) in line with the increased inflammation and immune infiltrate in the pathologic cohorts.

7.2.1 Tissue compartment segmentation

Since we found that CD163+ and MerTk+ macrophages compartmentalized using the DBSCAN method we sought to investigate how immune cells were distributed in the various kidney structural compartments. We were interesting in the differential distribution of immune cells in the following anatomical compartments: 1) tissue interstitium, 2) tubular border, 3) glomerular border, 4) tubules, 5) glomeruli (Figure 7.4A-D). MXA high areas and COLIII high areas were also investigated as "compartments" of biological value, areas of high

Figure 7.4: Kidney compartment segmentation workflow

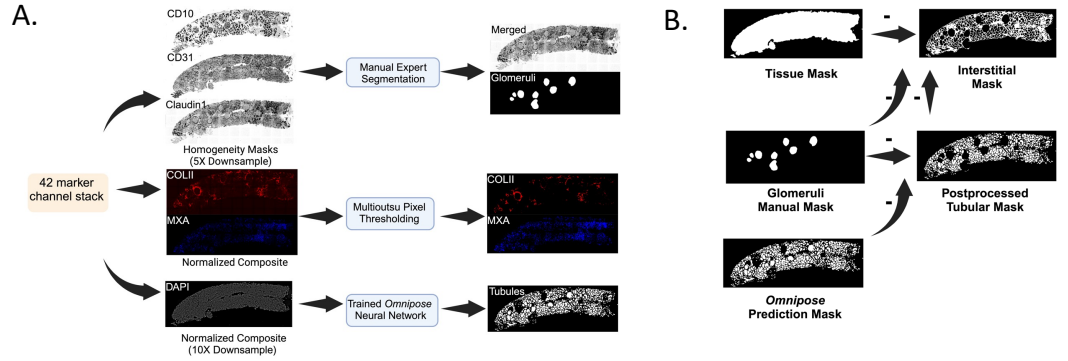

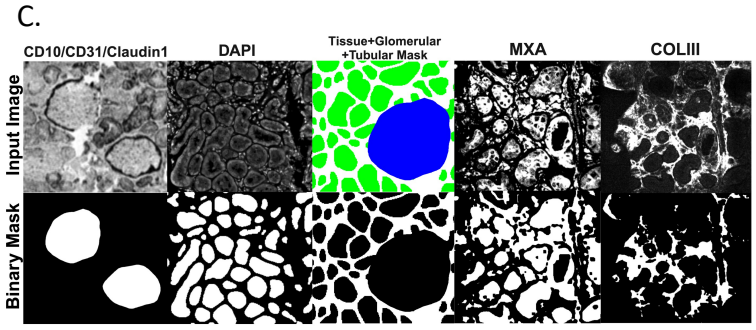

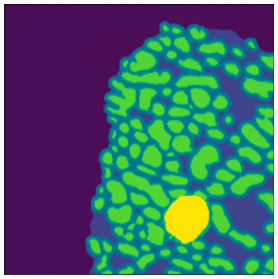

E.

Tissue characteristics	NK	LN	RA
Tubular Features:			
Density in tissue mm² (μ ± σ)	355.01 ± 31.82	339.19 ± 53.93	367.14 ± 81.39
Area μm² (μ ± σ)	961.97 ± 427.28	1259.37 ± 377.09	1153.84 ± 312.21
Perimeter μm (μ ± σ)	137.34 ± 35.00	161.74 ± 28.61	152.67 ± 22.42
Major Axis Length μm (μ ± σ)	41.98 ±10.68	49.25 ± 8.69	46.42 ± 6.73
Minor Axis Length μm (μ ± σ)	23.34 ± 4.68	26.66 ± 3.32	25.67 ± 2.57
Equivalent Diameter μm (μ ± σ)	29.60 ± 6.56	33.92 ± 4.67	32.57 ± 3.64
Glomerular Features:			
Density in tissue mm² (μ ± σ)	1.72 ± 1.45	2.07 ± 1.52	2.60 ± 1.68
Area μm² (μ ± σ)	18114.1 ± 4599.5	20100.7 ± 10452.9	16894.0 ± 7302.9
Perimeter μm (μ ± σ)	604.13 ± 89.78	473.44 ± 206.03	472.44 ± 168.83
Major Axis Length μm (μ ± σ)	168.63 ± 31.45	156.35 ± 70.03	154.14 ± 55.32
Minor Axis Length μm (μ ± σ)	130.33 ± 14.62	122.52 ± 51.25	121.38 ± 43.29
Equivalent Diameter μm (μ ± σ)	145.21 ± 21.08	137.02 ± 58.56	135.37 ± 48.25
Other Features:			
Tissue Area mm²(μ ± σ)	14.39 ± 4.03	2.19 ± 0.91	2.80 ± 1.24
Interstitial Area mm² (μ ± σ)	9.25 ± 3.48	1.18 ± 0.54	1.54 ± 0.68
Tubular Area mm² (μ ± σ)	4.69 ± 1.53	0.90 ± 0.44	1.14 ± 0.56
Glomerular Area mm² (μ ± σ)	0.45 ± 0.39	0.12 ± 0.11	0.12 ± 0.08
MXA Area mm² (μ ± σ)	3.51 ± 1.21	0.28 ± 0.19	0.47 ± 0.26
COLIII Area mm² (μ ± σ)	0.54 ± 0.11	0.16 ± 0.12	0.19 ± 0.14
MXA mask coverage	0.24 ± 0.07	0.13 ± 0.06	0.17 ± 0.06
COLIII mask coverage	0.04 ± 0.00	0.07 ± 0.04	0.07 ± 0.03

A) Workflow of the procedure adopted for acquiring the computational segmentation of COLIII high area, MXA high areas, tubules, and glomeruli. B) Procedure adopted for the creation of the interstitial mask and post-processed tubular mask. C) Zoomed representative images of kidney compartment segmentations. Input image (top) and resulting binary mask (bottom). From left: glomeruli, tubules, interstitium, MXA, and COL III. D) Example figure of all 5 kidney compartment: 0) slide background, 1) tissue interstitium, 2) border of tubules, 3) border of glomeruli, 4) tubules, and 5) glomeruli. E) Summary table of patient-level morphological features calculated from mask segmentations of the various kidney compartments. (Left) normal kidney, (middle) lupus nephritis, and (right) renal allograft.

interferon-driven inflammation and areas of high scarification respectively. A combination of various computer vision approaches, such as manual expert segmentation, multiotsu pixel thresholding, and Omnipose network segmentation were employed to define these categorical compartments from MMI (Figure 7.4A-D). The Omnipose network was developed by Thao Cao and the glomerular manual segmentation was done by Junting Ai (Lily). The manual glomerular mask is combined with the Omnipose tubular prediction mask to produce a post-processed tubular mask which is used for downstream analyses (Figure 7.4B). The tubular and glomerular masks are subtracted from a tissue mask to generate an interstitial stromal mask for downstream analyses. The compartment analysis is something we can uniquely do using highly multiplexed imaging. In all, we are confident that the binary masks of the renal compartments that we have generated are of high quality (Figure 7.3C).

7.2.2 Compartmentalisation of inflammation

When looking at our kidney structure masks, we find that the periglomerular mask has the highest proportion and density of immune cells in both RAR and LN; 37.43 and 45.39 cells per mm^2 respectively (Figure 7.5 A/B). We have already seen some examples of periglomerular inflammation in Figure 3.3. Furthermore, we do see minor signs that interstitial and tubular inflammation is higher in the RAR cohort relative to LN and NK. In general, the NK control has low levels of immune infiltration across all the renal compartments as expected. When comparing the inside of the MXA mask, the dilated MXA border mask, and all other tissue, we find that the MXA mask effectively captures areas of high immune cell density in both LN and RAR, but not NK (Figure 7.5C). This would suggest that we can use our MXA mask to specifically select for areas of active inflammation in MMI imaging; either of potential prognostic value or for future study (ie feature extraction using texture). Interestingly, the COLIII mask does not capture areas of high immune cell density with as much fidelity as MXA. This would align with our expectation of hypocellularity in fibrotic regions. To

better capture this compartmentalization, I generate multiple violin plots of the patient-level average cell count per mm^2 for our major immune players: CD8+ T-cells, CD4+ T-cells, CD14+CD163+ M2 Mϕ, CD14+MerTk+ M1 Mϕ, B-cells, and plasma cells. The latter two cell classes are included since LN/SLE is traditionally seen as a B-cell disease. Consequently, we observed higher densities, as well as heterogeneity, in CD8+ T-cell and CD4+ T-cells across the renal compartments in RAR particularly. Interestingly, plasma cell densities are low in most compartments in our cohorts, except for a relative spike in the glomerular border for LN biopsies. We observe a high variance in CD14+MerTK+ Mϕs in the interstitium, tubule, and tubular border of RAR samples. This population appears relatively limited mostly to the interstitium and glomerular border in LN. The higher heterogeneity of CD14+CD163+ Mϕ density in LN appears to be mostly limited to interstitial and tubular regions, indicative of tubulointerstitial inflammation (TI). We again find that the glomerular border has the highest density of immune cell infiltrate, however, the large variance in this compartment would suggest various immune subphenotypes in LN and RAR. We postulate that this high variance across cohorts is due to normal tissue (ie healthy tubules) obstructing the signal from high inflammation areas, a more targeted focus on inflamed tubules and glomeruli should unravel some of this heterogeneity. Thao Cao is currently developing a classifier for inflamed tubules for these exploratory purposes.

Figure 7.5: Kidney compartment analysis

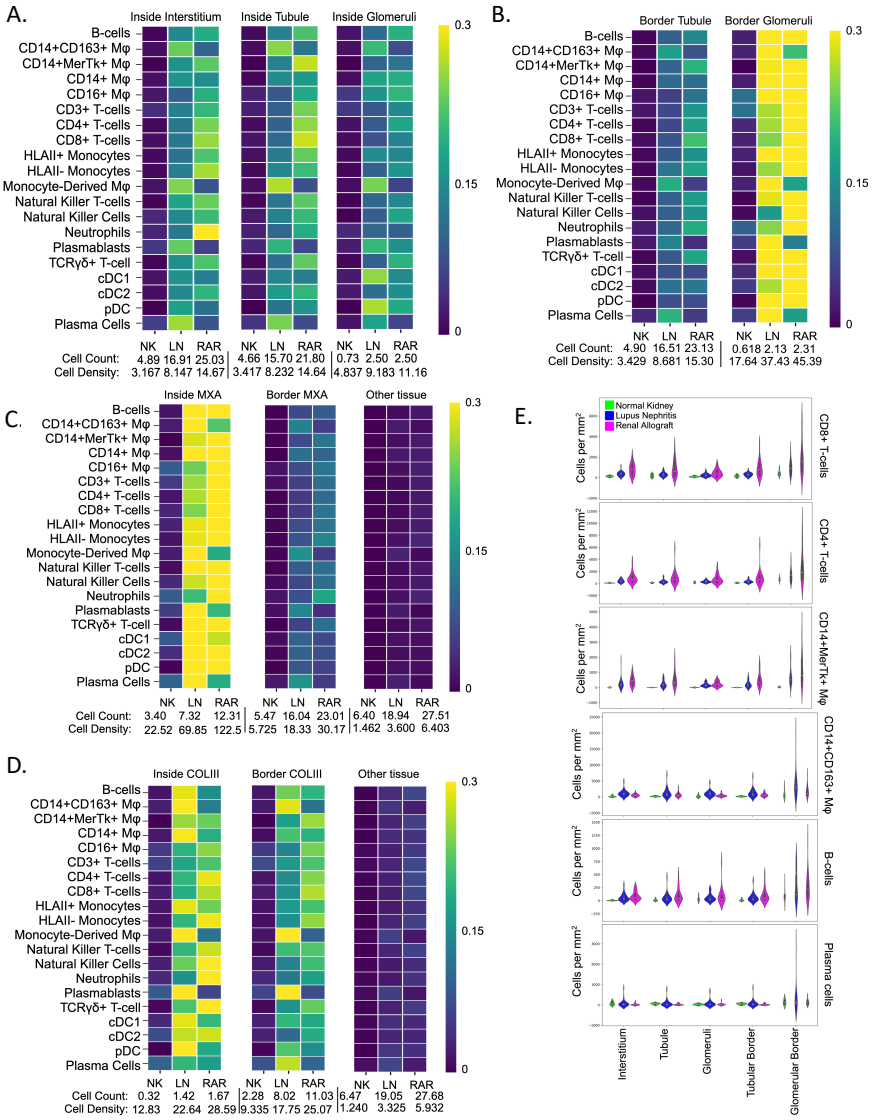

A) Heatmap showing the biopsy-average density of immune cells inside the kidney tissue compartments, normalized to proportion across cohorts: tissue interstitium (left), tubules (middle), and glomeruli (right). Bottom of heatmap shows the respective total cell count (per 10,000 cells) as well as the cell density (per 10 million pixels) for each cohort within all compartments shown. (Left column) normal kidney, (middle column) lupus nephritis, and (right column) renal allograft respectively for each heatmap. B) Heatmap showing the biopsy-average density of immune cells at the border of 2 major kidney tissue compartments, normalized to proportion across cohorts: tubules (left), and glomeruli (right). C) Heatmap showing the biopsy-average density of immune cells of the MXA mask compartments, normalized to proportion across cohorts: tubules (left), and glomeruli (right). D) Heatmap showing the biopsy-average density of immune cells of the COLIII mask compartments, normalized to proportion across cohorts: tubules (left), and glomeruli (right) E) Violin plots of the cell densities (per mm^2) of CD8+ T-cells, CD4+ T-cells, MerTk+ Mϕ, CD163+ Mϕ, B-cells, and plasma cells for interstitium, tubules, glomeruli, tubular border, and glomerular border.

CHAPTER 8

DISCUSSION

This thesis represents a pioneer investigation into the immune landscape of lupus nephritis and renal allograft rejection biopsies; providing novel insights into the pathogenic mechanisms underpinning renal autoimmunity and alloimmunity. Our expertise with CODEX microfluidics, along with our unique spinning-disk confocal microscopy system, and our innovative computational pipeline for the analysis of multiplex immunofluorescence images, has enabled us to capture the spatial features of renal immunity with unprecedented precision. This allows us to address biological questions that many other "omics" methods such as RNAsequencing are unable to investigate due to the physical limitations of the method, such as mandatory tissue dissociation. For example, our nearest-neighbor analyses, DBSCAN-neighborhood analyses, tissue compartment analyses, and mTOC polarization tool depend on spatial coordinate data. Furthermore, our ability to ascribe immune cell populations to specific kidney compartments, such as tubules or MXA high areas, is a specific advantage of spatial proteomics techniques such as CODEX.

Methods like CODEX and Imaging Mass Cytometry, have transformed the field of spatial biology and how we comprehend the cellular context in situ. These techniques allow for the extraction of an unprecedented depth of data from biopsy samples. Yet, the very complexity and volume of this data render traditional manual analysis methods impractical. In our initial High-Resolution (HR) dataset, we proposed that variations in renal outcomes might be linked to the differences in in situ adaptive immune responses, including the distribution and arrangement of key immune cells. Therefore, for the HR dataset, we stained each biopsy for 6 markers targeting the most prominent T cell lineages as well as dendritic cell subtypes: CD3, CD4, CD20, CD11c, BDCA2, and DAPI, to characterize: CD3+CD4+ T cells, CD3+CD4– T cells, CD20+ B cells, BDCA2+ pDCs, and CD11c+ mDCs. After analyzing the High-Resolution (HR) dataset, we utilized highly multiplexed (HMP) confocal

microscopy for a more detailed examination of lymphocyte populations and a more comprehensive array of cell types. To achieve this, we expanded our panel of markers beyond those used in the HR analysis, incorporating CD8, ICOS, PD1, FoxP3, CD20, CD138, and DAPI, to investigate various functional phenotypes of the immune response in kidney tissue. To gather this HMP dataset, we applied 4-color confocal microscopy, paired with techniques of iterative stripping and reprobing, to navigate past the conventional barriers of fluorescent imaging. The experience we gained with analyzing cellular imaging data using computer vision techniques was vital for our future CODEX analysis.

Cell segmentation challenges

We collected 54 archival kidney biopsy blocks preserved as formalin-fixed, paraffin embedded (FFPE) specimens. Of these, 25 blocks originated from patients with Lupus Nephritis (LN), 23 from patients experiencing Rejection After Renal transplantation (RAR), and six were classified as "normal" kidney samples. It's important to note that renal biopsies are generally reserved for cases with significant clinical or lab indications due to the invasive nature of the procedure. Therefore, the "normal" controls in this study were obtained from nephrectomy specimens from individuals without autoimmune diseases and who showed no signs of renal inflammation or damage upon histological review. In the context of LN, biopsies are undertaken not for routine surveillance but in situations where clinical or lab findings strongly suggest LN, requiring biopsy confirmation in patients with Systemic Lupus Erythematosus (SLE). Conversely, while RAR biopsies form a part of the routine surveillance for the health of organ transplants, such invasive monitoring is not practiced by the University of Chicago Medical Center.

Our LN cohort is highly heterogeneous, as evidenced by the wide range of ages at which our LN patient group received their SLE diagnoses, ranging from 10 to 61 years, with an average diagnosis age of approximately 25.75 $\pm$ years 5.38 years, plus or minus 5.38 years. Notably, these biopsies were collected on average about 4.08 years after the SLE diagnosis;

a year earlier than the average time to LN diagnosis as described in the background [10]. The different clinical contexts in biopsy acquisition are important confounding variables that we must remember when comparing our groups. For example, some residual inflammation is expected in our NK cohort given that they are nephrectomies. On the other hand, we expected our LN biopsies to be less inflamed when compared to the HR dataset since the HR dataset biopsies were collected later in terms of disease progression.

Leveraging the Lupus Nephritis (LN) Accelerating Medicines Partnership (AMP) single-cell RNA (sc-RNA) dataset, along with various studies on human in situ immune responses, we crafted and confirmed the efficacy of an antibody panel targeting 43 markers. The antibody validation performed by Junting Ai and microscopy images acquired are themselves worthy of scientific merit. Our marker panel was meticulously designed to capture a diverse spectrum of cellular phenotypes, focusing on renal cells essential for kidney function and immune cells from both innate and adaptive systems. We hope that the validated antibodies, as well as our imaging data, can help other labs study human renal immunity.

The considerable complexity of the kidney, along with its significant physiological cell diversity and immune marker variability, complicates the use of standard computer vision methods for imaging and analysis. The more novel human-in-the-loop retraining method proved instrumental in improving Cellpose's DAPI segmentation performance, particularly evident with our RAR samples. As highlighted earlier, the challenges inherent in processing RAR samples—primarily due to the ambiguous nature of nuclear structures caused by degradation in tissue quality—are a significant factor influencing this difference in performance with LN. After this HITL retraining approach is performed, Cellpose DAPI nuclear segmentation achieves a much better F1 performance score of 0.73 in RAR (+.15) and of 0.88 in LN (+.08) at an IoU threshold of 0.25 (Figure 3.6B). The average precision score had similar trends in improvement, with 0.54 in RAR (+.15) and 0.77 (+.09) in LN samples. The latter Cellpose performance metrics are approaching the upper bounds of ML and human

performance/agreement between readers. In the future, we hope that this Cellpose model can be generalized and tested on further renal diseases or non-renal tissue.

By directly involving human decision-making in the iterative process of training and refining models, HITL allows for more nuanced decision-making that purely unsupervised and supervised systems may overlook. This collaboration between model output and human expert feedback/corrections is especially pivotal in refining model predictions and mitigating the propagation of errors through continuous learning and adaptation. When we apply our HITL-trained Cellpose 2.0 model, we capture e a total of 2.19 million cells, of which 681,674 cells are from the NK samples, 784,113 cells are from the LN samples, and 724,960 cells are from RAR samples. NK samples, on average, have a greater cellularity presumably due to the healthier status of tissue and lack of fibrosis or destruction, a relatively straightforward segmentation task when compared to the highly inflamed RAR cohort. In all, these 2.19 million cells represent an unprecedented level of immune cell spatial detail, contributing to the advancement of the field.

As demonstrated in Figure 5.2B, normalizing cell frequency data by the biopsy tissue area (density) reveals significant differences in cell data, highlighting the importance of this approach in mitigating potential sampling bias. Such bias may arise from variations in tissue capture attributable to technical or logistical factors; particularly in studies where the tissue area can vary widely due to the sample collection process or issue with tissue sample quality, as in the case of the highly inflamed RAR samples. In our prior experience, we found that normalizing by ROI of capture (in HR data) or tissue area (in the HMP data) was vital for the analysis [49]. In this CODEX dataset, We observed that the highest cell count in NK samples was around 248,000 cells, compared to about 61,000 cells and approximately 67,000 cells in LN and RAR samples, respectively. However, when normalized by the area, the densities adjust to roughly 18.1, 24.9, and 23.2 cells/mm2 for NK, LN, and RAR. The NK biopsies are negative nephrectomy resections, as previously mentioned, and as such, are

physically much larger than the LN and RAR core needle biopsies. However, LN and RAR presumably have higher cell densities due to the presence of immune cell infiltrate.

Cell annotation

Multiplex microscopy imaging (MMI) with over 40 markers presents extraordinary detail from biological samples, yet this same complexity renders manual image analysis impractical. Traditional methods could require upwards of 100 man-hours for simpler image analyses, and scaling up to handle 40+ markers becomes unmanageable for manual review, far exceeding what is feasible for accurate, high-throughput analysis. Furthermore, the reliability of human-generated ground truth (GT) is constrained by significant variations in human performance, including among expert analysts [154]. In our prior work in HR and MHP research, we utilized Mask R-CNN for the simultaneous detection, segmentation, and classification of cells in microscopy images. However, for the CODEX project, we opted to separate cell detection and segmentation from cell classification. We believed that this separation would provide greater flexibility for the plug-and-use of novel segmentation or classification algorithms. Aside from this benefit, it was impractical, given our resources and time constraints, to generate cell-class-specific ground truth segmentations for 20+ cell types. Compiling accurate ground truths from 40 channels proves too challenging for manual processes, undermining the benefits of manual verification. Moreover, the extensive volume of training images required for reliable instance segmentation performance is not feasible.

The computational modeling of biological systems and the development of new computational approaches through biologic observation is not a novel concept per se. The perceptron, the precursor to the powerful and ubiquitously used neural net algorithms, is based upon the study and observation of real biological neural connections and the human visual cortex[175]. Furthermore, the popular ReLU activation function commonly employed in Neural nets was based upon the all-or-nothing behavior of neuronal action potentials[176]. Similarly, we construct our decision-tree classifier using expert domain knowledge of human immune cell

biology. In this work, I describe and use a decision-tree classifier for the multiclass (>30) annotation of renal cells; analogous to flow cytometry-based cell analyses. The well-known computer vision technique, Otsu's method [160], was used to calculate the ideal thresholds for determining cell marker positivity in images. We based our use of the multiotsu method on empirical observations in tissue; the ideal number of latent pixel population densities and threshold-stringency were selected to match manual segmentations of positive signal closely. The back-and-forth construction of the algorithmic branches, as well as spot-checking of marker positivity, is philosophically akin to human-in-the-loop model retraining due to the active and iterative human input during model construction and application. An example is the additional myeloid cell gating performed on CD45- cells since it was observed early that myeloid lineage cells have low CD45 expression kidney in tissue. Accordingly, the decision-tree algorithm was modified to capture this observed behavior.

Both multiplex fluorescence imaging and flow cytometry, traditionally used to study the human immune system, are antibody-based fluorescent assays for studying cell states. We aimed to mimic the structured and systematic categorization of immune cells often employed in analyzing proteomic fluorescence expression detected through flow cytometry [163]. Thus, our flow cytometry-analogous decision-tree approach to cell classification is familiar and interchangeable with known cell definitions; allowing for greater integration with existing immune literature. Furthermore, this cell classification approach, in theory, is an excellent way to deal with undesired background staining, as you guarantee background marker stains do not affect the classification decision as they are not factored into the decision tree's flow, we limit the feature space using domain-specific knowledge.

When we apply our classification approach, we note that the "undefined" cell class is the dominant cell class at 38.8% (250,987 cells) in NK, 24.0% (188,199 cells) in LN, and 22.0% (159,622 cells) in RAR respectively (Figure 5.2A). Our algorithm ultimately processed around 2.19 million cells, with over 72.58% assigned an interpretable phenotypic class: such

as as renal cells, T cells, myeloid cells, humoral cells, and subsets of each of those populations. Furthermore, our UMAP MFI plots showed that the expression of fluorescent markers largely corresponds with the cell classifications and gating strategies employed. For instance, the T-lymphoid cluster shows enrichment for lineage-specific markers such as CD3, CD4, and CD8, while the myeloid cluster is characterized by high levels of HLAII, CD14, and CD16, giving us the expected expression of these classes. Our undefined cell class likely represents mostly tubular cells as the marker used to categorize these cells, CD10/MUC1/Claudin1, is primarily expressed at the cell surface and is not fully captured by nuclear dilation of these large cells. By overcoming the challenges associated with manual annotation and leveraging advanced imaging and computational techniques, we provide a classification framework for the future of spatial biology research, with the potential to transform our understanding of complex diseases and improve clinical outcomes. Ultimately, our decision tree offers flexibility to modifications in the composition of the marker panel and updates in cellular definitions, and it is suitable for application to novel data collections.

We created additional UMAP plots by sampling 10,000 cells from the NK, LN, and RAR groups to investigate cell populations specific to each cohort. The balanced sampling from each cohort is key to avoid biasing our embeddings towards a particular patient population. When overlaying assigned cell classes on our UMAP plots, we find that cells embedded according to lineage similarities, display a spatial axis between immune and non-immune cells, as well as between lymphoid and myeloid cells. It is in these UMAP plots that we first saw the differential presence of immune cells in biopsy tissue. This includes a noticeable scarcity of immune cells in the NK cohort, a predominance of T-lymphoid cells in the RAR samples, and a higher presence of myeloid lineages in the LN cohort, indicating a disease-specific polarization of immune lineages. The overlapping of NK with LN and RAR cells in the non-immune territory aligns with our expectations, as all samples are derived from renal biopsies. The absence of NK cells in the immune territory is an important quality control

checkpoint, indicating their role as negative controls.

Cell frequency data

When we examine the cell count data, non-immune cells comprised 51.0% of the cell makeup in LN and 38.7% in RAR, against 53.7% in the NK cohort. Notably, in both LN and RAR cohorts, inflamed tubules were the most commonly identified cell type, comprising 17.6% (138,193 cells) and 13.2% (96,113 cells) of the cell populations, respectively. The high proportion of inflamed tubules in LN and RAR does not come as a surprise given that these are our autoimmune and alloimmune cohorts. Following inflamed tubules, the LN cohort had a high frequency of proximal tubules (109,330 cells; 13.9%), endothelial cells (87,288 cells; 11.1%), and distal collecting tubules (66,103 cells; 8.4%). In the RAR cohort, the most numerous were proximal tubules (63,629 cells; 8.7%), distal collecting tubules (62,211 cells; 8.5%), and endothelial cells (representing 8.3% of cells).

When looking at the frequencies of immune cells, we find that in LN samples, myeloid cells such as CD14+ Mϕs (34,871 cells; 4.4%) and CD14+CD163+ Mϕs (32,581 cells; 4.1%) are one of the most abundant immune cell types. The RAR cohort had a higher proportion of myeloid cells and T-cells than the NK cohort. For instance, myeloid cells like CD14+ Mϕs (41,138 cells; 5.6%), CD14+CD163+ Mϕs (18,813 cells; 2.5%), and CD14+MerTk+ Mϕs (17,802 cells; 2.4%), CD3+ T-cells (22,253 cells; 3.0%), CD4+ T-cells (16,551 cells; 2.2%), and CD8+ T-cells (14,151 cells; 1.9%). However, we find considerable heterogeneity in the immune infiltrate among patients, regardless of their cohort classification. For example, some RAR biopsies are clearly T-cell dominant, while others show an enrichment for myeloid cells. Nevertheless, we observe a consistent expansion of the myeloid cell group in LN samples, with a relatively smaller presence of T-lymphocytes, whereas RAR samples show a greater increase in T-lymphocytes compared to myeloid cells. These trends are consistent with the immune cell distribution seen on UMAP.

To statistically test for the differential abundance of these immune cells between our

cohorts, I used a WMU test using the patient-level cell densities. The use of density here is essential to correct for potentially biased sampling, as stated before. Furthermore, we use the patient-level averages versus sample-level averages to ensure statistical independence; a single patient may have more than one imaged sample. Upon comparing the disease cohorts, there was a notable increase in both myeloid and T-cell populations in the LN and RAR groups relative to the NK control. Specifically, in the LN samples CD14+CD163+MerTk+ macrophages (Mϕ), CD14+CD163+ Mϕ, CD14+MerTk+ Mϕ, HLAII+ monocytes, and CD14+ Mϕ were found to be significantly more abundant in the renal tissue compared to the NK group; suggesting a myeloid-cell predominance in this cohort. Likewise, in the RAR group, there were significant increases in the densities of CD14+CD163+MerTk+ Mϕ, CD14+MerTk+ Mϕ, and HLAII+ monocytes compared to NK; indicating a potential role of myeloid cells in driving tissue inflammation in RAR as well. Conversely, many T-cell populations such as CD4+ICOS+PD1+ T-cells, CD8+ICOS+ T-cells, Natural Killer T-cells, CD4+FoxP3+ T-cells, CD4+ICOS+ T-cells, CD4+PD1+ T-cells, CD4+ T-cells, and TCR$\gamma\delta$ T-cells were deferentially found in RAR and not NK biopsies. Enrichment of CD14+CD163+ M2 Mϕ was exclusively observed in the LN cohort. Additionally, when comparing the disease states, a notable enrichment in various T-cell lineages, alongside HLAII+ monocytes ($p < 0.01$), was seen in RAR relative to LN. For instance, increases in CD4+CD8+ T-cells ($p < 0.05$), CD4+ICOS+ T-cells ($p < 0.05$), CD4+ T-cells ($p < 0.05$), CD8+Foxp3+ T-cells ($p < 0.05$), CD8+ICOS+PD1+ T-cells, CD8+ICOS+ T-cells ($p < 0.05$), and natural killer T-cells ($p < 0.05$). From these statistical tests we start seeing cohort-specific inflammation, we see signs that a M1/M2 macrophage phenotype is predominant in LN, while the interplay between T-cells and myeloid cells is predominantly found in RAR, the latter is further confirmed by our cognate tool.

Immune cell covariance

To capture immune cell self-organization, we performed a Spearman's correlation heatmap

of patient-level cell densities and proportions. In doing so, we find that in LN there are three main "blocks" of covariant cells: 1) a T cell cluster that encompasses both CD4+ and CD8+ T-cells, 2) CD14+MerTk+ macrophages, and 3) B cells alongside CD14+CD163+ macrophages and the dendritic cells. Here we see signs that LN patients may have multiple clinical phenotypes. For example, we see an inverse correlation between the blocks comprising M2 (CD14+CD163+) and M1 (CD14+MerTk+) macrophages. In the RAR cohort, similar correlation patterns were noted, though the strengths of both positive and negative correlations were less pronounced, most likely reflecting the high heterogeneity of MR and TCMR samples and the smaller respective size of these cohorts (MR = 24, TCMR = 10) versus the joint RAR cohort (N = 24) or LN cohorts (N = 25). We expect that with a greater sample size for TCMR/MR these inflammatory trends should become more pronounced. Conversely, the NK cohort displayed no distinct trends in immune cell self-organization as expected. When we plot the patient-level densities of myeloid cells (representing innate immunity), T-lymphocytes (adaptive immunity), and humoral cells (also part of adaptive immunity), it becomes evident that the biopsies tend toward either a myeloid-dominant or T-cell-dominant phenotype. Specifically, the T-cell axis predominantly features samples from the RAR cohort, while the myeloid axis includes primarily LN samples, with some from RAR. We find that samples with the highest T-cell densities are primarily from MR cases, presumably due to a more aggressive alloimmune response in these patients. As anticipated, samples from the NK cohort are clustered near the origin, indicating minimal baseline inflammation levels.

When examining the distribution of CD163+ M2 macrophages (Mϕ) and MerTk+ M1 macrophages densities in biopsy samples, we noticed significant patient heterogeneity. In agreement with our Spearman's correlations heatmap, we observe an antagonistic relationship between these two cell populations reminiscent of the M1-M2 polarization axis. Specifically, LN biopsies tend to align along a trajectory favoring either CD14+MerTk+

M1 macrophages or CD14+CD163+ M2 macrophages, rarely showing high densities of both simultaneously. In contrast, RAR biopsies predominantly follow the M1 macrophage trajectory without significant representation of M2 macrophages. Additionally, densities of CD8+ T cells were more commonly associated with MerTk+ than CD163+ macrophages, suggesting potential functional linkages between these two. We later find no pronounced differences in M1/M2 macrophage polarity between MR and TCMR cohorts in our limited sample size, aside from a minor inclination towards CD163+ macrophages in MR cases. However, these observations pertain to global immune patterns rather than in situ local cell-cell interactions, something we were particularly interested in and employed spatial methods to capture.

We aimed to investigate the correlation between the presence of CD8+ T-cells, M2 CD163+ macrophages, and M1 MerTk+ macrophages and the levels of in situ inflammation and tissue damage. For this purpose, we defined tissue inflammation using criteria that are biologically relevant, straightforward to interpret, and applicable across various datasets; even those lacking detailed clinical or histological indicators of tissue stress. These inflammatory features are: 1) the overall density of immune cells (indicative of immune infiltration), 2) the density of inflamed tubules, 3) the extent of MXA expression within the tissue, and 4) the coverage of collagen type III (COLIII) in the tissue. Our analysis of total immune cell density revealed a significant link between CD8+ T-cell density and immune infiltration in both the LN ($p = 0.002$) and RAR cohorts ($p < 0.00001$), but not within NK controls. Moreover, the density of CD14+CD163+ M2 macrophages showed a significant association with immune infiltration exclusively in the LN group ($p = 0.006$), with no such correlation in RAR or NK patients. Similarly, examining CD14+MerTk+ M1 macrophage density concerning immune infiltration revealed statistically significant associations in both autoimmune LN ($p = 0.004$) and alloimmune RAR cohorts ($p = 0.005$), but not in the NK control group. The observed correlation between CD8+ T cells and immune cell infiltration in RAR aligns with expectations, reflecting the cytotoxic role these cells play in RAR,

a hallmark of adaptive alloimmunity. Intriguingly, the significant positive correlation seen in LN suggests the possible existence of a CD8+ T-cell inflammatory subtype within LN, beyond the noted M1/M2 macrophage polarization seen prior. Furthermore, both RAR and LN show a positive link between M1 MerTk+ macrophages and immune cell infiltration.

In our analysis of inflamed tubules, identified by diminished CD10/MUC1 expression and increased Claudin1 expression, no significant correlations with CD8+ T-cell density were found across the cohorts: NK ($\beta = 0.05$; p = 0.40), LN ($\beta = 0.01$; p = 0.68), and RAR ($\beta = 0.13$; p = 0.38). Likewise, no significant trends were detected between M2 CD163+ Mϕ density and inflamed tubules. However, a notable exception was the significant association between M1 MerTk+ macrophages and inflamed tubules exclusively in RAR ($\beta = 0.15$; p = 0.02). This association is particularly intriguing given MerTk's pivotal role in efferocytosis, the mechanism by which macrophages clear apoptotic cells. Given the significant positive link between M1 MerTk+ macrophages and inflamed tubules in RAR, we hypothesized that these M1 cells may engage with the tubules either to aid in resolving tissue inflammation or through a maladaptive efferocytosis process that contributes to tubular damage.

Utilizing MXA as an indicator of tissue inflammation, we uncovered a cohort-specific correlation within the RAR cohort, showing a significant link between CD8+ T-cell density and MXA expression ($\beta = 10.59$; p = 0.0009). The absence of a significant correlation in LN suggests that CD8+ T-cell-associated inflammation may occur independently of IFN-γ in LN samples. However, in RAR, IFN-gamma signaling, as evidenced by MXA expression, seems to correlate with cytotoxic CD8+ T-cell infiltration. This finding, particularly in the context of RAR, aligns with expectations that cytotoxic T-cells are a driving force behind alloimmune inflammation.

Using the COLIII score as a proxy for tissue inflammation was less revealing. A significant correlation was found between CD8+ T-cell density and COLIII scores exclusively in the NK control group ($\beta = 6.62$; p = 0.01). This finding in the NK controls is unexpected; however,

even though these NK biopsies were histologically classified as "negative" for inflammation, it's conceivable that there might be undetected, sub-clinical levels of immune cell infiltration not overly apparent to the naked eye. COLIII is a biomarker for various states; it can denote the structural integrity essential for organ function, indicate fibrosis or scar formation, or reflect tissue regeneration. The challenge arises from whether COLIII is maladaptive or a necessary aspect of repair; however, such repair processes can sometimes lead to further tissue damage.

Distinct in situ niches

Given the clinical significance of dense immune infiltration, we aimed to characterize these cell clusters to identify any cellular networks of immunological relevance. To achieve this, we employed the DBSCAN algorithm, a method previously utilized in our research [49], to detect these "neighborhoods" of cells within our multiplex microscopy imaging data. After conducting a bootstrapping experiment, we determined that the empirically optimal number of K-clusters falls between 9 and 11; opting for 11 as the ideal K for further analysis. Clusters 0, 5, and 8 emerged as the most biologically intriguing and most prevalent neighborhood clusters across all cohorts. Cluster 0 was characterized by a high presence of CD14+CD163+MerTk+ macrophages, CD14+CD163+ macrophages, CD3+ T-cells, CD4+ T-cells, and CD8+ T-cells. In contrast, Cluster 5 predominantly contains CD14+ macrophages and CD14+MerTk+ macrophages, along with smaller populations of monocyte-derived macrophages and CD14+CD163+ macrophages. We putatively consider Cluster 0 to depict a CD163+ M2 macrophage:T-cell network, likely facilitating antigen recognition. Meanwhile, we consider Cluster 5 to constitute an M1-like myeloid-rich cell network. The distinct compartmentalization of Clusters 0 and 5 reflects the antagonistic M1/M2 relationship observed in Spearman's correlation heatmaps and density plots figures, indicating that the global M1-M2 polarization observed in analyses is also present at the local tissue level.

Cognate immunity and a cognate tool

To investigate critical biological processes, including cell-cell interactions, cytotoxic activity, and immune recognition events, we created a computational approach capable of identifying mTOC polarity within multiplex microscopy imaging, designed to be adaptable across various datasets. In this approach, we directly utilize segmentation of the microtubule-organizing center (mTOC) and cell bodies. This approach allows us to examine mTOC polarity across a wide array cell-cell pairwise interactions without circumventing the need for human expert segmentation. We observe an increase in the absolute patient-level counts of B-cells:CD4+PD1+ T-cells and B-cells:CD4+ICOS+ T-cells polarization, specifically within the MR cohort. This finding is significant as it corroborates previous research linking cognate interactions between these cells to MR. Upon conducting a Wilcoxon-Mann-Whitney (WMU) test using cognate cell , we identified a statistically significant elevation in the polarization of B-cells towards CD4+PD1+ T-cells when comparing the RAR and NK cohorts ($p = 0.009$), and for B-cells towards CD4+ICOS+ T-cells when comparing RAR to NK ($p = 0.04$) and RAR to LN ($p = 0.01$), further substantiating these observations. In this analysis, we observed a statistically significant increase in CD14+MerTk+ macrophages:CD8+ T-cell polarization comparing ln to NK ($p = 0.02$), RAR to NK ($p = 0.003$), and RAR to LN ($p = 0.004$). Similarly, we find a significant enrichment of CD14+MerTk+ macrophages:CD4+ T-cells polarization when comparing NK to LN ($p = 0.006$), NK to RAR ($p = 0.0009$), and LN to RAR ($p = 0.009$). For CD163+ macrophages, significant increases in polarization towards CD8+ T-cells were found between NK and LN ($p = 0.009$), and NK and RAR ($p = 0.009$); and towards CD4+ T-cells between NK and LN ($p = 0.03$), and NK and RAR ($p = 0.03$). These findings would suggest that T-cell-mediated inflammatory activity plays a crucial role in RAR. This mTOC polarity detection algorithm is can be viewed as an additional method for spatial feature extraction, leveraging spatial data to infer cell-cell interaction levels.

Creating and applying our computational tool for detecting mTOC polarity in MMI

represents an innovative, biology-driven way to quantify spatial immunity. The direct use of cell segmentations and mTOC makes this algorithm compatible with the other pipelines, expanding the accessibility of this tool to MMI methods other than CODEX. We correctly hypothesized that there should be a higher amount of mTOC polarity between immune cells in the alloimmune (and to a lesser extent autoimmune) cohorts due to these samples' high immune activity and inflammation. Notably, the distinct patterns of T-cell interactions observed in RAR samples reinforce the notion of T-cells as pivotal actors in allograft rejection, aligning with our understanding of T-cell-mediated cytotoxicity in transplant pathology.

In the context of immune responses, microtubule organizing centers (MTOCs) play a critical role in directing the polarity of immune cells, thereby influencing their interaction with target cells. In alloimmune responses, such as renal allograft rejection, the immune system recognizes the transplanted kidney as foreign, triggering a robust immune response to donor alloantigens. MTOCs within immune cells, especially T cells, are reoriented towards the APCs or target cells of the donor tissue, facilitating precise delivery of cytotoxic agents or in activating immune cells through the TCR. In contrast, in the context an autoimmune condition like LN, the role of B-cell autoantibodies is pivotal. These autoantibodies are produced by autoreactive B cells that mistakenly recognize self-antigens as targets. In LN, these autoantibodies predominantly target nuclear antigens, forming immune complexes that deposit in the renal glomeruli, leading to inflammation and tissue damage. This B-cell driven process, however, occurs independently of mTOC polarization in situ. In alloimmune responses such as renal allograft rejection, the clear and robust antigenic distinction prompts a strong and directed immune cell response, where MTOCs actively polarize toward the donor tissue. However, in LN, despite the presence of autoantigens and the formation of immune complexes, the internal antigens recognized by autoantibodies do not provide the same polarization cues as seen in alloimmune contexts. The self antigens in LN may not trigger as strong and directional a movement of mTOCs within immune cells, particularly

because these antigens are more diffuse and systemic rather than localized and distinct as in allograft tissues.

Renal structures

Following the observation that CD163+ and MerTk+ macrophages compartmentalized, we shifted our focus on examining their abundance within specific anatomical areas: 1) the tissue interstitium, 2) the tubular border, 3) the glomerular border, 4) within tubules, and 5) inside glomeruli. Additionally, we considered areas with high MXA expression and high COLIII deposition as distinct "compartments" of biological interest, representing zones of intense interferon-driven inflammation and significant fibrosis, respectively. This compartment analysis leverages the unique capabilities of highly multiplexed imaging, allowing for an unprecedented exploration of immune cells within these critical renal areas. Upon analyzing our structural masks, we found that the area around the glomeruli (the periglomerular area) harbors the highest concentration and density of immune cells in both the RAR and LN cohorts, with densities of 37.43 and 45.39 cells per mm^2, respectively. This periglomerular infiltrate has been reported in LN biopsies before [28]. An analysis within the MXA-defined regions further underscored that this marker effectively identifies zones of high inflammation in both LN and RAR cohorts, suggesting that MXA-based masking can precisely target areas of active inflammation for prognostic significance or further study, such as texture-based feature extraction in multiplex microscopy imaging (MMI). Conversely, the COLIII mask did not demonstrate the same accuracy in pinpointing high-density immune cell regions; this is consistent with the expected cell sparsity in fibrotic areas as well as insignificant trends observed in the cell density plots.

To delve deeper into these compartmentalized immune responses, we generated violin plots illustrating the patient-level average immune cell count per mm^2, focusing on key immune cells like CD8+ and CD4+ T-cells, CD14+CD163+ M2 macrophages, CD14+MerTk+ M1 macrophages, B-cells, and plasma cells. Notably, Lupus Nephritis/Systemic Lupus Ery-

thematosus (LN/SLE) is traditionally associated with B-cell pathology. Our findings revealed a remarkably high heterogeneity of CD8+ and CD4+ T-cells within RAR's renal compartments. We observed a diverse presence of CD14+MerTk+ macrophages across the interstitium, tubules, and tubular borders in RAR samples, whereas this population was predominantly found in the interstitium and glomerular border in LN. The heterogeneity in CD14+CD163+ macrophage density within LN suggests these cells may contribute to tubulointerstitial inflammation. Again, the glomerular border consistently showed the highest immune cell density. The high variance in cell densities observed may result from non-inflamed tissue masking signals from areas with intense inflammation.

Our findings highlight the complex interplay between various immune cell populations in the kidney, underscoring the potential of spatial feature analysis as a diagnostic and prognostic tool. The phenotypic polarisation of our biopsies between T-lymphocyte dominant and myeloid dominant forms of autoimmunity highlights the vastly distinct pathologic mechanisms that can drive renal autoimmunity. We find that while in LN, pathogenicity may be predominantly mediated by the myeloid compartment, RAR showcases a more T-cell-centric disease. Interestingly, LN biopsies did not have a high amount of either B-cells, plasma cells, or plasmablasts despite SLE being thought of as a B-cell mediated disease; this is most likely because these clinical biopsies are at a very early stage of LN disease progression and have not reached high levels of inflammation that we've previously captured. We ascribe these observed differences to the vastly different induction mechanisms between both diseases; a systemic disorder arises due to the loss of self-tolerance in LN and an organ-specific graft rejection due to a highly invasive medical intervention. The observed heterogeneity between CD14+CD163+ macrophages and CD14+MerTk+ macrophages and the compartmentalization, at both micro and macro scales, suggests a role in disease pathogenesis, echoing the sentiments of existing literature that points to macrophages as drivers of inflammation, antigen-presentation, and tissue remodeling.

The strategic use of spatial proxies for tissue inflammation, such as total immune cell infiltration and MXA mask, paves the way for novel insights into human disease research, independent of the breadth of available clinical data. This approach is especially useful for biopsies with limited clinical information, allowing for a more inclusive analysis. Our renal compartment analysis shows compartment-specific immune dynamics, offering an intricate view of how immune cells orchestrate their response in different microenvironments. The differential distribution of specific macrophage populations and high heterogeneity in interstitial versus tubular regions underscores the roles of macrophages in renal pathology.

Differences in niches between LN and RAR

In LN, we observe 3 main phenotypes, a CD14+CD163+ M2 Mϕ-enriched phenotype, a CD14+MerTK+ M1 Mϕ-enriched phenotype, and signs of a T-cell-enriched phenotype. CD14+CD163+ is associated with increased immune cell density and is enriched in the COL-III mask and insterstitium particularly. On the other hand, CD14+MerTk+ cell density is significantly associated with immune cell density and COLIII score. Since CD163+ cells are more enriched in the interstitium and COLIII masks, but not the tubules and glomeruli or MXA mask, and given the inflammation trends, we suspect these cells are being recruited to either promote tissue scarification and collagen deposition, or at an attempt to repair tissue damage. On the other hand, CD14+MerTk+ Mϕ's inflammation trends and presence, particularly in the tubules and MXA mask and not the interstitium/COLIII support their pro-inflammatory phagocytic role leading to tubular damage. The relative lack of T-cell mTOC polarity, inflammation trends and reduced co-occurrence leads us to suspect inflammation here through CD14+MerTk+ cells is mostly T-cell independent, unlike in RAR.

In the context of RAR, while CD14+MerTk+ macrophages are involved in phagocytosis their covariance and interaction with CD8+ T-cells, as quantified using our cognate/mTOC tool, suggests a possible pathogenic positive loop, whereby these cells promote local inflammation jointly. This interaction is not merely coincidental but rather indicative of a func-

tional nexus that may exacerbate inflammatory responses. Further insight into this complex cellular interaction is provided by the upregulation of the activation marker CD27 within the T-cell population, along with increased expression of granzymes (GZMA, GZMB, GZMK) within the cytotoxic T-cell lineage. These molecular markers of activation not only signify an enhanced state of immune responsiveness but also suggest an aggressive cytotoxic response aimed at pathogen clearance or tissue remodeling. The observed spatial co-occurrence of CD14+MerTk+ macrophages and CD8+ T-cells, along with trends indicating microtubule-organizing center (mTOC) polarity, further supports the notion of a coordinated inflammatory response. This spatial arrangement is likely critical for effective antigen presentation, a key process in T-cell activation and subsequent immune response modulation. The proximity of these cell types facilitates efficient communication and antigen exchange, potentiating the T-cell response and likely influencing disease trajectory. This complex cellular choreography, mediated through antigen presentation, is instrumental in driving the inflammatory processes observed in RAR. Understanding these dynamics at a deeper molecular and cellular level could unveil new therapeutic targets and strategies for managing RAR-associated conditions, highlighting the need for further detailed studies in this area. The summary model emphasizes the importance of understanding cell relationships in situ and their contributions to disease pathogenesis. This data highlights the potential for MerTk+ macrophages in directly driving tissue inflammation and for CD163+ macrophages to indirectly drive damage through collagen deposition particularly in LN, and suggests a collaborative role of MerTk+ macrophages and CD8+ T-cells in driving inflammation in RAR (Figure 8.1).

Implications of MerTK+ macrophages

A very recent study by Ziyan ey al. identifies MERTK as a profibrotic kinase that is upregulated in various models of fibrosis in mice and in humans [177]. TGFβ is shown to stimulate an increase in MerTk expression in fibroblasts and macrophages, which in turn enhances profibrotic ERK/AKT and SMAD signaling pathways. MerTk functions downstream

of TGFβ and participates in a positive feedback loop that enhances fibrotic signaling in both human and mouse cells. In mouse models of fibrosis affecting the liver, kidney, and lungs, the genetic removal of Mertk successfully prevented fibrotic development. Additionally, a pharmacological inhibitor of MerTk was effective in reducing fibrosis in these models as well as in another mouse model of liver fibrosis. These observations indicate that inhibiting MerTk could be a viable strategy for treating fibrosis. In RAR, MerTk is notably associated with T-cells, the presence of MerTk+ macrophages in T-cells may enhance the inflammatory and fibrotic pathways critical to the rejection process, potentially through the activation of profibrotic signaling cascades like those mediated by TGFβ. The absence of a clear association with T-cells in LN might suggest that MerTk+ macrophages functions in concert through different cell types or signaling pathways, possibly influencing the severity and progression of fibrosis in a manner unique to autoimmune kidney damage. We believe that MerTk+ macrophages may behave in a fundamentally different way in driving inflammation in LN and RAR; we qualitatively observe a more interstitial distribution of MerTk+ cells in LN versus a tubule in-migration in RAR. A representative example of CD14+MerTk+ macrophage interstitial inflammation in LN and CD14+MerTk+ macrophage tubulitis in RAR is shown in Figure 8.1D. This observed difference may be due to the autoimmune versus alloimmune nature of renal tissue injury in LN and RAR respectively.

Potential roles of cytotoxic T cells in RAR

The role of T lymphocytes in kidney transplantation has been extensively studied, particularly focusing on various subpopulations of CD4+ lymphocytes [178]. However, relatively few studies have explored the impact of CD8+ T cytotoxic T-cells (CTLs) in renal transplantation and their potentially harmful effects on the longevity of the allograft. Recently, there has been a resurgence of interest in the involvement of CD8+ T cells within the field of transplantation. The role of CD8+ T cells in the rejection response following allorecognition is underscored by findings that the CD8+ T cell population exhibits greater resistance to im-

munotherapy and tolerance induction protocols than CD4+ T cells [178, 179]. Furthermore, a pronounced localized accumulation of CD8+ lymphocytes characterizes allograft rejection in recipients, where this subset of T cells evading immunosuppression, actively contributes to rejection episodes [180, 178]. CTLs are key players in the alloimmune destruction of the parenchymal cells in kidney transplants. Rejection is driven by a specific class I reaction of T lymphocytes, necessitating CD8+ involvement for cytolysis and the release of interferon IFN-γ, perforin, and granzyme A and B. However, perforins are not essential for inducing rejection, which can be entirely driven by IFN-γ production. This would align with our significant association found only in RAR between tissue CD8+ T-cell density and total MXA score. IFN-γ production promotes the presentation of alloantigens on target tissues and facilitates the recruitment of nonspecific effector cells such as macrophages and NK cells within the graft [180].

The graft outcome has long been hypothesized to hinge on the balance between regulatory and cytotoxic molecules within renal allografts [178]. TCMR is marked by a predominant number of CTLs compared to Foxp3+ Treg cells, unlike in normal grafts. Higher levels of CTL infiltration correlate with decreased allograft survival [181], and the extent of granzyme B expression is linked to the severity of the rejection process [182]. Recent findings suggest that T cell infiltrates in transplant recipients with borderline changes typically exhibit both cytotoxic and regulatory T cells. However, the ratio in these cases tends to favor regulatory/tolerogenic markers over cytotoxic molecules [183]. Consequently, the impact of CTL infiltrates in renal transplant recipients with borderline changes appears to be diminished by the dominance of regulatory T cells. This predominance may partly explain why many of these patients, even in the absence of specific treatment, do not undergo clinical acute rejection episodes [184]. Tregs play a crucial role in fostering tolerance by inhibiting naive T cell responses and averting allograft rejection. Studies conducted both in vivo and in vitro have shown that the apoptosis of allospecific memory CD8+ T cells is markedly increased

when exposed to antigen-activated Treg cells. This suppression is closely linked to enhanced apoptosis of allospecific memory CD8+ T cells within the graft and primarily relies on the presence of the CD30 molecule on Tregs [178, 185].

8.1 Final remarks

In conclusion, this study has unearthed a wealth of spatial immunological data that advances our understanding of renal autoimmunity. CD14+CD163+ Mϕ, CD14+MerTk+ Mϕ, and CD8+ T-cells have a significant amount of data suggesting these immune populations play a central and active in situ role in renal autoimmunity and alloimmunity; exciting for future study in their use as biomarkers or targets for cellular therapies. The distinctive spatial signatures of LN and RAR not only reflect the diversity of immune responses but also bear significant implications for the development of future studies and autoimmune therapies. Our insights into the spatial features of immune cells serve as a testament to the potential of computational imaging in transforming the landscape of human disease research. Building upon our findings, future investigations are imperative to harness the full therapeutic potential such a detailed spatial analysis promises. As we continue to unravel the complex tapestry of immune cell interactions and their clinical correlates, we edge closer to the prospect of precision medicine in autoimmune renal diseases tailored to the unique immunological fingerprint of each individual. In the interest of scientific progress, collaboration, and transparency, all novel imaging data, both raw and processed files will be made publicly available in the near future when this work is in press in a major scientific journal. Accordingly, all relevant code will be made publicly available on the lab's/project's Github page after said publishing.

Figure 8.1: Cell model and example tissue distribution

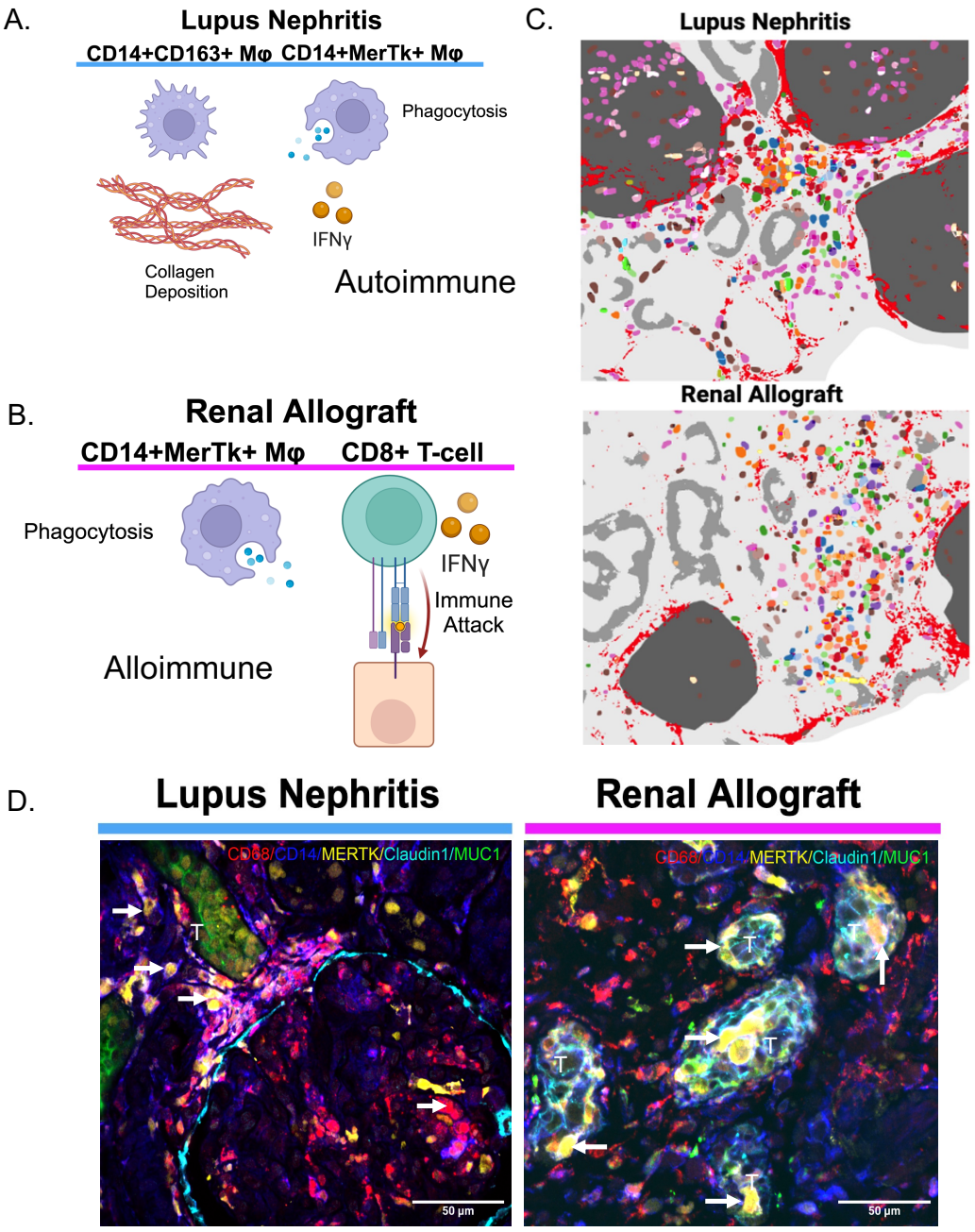

A) example inflammatory model for LN showing the interplay between M1 (MerTk+) and M2 (CD163+) macrophages B) example inflammatory model for RAR showing the interplay between M1 (MerTk+) and T-cells C) (top) computational rendering of myeloid-rich periglomerular infiltrate in LN. (bottom) computational rendering of tubulointerstitial T-cell rich infiltrate in a RAR biopsy. D) Representative example of CD14+MerTk+ macrophage interstitial inflammation in LN (left) and CD14+MerTk+ macrophage tubulitis in RAR.

REFERENCES

[1] Dörner; Thomas. Novel paradigms in systemic lupus erythematosus. 393:2344–2358, 2019.

[2] Marion; Tony. Chance, genetics, and the heterogeneity of disease and pathogenesis in systemic lupus erythematosus. 36:495–517, 2014.

[3] Arriens; Cristina. Systemic lupus erythematosus biomarkers: the challenging quest. 56:i32–i45, 2017.

[4] Hanley; John. The frequency and outcome of lupus nephritis: results from an international inception cohort study. 55:252–262, 2016.

[5] Sánchez-Escuredo; Ana. Economic analysis of the treatment of end-stage renal disease treatment: living-donor kidney transplantation versus hemodialysis. 47:30–33, 2015.

[6] Wang; Virginia. The economic burden of chronic kidney disease and end-stage renal disease. 36:319–330, 2016.

[7] Izmirly; Peter. Prevalence of systemic lupus erythematosus in the united states: estimates from a meta-analysis of the centers for disease control and prevention national lupus registries. 73:991–996, 2021.

[8] Feldman; Candace. Epidemiology and sociodemographics of systemic lupus erythematosus and lupus nephritis among us adults with medicaid coverage. 65:753–763, 2013.

[9] Korbet; Stephen. Severe lupus nephritis: racial differences in presentation and outcome. 18:244–254, 2007.

[10] Anders; Hans-Joachim. Lupus nephritis. Jan 23:6(1):7, 2020.

[11] Rother; Nils. Disturbed t cell signaling and altered th17 and regulatory t cell subsets in the pathogenesis of systemic lupus erythematosus. 6:610, 2015.

[12] Kuo; Chang-Fu. Familial aggregation of systemic lupus erythematosus and coaggregation of autoimmune diseases in affected families. 175:1518–1526, 2015.

[13] Holborow; EJ. A serum factor in lupus erythematosus with affinity for tissue nuclei. 2(5047):732–734, 1957.

[14] Canny; Susan. B cells in systemic lupus erythematosus: from disease mechanisms to targeted therapies. 47(3):395–413, 2021.

[15] Aringer; Martin. Classifying and diagnosing systemic lupus erythematosus in the 21st century. 5;59(Suppl5):v4–v11, 2020.

[16] Arazi; Arnon. The immune cell landscape in kidneys of patients with lupus nephritis. 20:902–914, 2019.

[17] Lech; Maciej. The pathogenesis of lupus nephritis. 24:1357–1366, 2013.

[18] Wise; Leanna. Belimumab and rituximab in systemic lupus erythematosus: a tale of two b cell-targeting agents. 7:303, 2020.

[19] Furie; Richard. Two-year, randomized, controlled trial of belimumab in lupus nephritis. 393:1117–1128, 2020.

[20] Bajema; Ingeborg. Revision of the international society of nephrology / renal pathology society classification for lupus: clarification of definitions, and modified national institutes of health activity and chronicity indices. 93:789–796, 2018.

[21] Chang; Anthony. Cellular aspects of the pathogenesis of lupus nephritis. Mar 1;33(2):197–204, 2021.

[22] Alexander; Tobias. The proteasome inhibitior bortezomib depletes plasma cells and ameliorates clinical manifestations of refractory systemic lupus erythematosus. 74:1474–1478, 2015.

[23] Kegerreis; Brian. Genomic identification of low-density granulocytes and analysis of their role in the pathogenesis of systemic lupus erythematosus. 202(11):3309–17, 2019.

[24] Jourde-Chiche; Noémie. Modular transcriptional repertoire analyses identify a blood neutrophil signature as a candidate biomarker for lupus nephritis. 56:477–487, 2017.

[25] Liarski; Vladimir. Cell distance mapping identifies functional t follicular helper cells in inflamed human renal tissue. 6:230ra46, 2014.

[26] Liarski; Vladimir. Quantifying in situ adaptive immune cell cognate interactions in humans. 20:503–513, 2019.

[27] Chang; Anthony. In situ b cell-mediated immune responses and tubulointerstitial inflammation in human lupus nephritis. 186:1849–1860, 2011.

[28] Couzi; Lionel. Predominance of cd8+ t lymphocytes among periglomerular infiltrating cells and link to the prognosis of class iii and class iv lupus nephritis. 56:2362–2370, 2007.

[29] Winchester; Robert. Immunologic characteristics of intrarenal t cells: trafficking of expanded cd8+ t cell -chain clonotypes in progressive lupus nephritis. 64:1589–1600, 2012.

[30] Wiechmann; Anika. Cd107a+ (lamp-1) cytotoxic cd8+ t-cells in lupus nephritis patients. 8:556776, 2021.

[31] Żabińska; Marcelina. Cd3(+)cd8(+)cd28(-) t lymphocytes in patients with lupus nephritis. 2016:1058165, 2016.

[32] Kinloch; Andrew. Anti-vimentin antibodies: a unique antibody class associated with therapy-resistant lupus nephritis. 29(6):569–77, 2020.

[33] Schürch; Christian. Coordinated cellular neighborhoods orchestrate antitumoral immunity at the colorectal cancer invasive front. 182:1341–1359.e19, 2020.

[34] Keren; Leeat. A structured tumor-immune microenvironment in triple negative breast cancer revealed by multiplexed ion beam imaging. 174:1373–1387.e19, 2018.

[35] Maningding; Ernest. Racial and ethnic differences in the prevalence and time to onset of manifestations of systemic lupus erythematosus: the california lupus surveillance project. 2020.

[36] Stojan; George. Epidemiology of systemic lupus erythematosus: an update. 30:144–150, 2018.

[37] Croca; Sara. Assessment of a lupus nephritis cohort over a 30-year period. Aug;50(8):1424–30, 2011.

[38] Mok; Chi Chiu. Understanding lupus nephritis: diagnosis, management, and treatment options. 4:213–222, 2012.

[39] Font; Joseph. Silent renal disease in systemic lupus erythematosus. 27:283–288, 1987.

[40] Bihl; Geoffrey. Kidney biopsy in lupus nephritis: look before you leap. 21:1749–1752, 2006.

[41] Zickert; Agneta. Role of early repeated renal biopsies in lupus nephritis. 1:e000018, 2014.

[42] Isenberg; David. Influence of race/ethnicity on response to lupus nephritis treatment: the alms study. Jan;49(1):128–40, 2010.

[43] Ioannidis; john. Remission, relapse, and re-remission of proliferative lupus nephritis treated with cyclophosphamide. 57:258, 2000.

[44] Lee; Senq-J. The role of antimalarial agents in the treatment of sle and lupus nephritis. 7:718–729, 2011.

[45] Hsieh; Wan-Chen. Spatial multi-omics analyses of the tumor immune microenvironment. Nov 14;29(1):96, 2022.

[46] Williams; Cameron. An introduction to spatial transcriptomics for biomedical research. Jun 27;14(1):68, 2022.

[47] Fu; Tong. Spatial architecture of the immune microenvironment orchestrates tumor immunity and therapeutic response. 25;14(1):98, 2021.

[48] Bonaguro; Lorenzo. A guide to systems-level immunomics. 23:1412–1423, 2022.

[49] Abraham; Rebecca. Specific in situ inflammatory states associate with progression to renal failure in lupus nephritis. Jul 1;132(13):e155350, 2022.

[50] Schubert; Erich. Dbscan revisited. 42:1–21, 2017.

[51] Jeanmougin; Marine. Should we abandon the t-test in the analysis of gene expression microarray data: a comparison of variance modeling strategies. Sep 3;5(9):e12336, 2010.

[52] Rosser; Elizabeth. Regulatory b cells: origin, phenotype, and function. 42(4):607–6, 2015.

[53] Fassbinder; Till. Differential effects of cyclophosphamide and mycophenolate in patients with systemic lupus erythematosus. 17(1):92, 2015.

[54] Tilney; Nicholas. Transplant: from myth to reality. 2003.

[55] Doyle; Alden. Organ transplantation: halfway through the first century. 15(12):p:2965–2971, 2004.

[56] Carrel; Alexis. Results of the transplantation of blood vessels, organs and limbs. JAMA 250 reprint:944–953, 1908.

[57] Oweira; Hani. Risk factors of rejection in renal transplant recipients: a narrative review. 11:1392, 2022.

[58] Lemoine; Mathilde. Risk factors for early graft failure and death after kidney transplantation in recipients older than 70 years. 4:656–666, 2019.

[59] Cheung; Chi Yuen. Personalized immunosuppression after kidney transplantation. Jun;27(6):475–483, 2022.

[60] Jeong; Hyeon Joo. Diagnosis of renal transplant rejection: banff classification and beyond. Mar 31;39(1):17–31, 2020.

[61] Lai; Xingqiang. Tackling chronic kidney transplant rejection: challenges and promises. 12:661643:10.3389/fimmu.2021.661643, 2021.

[62] Solez; Kim. International standardization of criteria for the histologic diagnosis of renal allograft rejection: the banff working classification of kidney transplant pathology. 44:411–422, 1993.

[63] Naesens; Maarten. Precision transplant medicine: biomarkers to the rescue. 29:24–34, 2018.

[64] Hara; Shigeo. Current pathological perspectives on chronic rejection in renal allografts. 21:943–51, 2017.

[65] Steinberg; Elizabeth. Adherence in pediatric kidney transplant recipients: solutions for the system. 33:361–372, 2018.

[66] Akoh; Jacob. Renal transplantation from elderly living donors. 2013:2013, 2013.

[67] Zeier; Martin. The effect of donor gender on graft survival. 13:2570–2576, 2002.

[68] Hiramitsu; Takahisa. Adult living-donor kidney transplantation, donor age, and donor–recipient age. 6:3026–3034, 2021.

[69] Rouchi; Alireza. When is transplantation with a "marginal kidney" justifiable? 21:463–468, 2016.

[70] Song; G. Abo-incompatible adult living donor liver transplantation under the desensitization protocol with rituximab. 16:157–170, 2016.

[71] Danger; Richard. Cxcr5+ pd1+ icos+ circulating t follicular helpers are associated with de novo donor-specific antibodies after renal transplantation. International Reviews of Cell and Molecular Biology:2071, 2019.

[72] Dharnidharka; Vikas. Kidney transplant results in children: progress made, but blacks lag behind. 87:492–494, 2015.

[73] Mehrabi; Arianeb. Surgical outcomes after pediatric kidney transplantation at the university of heidelberg. 15:221.e1–221.e8, 2019.

[74] Pratschke; Johann. Immunological risk assessment: The key to individualized immunosuppression after kidney transplantation. 30:77–84, 2016.

[75] Mehrabi; Arianeb. Long-term follow-up of kidney transplant recipients with polycystic kidney disease. 13:413–420, 2015.

[76] Salvadori; Maurizio. Renal transplant allocation criteria, desensitization strategies and immunosuppressive therapy in retransplant renal patients. 25:890, 2012.

[77] Kalogeris; Theodore. Cell biology of ischemia/reperfusion injury. 298:229–317, 2012.

[78] Kulu; Yakup. Impact of surgeon's experience on vascular and haemorrhagic complications after kidney transplantation. 57:139–149, 2019.

[79] Curci; Claudia. Potential role of effector memory t cells in chronic t cell-mediated kidney graft rejection. 31:2131–42, 2016.

[80] Benichou; Gilles. Role of memory t cells in allograft rejection and tolerance. 8:170, 2017.

[81] Bestard; Oriol. Intragraft regulatory t cells in protocol biopsies retain foxp3 demethylation and are protective biomarkers for kidney graft outcome. 11:2162–72, 2011.

[82] Boer; Karin. Variations in dna methylation of interferon gamma and programmed death 1 in allograft rejection after kidney transplantation. 8:116, 2016.

[83] Mayer; Katharina. New concepts in chronic antibody-mediated kidney allograft rejection: prevention and treatment. Feb 1;26(1):97–105, 2021.

[84] Reese; Shannon. B-cell deficiency attenuates transplant glomerulopathy in a rat model of chronic active antibody-mediated rejection. Jul 1;105(7):1516–1529, 2021.

[85] Ge; Shili. Imlifidase inhibits hla antibody-mediated nk cell activation and antibody-dependent cell-mediated cytotoxicity (adcc) in vitro. 104:1574– 9, 2020.

[86] Sellarés; J. Molecular diagnosis of antibody-mediated rejection in human kidney transplants. 13:971–983, 2013.

[87] Yazdani; Saleh. Natural killer cell infiltration is discriminative for antibody-mediated rejection and predicts outcome after kidney transplantation. 95:188–98, 2019.

[88] Sartelet; Hervé. Sirolimus-induced thrombotic microangiopathy is associated with decreased expression of vascular endothelial growth factor in kidneys. 5:2441–2447, 2005.

[89] Tsuji; Takahiro. Preceding t-cell-mediated cejection is associated with the development of chronic active antibody-mediated rejection by de novo donor-dpecific antibody. 144:13–7, 2020.

[90] Sablik; Kasia. Immune cell infiltrate in chronic-active antibody-mediated rejection. 10:3106:10.3389/fimmu.2019.03106, 2019.

[91] Jordan; Stanley. The role of novel therapeutic approaches for prevention of allosensitization and antibody-mediated rejection. 20(Suppl 4):42–56, 2020.

[92] Wojciechowski; David. Long-term immunosuppression management: opportunities and uncertainties. 16:1264–1271, 2021.

[93] Bowman; Lyndsey. The role of tacrolimus in renal transplantation. 9:635–643, 2008.

[94] Shrestha; Badri. Two decades of tacrolimus in renal transplant: Basic science and clinical evidences. 15:1–9, 2017.

[95] Rommelaere; Marie. Disseminated varicella zoster virus infection in adult renal transplant recipients: outcome and risk factors. page 2814–2817, 2012.

[96] Black; Sarah. Codex multiplexed tissue imaging with dna-conjugated antibodies. 16:3802–3835, 2021.

[97] Arazi; Arnon. Accelerating medicines partnership in sle network. the immune cell landscape in kidneys of patients with lupus nephritis. Jul;20(7):902–914, 2019.

[98] Langner; Cord. Cd10 is a diagnostic and prognostic marker in renal malignancies. 45:460–467, 2004.

[99] Lertkiatmongkol; Panida. Endothelial functions of platelet/endothelial cell adhesion molecule-1 (cd31). May;23(3):253–9, 2016.

[100] Chor; Chor ho. Claudins in kidney health and disease. 41(3):275–287, 2022.

[101] Yu; Alan. Claudins and the kidney. 26(1):11–9, 2015.

[102] Voskoboinik; Ilia. Perforin and granzymes: function, dysfunction and human pathology. Jun;15(6):388–400, 2015.

[103] Yokosuka; Tadashi. The immunological synapse, tcr microclusters, and t cell activation. 340:81–107, 2010.

[104] Allenspach; Eric. Erm-dependent movement of cd43 defines a novel protein complex distal to the immunological synapse. 15:739–750, 2001.

[105] Liu; Wenping. Ifn-, should not be ignored in sle. Aug 10;13:954706, 2022.

[106] Haller; Otto. Human mxa protein: an interferon-induced dynamin-like gtpase with broad antiviral activity. Jan;31(1):79–87, 2011.

[107] Nielsen; Mette Juul. Collagen type 3. 114:21–27, 2014.

[108] Scholzen; Thomas. The ki-67 protein: from the known and the unknown. Mar;182(3):311–22, 2000.

[109] Al Barashdi; Maryam. Protein tyrosine phosphatase receptor type c (ptprc or cd45). Sep;74(9):548–552, 2021.

[110] Choo: Sung Yoon. The hla system: genetics, immunology, clinical testing, and clinical implications. Feb 28;48(1):11–23, 2007.

[111] Dendrou; Calliope. Hla variation and disease. 18:325–339, 2018.

[112] Mir: Manzoor Ahmad. Introduction to costimulation and costimulatory molecules. Developing Costimulatory Molecules for Immunotherapy of Diseases:1–43, 2015.

[113] Szabo; Peter. Location, location, location: Tissue resident memory t cells in mice and humans. Apr 5;4(34):eaas9673, 2019.

[114] Gorabi; Armita. The pivotal role of cd69 in autoimmunity. Jul;111:102453, 2020.

[115] Morath; Anna. and t cell receptors: similar but different. Volume 107, Issue 6, June:1045–1055, 2020.

[116] Wu; Zhiheng. Cd3+cd4-cd8- (double-negative) t cells in inflammation, immune disorders and cancer. Feb 10;13:816005, 2022.

[117] Hall; Jason. Transcription factor ror enforces stability of the th17 cell effector program by binding to a rorc cis-regulatory element. Nov 8;55(11):2027–2043.e9., 2022.

[118] Standiford: Theodore. Interleukins: Il-10. Encyclopedia of Respiratory Medicine:373–377, 2006.

[119] Devaud; Christel. Foxp3 expression in t regulatory cells and other cell lineages. 63:869–876, 2014.

[120] Bao; Katherine. The differential expression of il-4 and il-13 and its impact on type-2 immunity. 75 (1):25–37, 2015.

[121] Edner; Natalie. Targeting co-stimulatory molecules in autoimmune disease. 19:860–883, 2020.

[122] Rezayi; Mahdi. Structure of pd1 and its mechanism in the treatment of autoimmune diseases. Jul 20.:10.1002/cbf.3827, 2023.

[123] Kapellos; Theodore. Human monocyte subsets and phenotypes in major chronic inflammatory diseases. Aug 30;10:2035:10.3389/fimmu.2019.02035., 2019.

[124] Sahu; Ranjit. Structure and function of renal macrophages and dendritic cells from lupus-prone mice. 66 (6):1596–1607, 2014.

[125] Davidson; Anne. Renal mononuclear phagocytes in lupus nephritis. Jul;3(7):442–450, 2021.

[126] Xue; Qingjie. Regulation of inos on immune cells and its role in diseases. Nov 29;19(12):3805:0.3390/ijms19123805, 2018.

[127] Skytthe; Maria. Targeting of cd163+ macrophages in inflammatory and malignant diseases. Jul 31;21(15):5497:10.3390/ijms21155497, 2020.

[128] Cai; Bishuang. Mertk signaling in macrophages promotes the synthesis of inflammation resolution mediators by suppressing camkii activity. Sep 25;11(549):eaar3721.:10.1126/scisignal.aar3721., 2018.

[129] Van Acker; Heleen. Cd56 in the immune system: more than a marker for cytotoxicity? 8:10.3389/fimmu.2017.00892, 2017.

[130] Wu; Yongjian. Slamf7 regulates the inflammatory response in macrophages during polymicrobial sepsis. Volume 133, Issue 6 e150224:https://doi.org/10.1172/JCI150224, 2023.

[131] Sosa; Eleonora Sosa. Bdca1+ cdc2s, bdca2+ pdcs and bdca3+ cdc1s reveal distinct pathophysiologic features and impact on clinical outcomes in melanoma patients. Nov 24;9(11:e1190, 2020.

[132] Smith; Mitchell. Rituximab (monoclonal anti-cd20 antibody): mechanisms of action and resistance. Oct 20;22(47):7359–68, 2003.

[133] Grimsholm; Ola. Cd27 on human memory b cells–more than just a surface marker. Volume 213, Issue 2, August:164–172, 2023.

[134] Kovács; Kristóf. Revisiting the coreceptor function of complement receptor type 2 (cr2, cd21); coengagement with the b-cell receptor inhibits the activation, proliferation, and antibody production of human b cells. Apr 1;12:620427, 2021.

[135] Freudenhammer: Mirjam. Naive and memory-like cd21low b cell subsets share core phenotypic and signaling characteristics in systemic autoimmune disorders. Oct 15;205(8):2016–2025, 2020.

[136] Rubtsova; Kira. Age-associated b cells: a t-bet-dependent effector with roles in protective and pathogenic immunity. Sep 1;195(5):1933–7, 2015.

[137] Muhlich; Jeremy. Stitching and registering highly multiplexed whole-slide images of tissues and tumors using ashlar. 38:19:4613–4621, 2022.

[138] Desiree Desiree. Functional dissection of the granzyme family: cell death and inflammation. 235:73–92, 2010.

[139] Vahedi; Fatemeh. Human granzymes: related but far apart. 83:688–693, 2014.

[140] Chowdhury; Dipanjan. Death by a thousand cuts: granzyme pathways of programmed cell death. 26:389–420, 2008.

[141] Kiniry; Brenna. Differential expression of cd8+ t cell cytotoxic effector molecules in blood and gastrointestinal mucosa in hiv-1 infection. Mar 1;200(5):1876–1888, 2018.

[142] Tay; Savas. Single-cell nf-b dynamics reveal digital activation and analogue information processing. 466:267–271, 2010.

[143] Lee; Timothy. A noisy paracrine signal determines the cellular nf-kappab response to lipopolysaccharide. 2:ra65, 2009.

[144] Van Valen; David. Deep learning automates the quantitative analysis of individual cells in live-cell imaging experiments. 12:e1005177, 2016.

[145] Niaz; Asim. Self-initialized active contours for microscopic cell image segmentation. 12:1–13, 2022.

[146] Win; Khin. Comparative study on automated cell nuclei segmentation methods for cytology pleural effusion images. 2018:9240389, 2018.

[147] Mohammdian-Khoshnoud; Maryam. Optimization of fuzzy c-means (fcm) clustering in cytology image segmentation using the gray wolf algorithm. 22:9, 2022.

[148] Hornik; Kurt. Multilayer feedforward networks are universal approximators. Volume 2, Issue 5:359–366, 1989.

[149] Stringer; Carsen. Cellpose: a generalist algorithm for cellular segmentation. 18:100–106, 2021.

[150] Nateghi; Ramin. A deep learning approach for mitosis detection: application in tumor proliferation prediction from whole slide images. 114:102048, 2021.

[151] Corredor; Germán. Computational pathology reveals unique spatial patterns of immune response in he images from covid-19 autopsies: preliminary findings. 8:017501, 2021.

[152] Ginley; Brandon. Computational segmentation and classification of diabetic glomerulosclerosis. 30:1953–1967, 2019.

[153] Hermsen; Meyke. Deep learning-based histopathologic assessment of kidney tissue. 30:1968–1979, 2019.

[154] Madeleine Durkee. Quantifying the effects of biopsy fixation and staining panel design on automatic instance segmentation of immune cells in human lupus nephritis. 26, 2021.

[155] Stevens; Michiel. Stardist image segmentation improves circulating tumor cell detection. 14, 2022.

[156] Greenwald; Noah. Whole-cell segmentation of tissue images with human-level performance using large-scale data annotation and deep learning. 40:555–565, 2021.

[157] Bannon; Dylan. Deepcell kiosk: scaling deep learning–enabled cellular image analysis with kubernetes. 18:43–45, 2021.

[158] Schmidt; Uwe. Cell detection with star-convex polygons. pages 265–273, 2018.

[159] Weigert; Martin. Star-convex polyhedra for 3d object detection and segmentation in microscopy. March 2020.

[160] Otsu; Nobuyuki. A threshold selection method from gray-level histograms. 9 (1):62–66, 1979.

[161] Mosqueira-Rey; Eduardo. Human-in-the-loop machine learning: a state of the art. 56:3005–3054, 2023.

[162] Johnson; Evan. Adjusting batch effects in microarray expression data using empirical bayes methods. Jan;8(1):118–27, 2007.

[163] McKinnon; Katherine. Flow cytometry: an overview. Feb 21;120:5.1.1–5.1.11., 2018.

[164] Maecker; Holden. Standardizing immunophenotyping for the human immunology project. Jun;12(6):471, 2012.

[165] Wang; Ruiqing. Transcription factor network regulating cd(+)cd8(+) thymocyte survival. 31(6):447–58, 2011.

[166] Parel; Yann. Cd4+ cd8+ double positive (dp) t cells in health and disease. Mar;3(3):215–20, 2004.

[167] Mann; Henry. On a test of whether one of two random variables is stochastically larger than the other. vol. 18, no. 1:pp. 50–60, 1947.

[168] Spearman; Charles. The proof and measurement of association between two things. vol. 15, no. 1:72–101, 1904.

[169] Kilmer; Joseph. Ordinary least squares regression is indicated for studies of allometry. Jan;30(1):4–12, 2017.

[170] MacQueen; James. Some methods for classification and analysis of multivariate observations. Vol. 1. University of California Press.:281–297, 1967.

[171] Traag; Vincent. From louvain to leiden: guaranteeing well-connected communities. 5233, 2019.

[172] Halle; Stephan. In vivo killing capacity of cytotoxic t cells is limited and involves dynamic interactions and t cell cooperativity. 44:233–245, 2016.

[173] Delon; Jerome. Exclusion of cd43 from the immunological synapse is mediated by phosphorylation-regulated relocation of the cytoskeletal adaptor moesin. 15:691–701, 2001.

[174] Okada; Takaharu. Two-photon microscopy analysis of leukocyte trafficking and motility. 32:215–225, 2010.

[175] Rosenblatt; Frank. The perceptron: a probabilistic model for information storage and organization in the brain. 65 (6):386–408, 1958.

[176] Guangyu; Robert. Artificial neural networks for neuroscientists: a primer. Volume 107, Issue 6:1048–1070, 2020.

[177] Pan; Ziyan. Inhibition of mertk reduces organ fibrosis in mouse models of fibrotic disease. 16,eadj0133(2024), 2024.

[178] Rascio; Federica. Cytotoxic t lymphocytes (ctls) and kidney transplantation: an overview. 2325:203–213, 2021.

[179] Koyama; I. Depletion of cd8 memory t cells for induction of tolerance of a previously transplanted kidney allograft. 7 (5):1055–1061, 2007.

[180] Bueno V. et al. The role of cd8+ t cells during allograft rejection. 35(11):1247–1258, 2002.

[181] Mengel; Michael. Prognostic value of cytotoxic t-lymphocytes and cd40 in biopsies with early renal allograft rejection. 2004.

[182] Salcido-Ochoa; Francisco. Histopathological analysis of infiltrating t cell subsets in acute t cell-mediated rejection in the kidney transplant. 7 (4):222–234, 2017.

[183] Sato; Eiichi. Intraepithelial cd8+ tumor-infiltrating lymphocytes and a high cd8+/regulatory t cell ratio are associated with favorable prognosis in ovarian cancer. 102 (51):18538–18543, 2005.

[184] Grimbert; Philippe. The regulatory/cytotoxic graft-infiltrating t cells differentiate renal allograft borderline change from acute rejection. 83 (3):341–346, 2007.

[185] Süsal; Caner. A collaborative transplant study report: donor-specific antibodies require preactivated immune system to harm renal transplant. 9:366–371, 2016.

[186] Yokosuka; Tadashi. The immunological synapse, tcr microclusters, and t cell activation. 340:81–107, 2010.

[187] He; Kaiming. Mask r-cnn. page 2980–2988, 2017.

[188] Obrișcă; Bogdan. Histological predictors of renal outcome in lupus nephritis: the importance of tubulointerstitial lesions and scoring of glomerular lesions. 27:1455–1463, 2018.

[189] Hoyt; Clifford. Multiplex immunofluorescence and multispectral imaging: forming the basis of a clinical test platform for immuno-oncology. 8:674747, 2021.

[190] Tan; Wei. Overview of multiplex immunohistochemistry/immunofluorescence techniques in the era of cancer immunotherapy. 40:135–153, 2020.

[191] Berg; Mark. *Delaunay triangulations. in Computational geometry: algorithms and applications*. Springer Berlin Heidelberg, 2000.

[192] Pettie; Seth. *Minimum spanning trees. in Encyclopedia of Algorithms*. Springer US, 2008.

[193] Kang; James. *Voronoi diagram. in Encyclopedia of GIS*. Springer US, 2008.

[194] Palla; Giovanni. Squidpy: a scalable framework for spatial omics analysis. 19:171–178, 2022.

[195] Schapiro; Denis. Mcmicro: a scalable, modular image-processing pipeline for multiplexed tissue imaging. 19:311–315, 2021.

[196] Baumbartner; Christina. Lp peptide-mhc class ii complex stability governs cd4 t cell clonal selection. 184:573–581, 2010.

[197] Polliack; Aaron. Identification of human b and t lymphocytes by scanning electron microscopy. 138:607–624, 1973.

[198] Kupfer; Alexander. Reorientation of the microtubule-organizing center and the golgi apparatus in cloned cytotoxic lymphocytes triggered by binding to lysable target cells. 133:2762–2766, 1984.

[199] Dustin; Michael. The cellular context of t cell signaling. 30:482–492, 2009.

[200] Stoll; Sabine. Dynamic imaging of t cell-dendritic cell interactions in lymph nodes. 296:1873–1876, 2002.

[201] Freiberg; Benjamin. Staging and resetting t cell activation in smacs. 3:911–917, 2002.

[202] Wang; Xue. Function and dysfunction of plasma cells in intestine. Mar 13:9–26, 2019.

[203] Carrel; Alexis. La technique operatoire des anastomoses vasculaires et la transplantation des visceres. 98:859–864, 1902.

[204] Menon; Madhvi. A regulatory feedback between plasmacytoid dendritic cells and regulatory b cells is aberrant in systemic lupus erythematosus. Mar 15;44(3):683–697, 2016.